MOLECULAR SIMULATIONS OF RHEOLOGICAL, MECHANICAL AND

TRANSPORT PROPERTIES OF SOLID-FLUID SYSTEMS

by

YANGYANG SHEN

A Dissertation submitted to the

Graduate School-New Brunswick

Rutgers, The State University of New Jersey

in partial fulfillment of the requirements

for the degree of

Doctor of Philosophy

Graduate Program in Chemical and Biochemical Engineering

written under the direction of

Prof. M. Silvina Tomassone

and approved by

_____

_____

_____

_____

_____

New Brunswick, New Jersey

[January, 2010]

ABSTRACT OF THE DISSERTATION

Molecular Simulations of Rheological, Mechanical and Transport Properties of

Solid-Fluid Systems

By YANGYANG SHEN

Dissertation Director:

Prof. M. Silvina Tomassone

In this dissertation, two distinct but relevant systems are chosen as representatives of interesting solid-fluid systems. Molecular dynamics (MD) and Monte Carlo techniques are applied to investigate the rheological, mechanical and transport properties of these systems.

Firstly, polyethylene melt embedded with silica nanoparticles is examined to be of our interest. Since it is computationally impractical to model a complex system with a molecular description, a multiscale modeling approach, which combines both atomistic and mesoscale simulations, is employed to efficiently represent and study the polymer nanoparticle systems. Based on a coarse-grained force field for polyethylene, a novel method is developed for determining the solid-fluid interaction at the spherical interface. Our coarse grained model is designed to mimic 4 nm silica nanoparticles in polyethylene melt at 423K. A series of MD simulations are performed to investigate the factors that control the homogeneity of nanofillers inside polymer matrix, also in the presence of

nonionic surfactants (short chain alcohols). The effects of nanoparticle filling fraction, polymer chain length, and relative sizes between nanoparticles and polymer chains on the particle dispersion are explored. In addition, a fundamental relationship is pursued between the microstructure and macroscopic properties (transport and rheological) of polymer nanoparticle composites.

In this work another method for determining the solid-fluid interaction parameter is presented: the experimental adsorption isotherms are used to validate the potential parameters. The rapid expansion of silica nanoparticle agglomerates in supercritical carbon dioxide (RESS process) is chosen to be the system of interest. The simulations show that the effective attraction between two identical nanoparticles is most prominent for densely hydroxylated particle surfaces that interact strongly with CO_2 via hydrogen bonds, while it is significantly weaker for dehydroxylated particles. We also explore the shearing forces necessary to break an agglomerate in supercritical fluid. The agglomerate experiences deformation followed by elongation, and finally break-up. The calculated diffusion coefficient of CO_2 is expected to be smaller than the experimental value, because the nanoparticle agglomerate hinders fluid movement. In the direction of shearing forces, the diffusion of CO_2 shows a steep increase after the breakup, confirming the rupture of the agglomerate.

Acknowledgement

First and foremost, I thank my research advisor Prof. M. Silvina Tomassone for her guidance, encouragement and support throughout the course of this work. She introduced me to the challenging field of computational chemistry, and always provides theoretical insights and motivates me to pay careful attention to every details of my research. I also appreciate her taking the time to provide feedback on each of the articles, reports, and presentations I prepared, as well as this dissertation.

I owe much gratitude to my committee members, Profs. Yee Chiew, Fernado Muzzio, Jerry Scheinbeim and Sobin Kim, for their support at all levels that has greatly helped in improving my work. I would especially like to thank Dr. Aleksey Vishnyakov for many helpful discussions and crucial guidance in allowing me to realize my potential. Without his help, it would not have been possible to realistically model many of the most complex systems considered in this thesis.

I am very grateful to all the past and present members of Prof. Tomassone's research group. Their support and feedback have been extremely helpful in carrying out my research project. I am also thankful to the fellow graduate students in the department and a number of friends at Rutgers, who have shared all the excitement, frustration and rewards over the past years with me.

Dedication

I dedicate this dissertation to my parents with their endless love, encouragement and patience, who made all of this possible.

Table of Contents

List of Tables

Chapter 1

INTRODUCTION

This chapter is divided in two subsections. The first one explains the motivation for this thesis; the second subsection describes the specific research goals along with the organization of this thesis.

1.1   Motivation

Solid-fluid interaction problems are numerous in manufacturing processes, mechanical device performance, and biological systems. While at the nanometer scale, both the molecular structure of solid and fluid and the interactions between them at the atomistic length scales play a key role. They control a large number of phenomena, such as, wetting and drying of the solid wall, adhesion and stickiness between mechanical components, and capillarity effects in narrow slits. Due to the fundamental importance for many technological processes, interfacial properties at the solid-fluid interface have been studied extensively both experimentally and theoretically. Depending on the systems to be investigated, performing an experimental study of the interfacial properties can be sometimes difficult and challenging. In the last decade, computer simulations have complemented our understanding of the properties of pure homogeneous fluids and mixtures as well as their interfacial behavior with other fluids or solid surfaces. The interaction between solid and fluid phases is an essential determinant for computer simulations. In this thesis, two different solid-fluid interfaces were chosen to be studied: i) polymer-nanoparticle composites (Section 1.1.1) and ii) silica nanoaggregates in

supercritical CO_2 (Section 1.1.2). In what follows a background review is given for the two systems.

1.1.1 Polymer Nanoparticle Composites (PNC)

The first case of interest is polymer nanoparticle composites, where nanoparticles are considered as the solid phase and the polymer melt as the fluid phase.

Particles have long been added to polymers to improve their physical properties, such as strength, toughness and thermal behavior. Traditional polymer composites filled with micrometer-size fillers often show improvements in their mechanical properties in the form of an increase in modulus, yield strength, dielectric strength, and glass transition temperature [1, 2]. However, these gains are usually accompanied by losses in ductility and toughness, caused by the large ratio of filler to polymer typical of these materials or by the lack of homogeneity in dispersity inside the polymer matrix. Recently, nanoparticles have begun to replace larger particles in composite materials because they can impart different properties such as optical transparency, yet at the same time, they provide property enhancements at lower loadings [3, 4]. Furthermore, these nanostructured polymer composites display improved strength, fire-retardancy, and barrier properties over simple polymers or conventional copolymer composites [5].

For example, polymer nanocomposites exhibit even more enhanced mechanical properties at very low filler level (usually less than five percent by weight). Sumita et al. found dramatic improvements in the yield stress (30%) and Young modulus (170%) in nanofilled polypropylene compared to micrometer-filled polypropylene [6]. The mechanical analysis via stress-strain testing showed a substantial increase in the Young's

modulus, while values for strain at break and yield stress remain nearly at the same level of the pure matrix materials. These composites also showed no decrease in the strain-to-failure when filled with silica ranging from 7 to 40 nm in diameter.

In addition, polymer nanoparticle composites are used for the manufacturing of capacitors with high energy storage [7, 8]. A capacitor is an energy storage device. The amount of energy that a capacitor can hold depends on the insulating material between the metal surfaces, called a dielectric. A way of increasing the dielectric strength is to add ceramic nanoparticles, with high volume fraction for a significant improvement. Several systems have been used for the manufacturing of these types of capacitors, such as silica, titania, strontium titanate and barium titanate dispersed in perfluoropolyether, polydimethyl siloxane, and polyethylene [9]. They found that silica in polyethylene gives the highest dielectric strength when uniform dispersion of the nanoparticles was able to be achieved. This system is one of the most promising ones, however it is not completely understood. Having a good dispersion is of extreme importance to fully utilize the potential of dielectric materials. However it is not clear for what filling fraction it is possible to achieve a uniform dispersion of the nanoparticles inside the polymer matrix. This is, in fact, one of the motivations for our research. In chapters 3 and 5 we perform studies of the stability of silica nanoparticles in a polyethylene matrix and their corresponding rheological properties.

Generally speaking, in material science, the relationship between macroscopic properties and microscopic structures is crucial for scientists to improve known and design new materials. This is particularly important for the case of synthetic polymers, where material properties depend strongly on both the molecular structure and the

organization of macromolecules in the solid state: their phase structure, morphology, molecular order, molecular dynamics, etc. Different approaches have been developed to study these aspects respectively. Experimentally, the microstructure and order of materials are frequently studied using X-ray scattering, neutron scattering and various kinds of microscopy methods. Information about dynamics is mainly obtained from relaxation experiments. Computationally, molecular simulation techniques provide atomistic level and direct numerical experiments, and give insight on material behaviors under different physical conditions. They can potentially address the issues at solid–fluid interfaces and shed light on the interactions arising in the nanoscale-regime. In addition, large-scale simulations, which involve coarse-graining, significantly enhance the prospect of probing important mechanisms at molecular-level, which are the basis of macroscopic phenomena and interfacial behavior.

Even though significant progress has been made in developing polymer nanocomposites with varying polymer matrices and inorganic nanoparticles, the fundamental mechanisms that control the behavior of polymeric materials at the polymer/nanoparticle interface and their impact on macroscopic mechanical and constitutive properties are largely unexplored. This thesis is focused on the understanding of rheological, mechanical and transport properties of PNC at the molecular level using molecular simulations. Manipulating the filler microstructure can be a powerful design tool for controlling and optimizing macroscopic properties. If this proves to be correct, it will open new avenues for the systematic optimization of the properties that make composites more valuable for a myriad of applications. However, for this to be possible, essential questions that as of now still remain unanswered need to be addressed: How can

we characterize the effects of molecular interactions on the micro-structure of the filler phase? Can we develop effective methods for exploring the parametric space and optimizing the macroscopic properties? Can macroscopic materials properties be predicted from nanostructural data and molecular simulations? Other questions are also to be addressed: How does shear flow affect the spatial distribution of nanoparticles? How is the rheology of the polymers affected by the inclusion of nanoparticles? In this work we will answer these open questions.

1.1.2   Silica Nanoparticles in Supercritical Fluids

In this thesis, another solid-fluid system has been considered: silica nanoparticle agglomerates in supercritical carbon dioxide.

Currently, most popular methods of nanoparticle deagglomeration essentially rely on shearing of nanoparticle suspensions in organic solvents [10], often facilitated by surfactants/dispersants [11]. Another promising deagglomeration technique is the rapid expansion of supercritical solutions (RESS). In the first stage of the RESS procedure, an agglomerate of primary particles is saturated with supercritical fluid. The gas penetrates inside the pores of the agglomerates and after rapid depressurization the agglomerate is broken down by the extreme pressure gradients and fluid velocities. RESS is an environmentally benign technique that allows reducing the use of volatile organic solvents and is well established for the synthesis of micron- and sub-micron size particles [12].

However, the interaction forces between nanoparticles in the RESS technique are not completely understood, especially when the particles are at the nanoscale. Most of the

published work has been focused on the solvation forces between nanoparticles in vapors and liquids, but not in supercritical fluids. In vapors, the adsorption field of the two bodies typically leads to the formation of a liquid-like junction between them [13, 14]. Solvation forces can be interpreted in terms of the surface tension of the formed meniscus, and essentially the forces vanish when the liquid junction breaks up. The other group of simulation studies deals with solvation forces between planar surfaces and particles in liquids and polymers. Neither of these groups deals with dense supercritical fluids, where meniscus formation is not really possible (unlike vapors), but strong density variations are (unlike liquids).

To the best of our knowledge, there have been no reported simulation studies of breakup forces for nanoscale silica agglomerates in the presence of supercritical CO_2. The ultimate goal of this work is to shed light on the interaction forces between silica nanoparticles in supercritical CO_2, which determine the dominant mechanisms for deagglomeration when the fluid expands rapidly. We considered different types of aggregates (with different topologies and strengths) and studied how the agglomerate structure affects their final strength when exposing them to shear forces.

1.2   Objectives and Organization

Given the above mentioned open questions about any solid-fluid system, the aim of this thesis is to take us to the root of these issues: the solid-fluid interfacial structures and the basic interactions between structural units that determine the kinetics of nanoparticles in their embedding medium and assembly formation, and subsequently the

resulting structures and functionalities of the nanophases and devices. The specific aims are the following:

Specific Aim 1: To construct a coarse-grained model for polymer nanoparticle composites and validate the solid-fluid interaction by fitting surface tension experimental data. This work, along with the details of simulation techniques used, will be given in Chapter 2.

Specific Aim 2: To investigate how the microstructure of PNC (degree of agglomeration and morphology) is affected by changes in molecular weight, chain conformation, temperature and orientation of the polymers, and concentration of non-ionic surfactants. The results of this study are given in Chapter 3.

Specific Aim 3: To investigate the interaction forces between silica nanoparticles in supercritical carbon dioxide and the effect of agglomerate structure (with different topologies) on their final strength under shearing conditions. Another method for validating solid-fluid interaction is via the adsorption isotherms, and it was used here to determine silica and supercritical carbon dioxide. The results of this study are given in Chapter 4.

Specific Aim 4: To determine how microstructure of the filler nano-phase affects the macroscopic mechanical and constitutive properties of PNC. The results of this study are given in Chapter 5.

Finally Chapter 6 summarizes significant results and conclusions, and provides recommendations for future work. All references are listed at the end.

The results from this proposed work will allow construction of the relationships between microstructure and macroscopic properties in nanofilled polymer composites.

Such relationships can be used to optimize properties of existing materials, and to design new filler reinforced materials for novel applications. In addition, fulfillment of the stated objectives will expand knowledge of the science of nanoparticle-polymer interactions as well as provide technical information and design strategies for the new generation of polymer nanocomposites.

CHAPTER 2

COARSE GRAINED MODEL FOR POLYMER NANOPARTICLE

COMPOSITES

In this chapter, we focus on Specific Aim 1, where a multiscale simulation scheme is carried out for the system of silica nanoparticle aggregates in a polyethylene melt. We develop a coarse-grained model for polyethylene, for which the parameters of the solid-fluid interaction are determined from the results of a separate atomistic model. This procedure is divided into three steps: (i) thermodynamic derivation for the surface tension calculation, (ii) atomistic simulation for the surface energy calculation, and (iii) surface tension calculation using the coarse-grained model and subsequent comparison with the value obtained from the thermodynamic derivation performed in step (i).

In what follows, Section 2.1 gives the literature search on simulations of polymer models and introduces the one we used in this work. Section 2.2 explains the theoretical formalism for the derivation of the surface tension. Section 2.3 presents the results on the surface energy obtained with atomistic simulations. Finally, Section 2.4 shows the results of surface tension obtained with the coarse grained model and subsequent comparison with the thermodynamic model.

2.1   Introduction

Polymeric materials have a large range of physical properties [15, 16], which, together with the relative economy of their production, makes them extremely useful. These chain molecules are characterized by the repetition of chemically equal or similar

units (monomers). The simplest polymers are therefore chains of equally repeated units (homopolymers). One of the major challenges in polymer science is the large range of time and length scales spanning from interatomic bond distances (a few Å) to macroscopic scales. This challenge makes it even more demanding to understand polymers from a theoretical point of view. It is essential to combine different theoretical approaches developed independently in various fields of physics and theoretical chemistry, but they are not easily interlinked. Perturbation theories depend on the dominance of one interaction or length scale over all the others, only treated as perturbations. These theories are often not applicable to polymers due to the complex interrelation of length and time scales. This is difficult to incorporate into a theory as the resulting topology conservation imposes constraints on the equations of motion.

Computer simulations can contribute substantially to the understanding of polymer dynamics, where the different scales pose a severe problem. In fact, to deal with all the length and time scales is the hardest task in molecular simulations, because the time step of the simulations is set by the fastest motion, and in order to keep the correct dynamics, one has to carefully integrate out these fast degrees of freedom over all scales. The big advantage of simulations is the free access to all information about the system at all times. However, since simulations are only models of reality, they need to be validated against experiments or analytic theory, and the model is refined if necessary.

Our case study is silica nanoparticles embedded in a polyethylene melt. Because of its attractive properties, polyethylene (PE) is the world's largest volume thermoplastic and finds wide use in packaging, consumer goods, pipes, cable insulation, etc. The melt state of polyethylene is very interesting from the point of view of its dynamics depending

on the degree of polymerization, i.e. the chain length. The properties change drastically from liquid-like to rubbery behavior as the chain length increases. Moreover, they are viscoelastic. They behave liquid-like if slow deformations are applied. In the high-frequency range they respond elastically to deformations like a solid. Besides, the melt state is crucial to polymer processing as most polymers in industrial applications are processed in their melt state, e.g. by injection molding. Thus, the technological relevance of a better understanding of polymer melts is rather obvious.

2.2   Polyethylene Molecular Models

Increasingly computer simulations have been used to calculate thermodynamic properties of polymeric liquids from a molecular basis. In these simulations a suitable choice of molecular potential needs to be made and some compromise must be made between atomic detail and computational efficiency. In what follows, one united atom model and four coarse-grained models are described. The united atom model (Section 2.2.1) was used for the calculation and adjustment of the temperature of the coarse grained PNC system. The last coarse-grained model (Section 2.2.2 vi) was used for the study of the stability and rheology properties of the PNC system.

2.2.1   Siepmann-Karaboni-Smit (SKS) United Atom Model

The methyl ($-CH_3$) and methylene ($-CH_2-$) groups are treated as spherical interaction sites with interaction centers located at the centers of the carbon atoms. The interaction between sites on different molecules and between sites separated by more than 3 bonds on the same molecule is described by Lennard-Jones (LJ) potential:

$$V_{LJ}\left(r_{ij}\right) = 4\varepsilon_{ij}\left[\left(\frac{\sigma}{r_{ij}}\right)^{12} - \left(\frac{\sigma}{r_{ij}}\right)^{6}\right].$$ The Lorentz-Berthelot mixing rules are used for the

unlike interactions. The bond-stretching interaction is modeled by a harmonic potential:

$$V_{s}\left(\theta\right) = \frac{1}{2}k_{s}\left(r - r_{eq}\right)^{2}.$$ The bond-bending interaction is also governed by a harmonic

potential: $V_{b}\left(\theta\right) = \frac{1}{2}k_{b}\left(\theta - \theta_{eq}\right)^{2}.$ The torsional interaction is described by the model

developed by Jorgensen: $V_{t}\left(\phi\right) = \sum_{i=0}^{3} a_{i}\left(\cos\phi\right)^{i}.$

Utilizing this united atom potential model and the reversible reference system

propagator algorithm multi time step dynamics, Moore et al. have performed both

equilibrium and non-equilibrium molecular dynamics simulations of a mono-disperse

$C_{100}H_{202}$ polyethylene melt at 448 K and 0.75 g/cm^3 [17]. At equilibrium, rotational

relaxation time and self-diffusion coefficient are calculated. Under steady state shearing,

shear-enhanced diffusion and rheological properties are measured.

Using the same model and non-equilibrium molecular dynamics simulations of

planar elongational flow, Baig et al. have investigated various structural and rheological

properties of three polyethylene liquids, $C_{50}H_{102}$, $C_{78}H_{158}$, and $C_{128}H_{258}$ at different

densities but the same temperature (T = 450K) [18]. Many physical properties for these

rather long chains appeared to be qualitatively similar to those for shorter chains in the

previous work of this group [19]. The intermolecular LJ, intramolecular LJ, and bond-

stretching modes make positive contributions to the first and second elongational

viscosity, while the bond-torsional and bond-bending modes appear to make negative

contributions. Daoulas et al. have also considered a thin film of united atom polyethylene

melt confined between a semi-infinite graphite phase on the one side and vacuum on the other, and studied the interface between polymer melt and crystalline solid substrate [20]. The simulations are carried out in the *NPT* statistical ensemble with an efficient Monte Carlo algorithm based on variable connectivity moves. The local mass densities, the structural and conformational features of polyethylene at the two interfaces are analyzed.

2.2.2 Coarse-Grained Models

In general, the coarse-graining procedure consists of defining effective interactions governing the behavior of particles on a larger length scale than the all-atom or united atom model. There is not a simple definition of a coarse grained model, because the type of model strongly depends on the size of the system to be studied. In general, when defining a coarse grained model, one needs to make a compromise between the size of the system and the information and accuracy to be lost in the model, particularly when defining the "beads" or "particles". The coarse-grained interactions are generally adjusted by matching static properties of the material in consideration. Several coarse-grained models have been utilized to investigate different properties of polyethylene. (Note: the reader may jump directly to section (iv) without loss of continuity.)

i) Depa and Maranas use the distribution functions from the united atom simulation to parameterize the coarse-grained force field [21, 22]. Each coarse-grained bead represents four united atoms. Coarse-grained stretching and bending potentials are calculated by Boltzmann inverting the distributions obtained from the united atom simulation. They set the desired distribution of coarse-grained bond lengths from the positions of united atoms separated by one coarse-grained bond, and the distribution of

coarse-grained bond angles from the positions of united atoms separated by two coarse-grained bonds. The distribution for united atoms separated by three coarse-grained bonds is featureless, therefore a coarse-grained torsional potential is not used. Because the coarse-grained bond-stretching distribution is double peaked and the coarse-grained bond angle distribution is asymmetric, at least two Gaussian functions are used to describe them. The molecular dynamics simulations are performed in the NVT ensemble at 423 K using a Berendsen thermostat and a time step of 5 fs, and the dynamic properties of unentangled polyethylene are studied. When scaled by a constant factor the results are in excellent agreement with their underlying atomistic counterparts [21]. In the later studies of Depa and Maranas, the diffusion coefficients are compared to experimental values and united atom simulations [22]. They also assign the entanglement length using various methods, and compare tube diameters extracted using a primitive path analysis to experimental values. These results show that the coarse-grained model accurately reproduces dynamic properties over a range of chain lengths, including systems that are entangled. Even though their model is validated and works well, it only works for systems of 10 nm and smaller. Out goal is to target larger systems of at least 50nm.

ii) Vettorel and Meyer derived a coarse-grained model of polyethylene in the melt state with the aim to study polymer crystallization [23]. The model requires relatively low level of coarse-graining, and only two CH_2 groups are mapped onto one bead. The coarse-grained beads are connected with harmonic springs, and optimized angular potential, and an optional torsional potential. The coarse-grained potentials are derived from detailed all-atom simulations, and an optimized form of the force field is then derived to achieve good accuracy in reproducing the static properties of the chains. The

electrostatic effects accounted for by an explicit potential in the all-atom model are neglected, because they are absorbed in the effective non-bonded interaction. Even though this model allows a qualitatively reproduction of the structural features of polyethylene at low temperature, it only considers 2 CH_2 groups in a single bead, which restricts the fluid size.

iii) Xu et al. have developed a coarse-grained Monte Carlo method to investigate thin films of short polyethylene chains during the crystallization [24]. This method does not allow for the calculation of dynamic properties such as diffusion coefficient and viscosity, therefore we were unable to implement it in our work. To summarize, these coarse-grained models can be broadly divided into two classes. The first class consists of generic models such as the 2nnd diamond lattice model that does not retain a connection to the underlying atomistic description (e.g. the model of Xu et al.). The second class of models maintains chemical identity by using information from atomistic level simulations to obtain the coarse-grained force field (e.g. the other 2 models above).

iv) We have implemented the model proposed by Guerrault et al. [25]. In the coarse-grained model each CG bead consists of eight methylene groups of a linear polyethylene chain. The bonded and non-bonded interactions between them have been developed from the potential of mean force for PE. They first obtained the microscopic structure of PE using MC NPT simulations. Then the intramolecular coarse-grained force fields were defined to reproduce the atomistic pair correlation functions, accurately representing the static properties and reproducing as closely as possible the structural and thermodynamic properties of the original atomistic model. We applied their potentials in

our work, but modified their functional form. Our considered bonded and non-bonded potentials are:

Non-bonded $w_\lambda^{nb}(r) = a_1 \exp(-b_1 r^2) + a_2 \exp(-b_2 r^2)$ (2.1)

Bonded $w_\lambda^{b}(r) = k_{eq}(r - r_{eq})^4$ (2.2)

Here r is the distance between two beads $r = |\vec{r}_i - \vec{r}_j|$. The potentials of mean force are shown in Figure 2.1. The parameters of the potentials are given in Table 2.1.
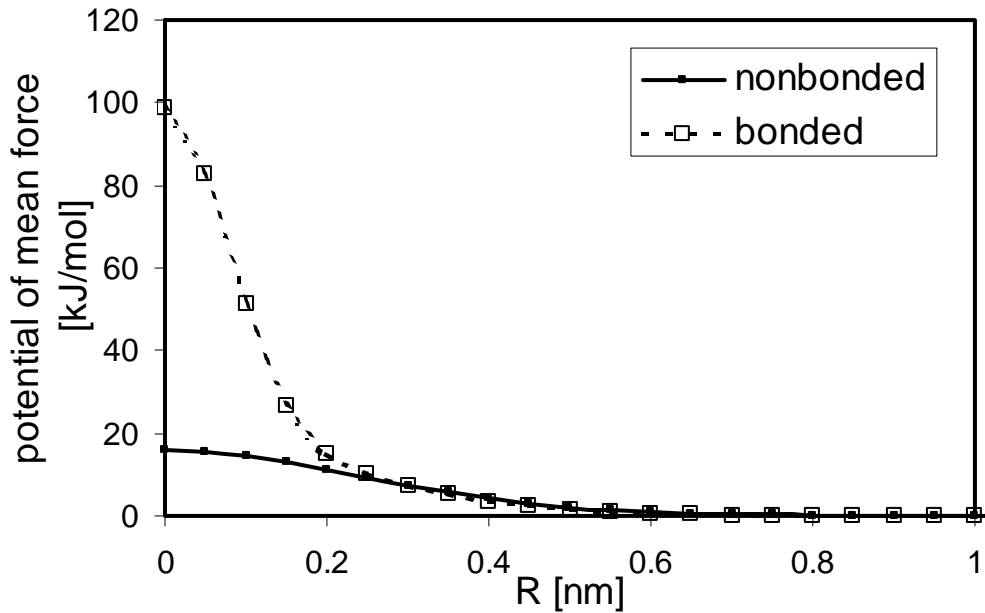
Figure 2.1 Bonded and non-bonded potentials of mean force. The bonded and non-bonded interactions for this system have been developed from the potential of mean force for PE by Guerrault et al. This GC model accurately reproduces the structural and thermodynamic properties of the original atomistic model.

2.3   Calculation of the Coarse Grained Temperature

When atoms are grouped into larger beads, their dynamics change, and as a consequence, their temperature (proportional to the kinetic energy via the Equipartition Theorem) also changes with respect to the temperature they would have if they were atoms (i.e. not grouped into beads as in a coarse grained model), so it needs to be adjusted.

The instantaneous temperature is proportional to the kinetic energy $k_B T = \dfrac{\sum\limits_{i=1}^{N} m_i v_i^2}{3N}$. To account for this change in temperature we considered a separate molecular dynamics simulation of polyethylene using the united atom model explained in Section 2.2.1.

The idea of this calculation is to obtain the temperature for a system using the united atom model, for which the interaction potentials are well validated in the literature, and then extrapolate the temperature that the system would have if it was modified to be a coarse grained model (i.e. grouping the united atoms into larger beads). In this system, polyethylene is modeled as a chain of 80 united atoms [17] (denoted by C80). The polymer system containing 100 chains is simulated at a temperature of T = 423K, which is coincident with the temperature used in experiments. After compressing the system to reach a density equal to 0.75 g/cm^3, the system is equilibrated for 200ps in an NPT ensemble. The system is first run for 100ps for equilibration and then, 200ps for data collection.

To derive the "coarse grained temperature" from the united atom model we have to remember that in the coarse grain model we combine 8 united -CH_2- groups into 1

coarse grain bead. Hence, the coarse grained temperature of the system is obtained by calculating the kinetic energy corresponding to the average velocity of 8 united atoms and then fitted to a Gaussian function (Figure 2.2). The mean value for V^2 is 5.0E-5 Å/fs, giving a coarse grained temperature T = 280.77K. Figure 2.2 shows the fitting of these curves. Here we can see that the coarse-grained temperature that correctly describes the experimental system (at 423K) is lower (280.77K) due to the fact that the atoms are grouped into beads and move slower.
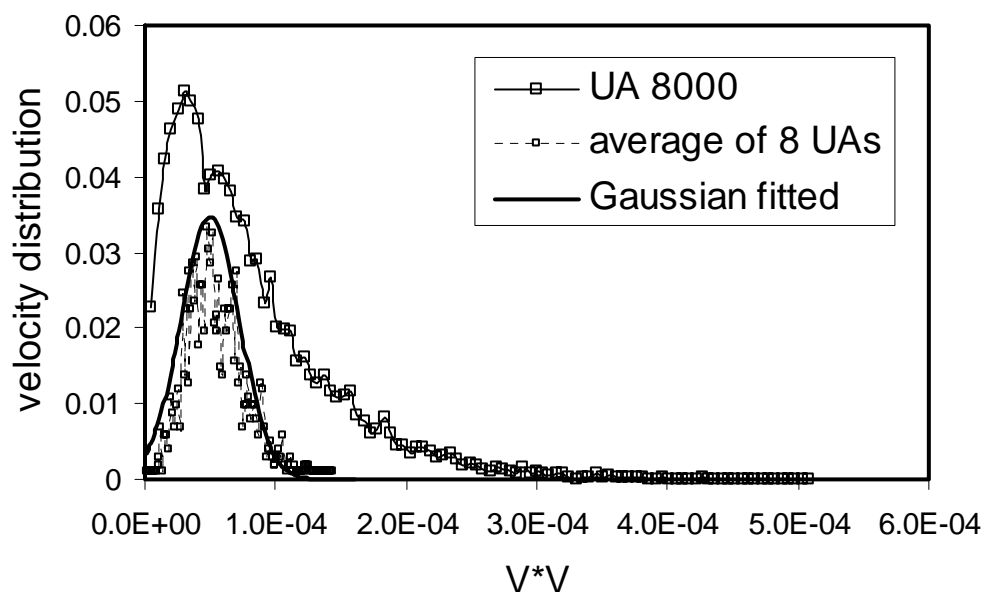
Figure 2.2 Velocity profile after equilibration. The distributions of the averaged velocities of 8 neighboring methylene groups were calculated. Then the temperature was obtained by fitting the velocity distribution with Maxwellian curve.

2.4   Determine the Solid-Fluid Interaction Parameters

When conducting molecular simulations, it is also necessary to have reliable descriptions of solid-fluid interactions for obtaining accurate thermodynamic and structural properties. Solid-fluid interactions between spherical silica nanoparticle and polyethylene for a coarse grained potential are not available in the literature.

Typically the interactions between different types are fitted either to the experimental thermodynamic properties (such as solubilities, activity coefficients, or surface tension) or to structural parameters (such as simulated RDFs). Since nanoparticle aggregation is to a large extent governed by the surface forces, fitting the unlike parameters to the surface tension is the most logical choice. The situation, however, differs dramatically from that in liquids, because aggregating nanoparticles never merge into a single solid body (unlike, for example, the aggregation of liquid droplets in an emulsion). That is why experimental values for PE-quartz interface reported in the literature do not suite our purpose either: they measure the free energy of a different process and indeed are extremely high for the scale we deal with in soft particle simulations. Instead, we came up with a thermodynamic scheme that allows us to derive the surface tension from the available experimental and simulated data.

As already mentioned in Section 2.2, the potentials describing these interactions are listed in Equation 2.1. The solid-fluid interaction is characterized by the surface tension. In what follows, we explain the theoretical formalism to obtain the repulsion coefficients a and b. For this, the idea is first to obtain the surface tension of the PE-Silica interfacial system and then perform coarse grained simulations to extrapolate the repulsion coefficients. We will first explain how to obtain the surface tension and then

how to extrapolate the value of the repulsion coefficients for the potential of Equation 2.1.

2.4.1   Surface Tension at Spherical Interface: A Thermodynamic Derivation

The surface or interfacial tension of a fluid interface can be viewed in two different ways. From a thermodynamic point of view it is the additional free energy per unit area caused by the presence of the interface. The energy per molecule is greater in the interfacial region than in the bulk liquid. From the mechanical point of view, the tension is a force per unit length parallel to the interface, i.e. perpendicular to the local density or concentration gradient. Regardless how interfacial tension is developed, thermodynamic (energy) or mechanical (force), its main effect is that a system acts to minimize its interfacial area.

The determination of the interfacial tension of planar interfaces between fluid phases is relatively straightforward within classical statistical mechanics. In the case of molecular simulations the mechanical route of Irving and Kirkwood, which requires the knowledge of the tangential and normal components of the pressure, is commonly employed. The situation is less obvious in the case of curved interfaces: according to the Laplace relation there is a pressure difference on either side of a curved interface which causes some level of difficulty on the evaluation of the tension via a mechanical route; in the case of small drops of liquid, one cannot strictly talk of a uniform value of the density (and local pressure) since the density profile can be oscillatory. In addition, an evaluation of the tension from the thermodynamic relation of Tolman (to first order in the curvature) is only formally valid for large drops. These complications lead to problems in the

determination of the interfacial tension of spherical drops in computer simulations. Here we have proposed a different method for calculating the surface tension of polyethylene on silica surface, based on fundamental thermodynamics concepts. The schematic is shown in Figure 2.3. Initially a slab of silica solid and a slab of polyethylene are placed next to each other. Then an interface is created following 3 stages: (i) we cut out one spherical space out of both slab, (ii) we move the spheres to the vacuum, and (iii) we replace them with the spheres of different species. As a result, two spherical interfaces have been created.
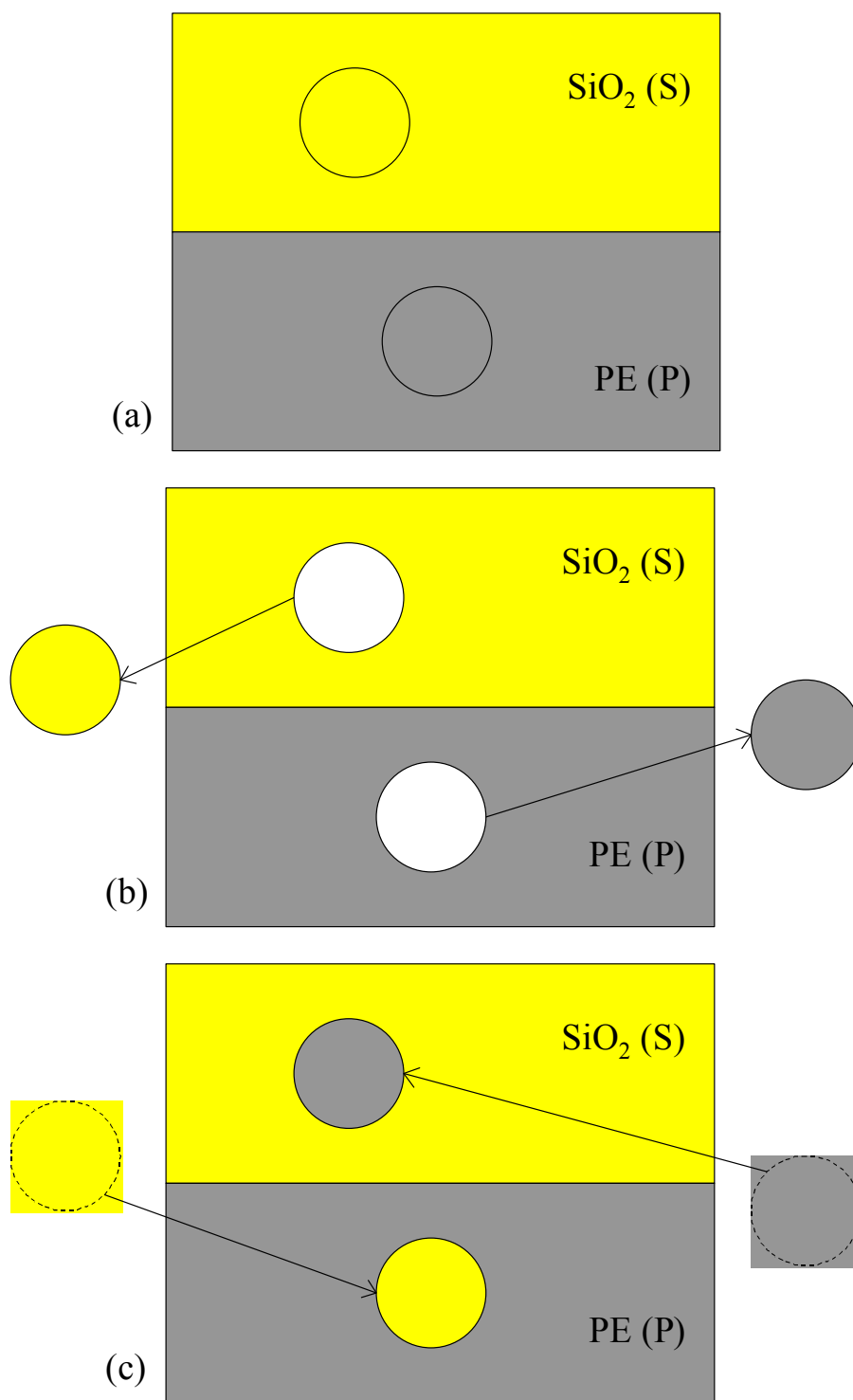
Figure 2.3 Scheme for creating a spherical solid-polymer interface.

For particulate matter, the surface tension can be presented as the difference of the free energy of adhesion and the free energy of cohesion divided by the surface area of the interface created. Assuming the canonical (NVT) conditions, the difference between the cohesion and adhesion free energies can be expressed as:

$$\gamma^*_{pe-silica} \Delta A = \Delta F = \Delta U_{pp-pv} + \Delta U_{ss-sv} + \Delta U_{pv-ps} + \Delta U_{sv-sp}$$

$$- T\left(\Delta S_{pp-pv} + \Delta S_{ss-sv} + \Delta S_{pv-ps} + \Delta S_{sv-sp}\right) \tag{2.3}$$

where ΔF is the total change in Helmholtz free energy, γ_{ps} is the surface tension between the "particulate" silica and PE, ΔU_{ss-sv} is the change of internal cohesion energy between the two silica surfaces (that is, the energy required for surface separation). ΔS_{ss-sv} is the entropy of the same process, ΔU_{pv-ps} is the energy of adhesion between PE and silica (that is, the energy required to bring together silica and polymer surfaces separated by vacuum) and so on.

We assume that the only entropy change is related to the limitation of polymer conformation due to the creation of the surface in polymer. The silica surfaces do not really deform; they stay intact and therefore their separation does not produce substantial entropy change. In this case, $\Delta S_{ss-sv} + \Delta S_{pv-ps} + \Delta S_{sv-sp} \ll \Delta S_{pp-pv}$. And Eq (2.3) reduced to

$$\Delta F \approx \Delta U_{pp-pv} - T\Delta S_{pp-pv} + \Delta U_{ss-sv} + \Delta U_{pv-ps} + \Delta U_{sv-sp} \tag{2.4}$$

Now, if we take into account that $\Delta U_{pp-pv} - T\Delta S_{pp-pv} = \gamma_p A$, where γ_p is the surface tension of the polymer (with vacuum). Finally we obtain the surface tension for the polymer-solid system γ^*_{ps}:

$$\gamma^*_{ps} = \gamma_p + (1/A)\left(\Delta U_{ss-sv} + \Delta U_{pv-ps} + \Delta U_{sv-ps}\right) = \gamma_p + (1/A)\left(\Delta U_{ss-sv} - 2 \times \Delta U_{ps}\right) \tag{2.5}$$

Therefore, $\gamma_{ps}^{*} = \gamma_p + \dfrac{1}{A}\left(\Delta U_{ss-sv} - 2 \times \Delta U_{ps}\right)$ (2.6)

Where ΔU_{ss-sv} is the energy related to the separation of two silica surfaces, and ΔU_{ps} is the energy of separation of polymer and silica. For γ_p we use the experimental value of polymer-vacuum surface tension, $\gamma_p = 0.027 \text{J/m}^2$. Notice that we do not have the values of ΔU_{ss-sv} and ΔU_{ps}. To obtain these two energies we perform separate atomistic simulations, which are explained in details in the following (Section 2.4.2).

2.4.2   <u>Atomistic Simulations for Calculating ΔU_{ss-sv} and ΔU_{ps}</u>

To obtain the internal energy terms, we performed classical MD simulations in Materials Studio package from Accelrys. In order to have two slabs of silica surfaces, we first need to get a cleavage of the silica glass and minimize the energy, then to place them in contact. Starting from an ideal quartz structure, the system is melt in a constant-pressure MD simulation at 1000K. Then the surface is quenched to the normal temperature of 423K and simulation continued for 1ns for silica to form an amorphous glass. After this, we minimize the resulting structure and cleave the surface of 21.4Å×21.4Å in the resulting sample. When cleaving the surface, some of the chemical bonds can be broken. The broken bonds are replaced with S-OH bonds; in total 8 hydroxyls were introduced resulting in a hydroxyl surface density of 15 mmol/m². The depth of the surface is set to be larger than the non-bond cut-off distances in the force field settings (13.16 Å).

Only the top few layers of atoms in the surface should interact with the polymer or another surface and the rest of the atoms can be considered to be part of the bulk and

therefore have little effect. By this means the bulk atoms are constrained at fixed positions so that they are not minimized. Then using the energy minimizer in Discover tools the surface is again relaxed in a 1ns MD simulation.

Afterwards, two initial configurations with different separations between the two slabs of solid are constructed. In one case (Figure 2.4 a), the solid surfaces are located at very close (or zero) distance. In the other case (Figure 2.4 b), they are separated by a large vacuum (20Å wide). Another vacuum layer is also added above the second surface so that only one side of the surfaces would interact with each other (otherwise due to the periodic boundary conditions both sides would be considered). Using Discover tools a molecular dynamics simulation of 300ps was conducted to equilibrate both the systems at T = 423K. Using Discover tools the system energy was calculated after equilibration. The total energies of the systems fluctuated around stable values after 100ps. The surface energy ΔU_{ss-sv} is obtained using the difference between two close solid surfaces and two separated solid surfaces. This is the energy required for creating a surface from the bulk, and will be implemented into the surface tension calculation.

(a)
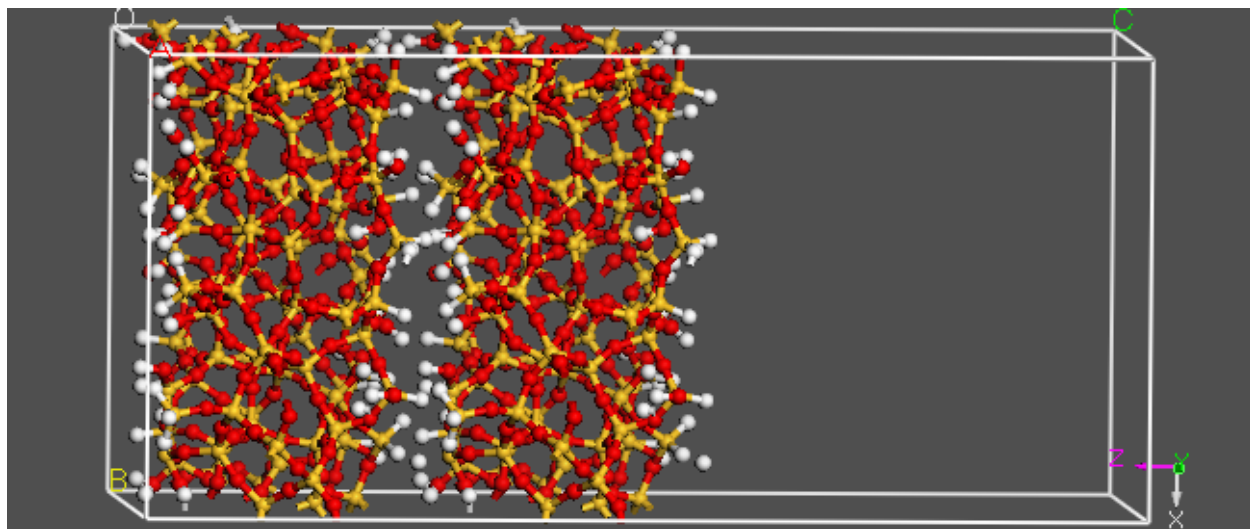
(b)
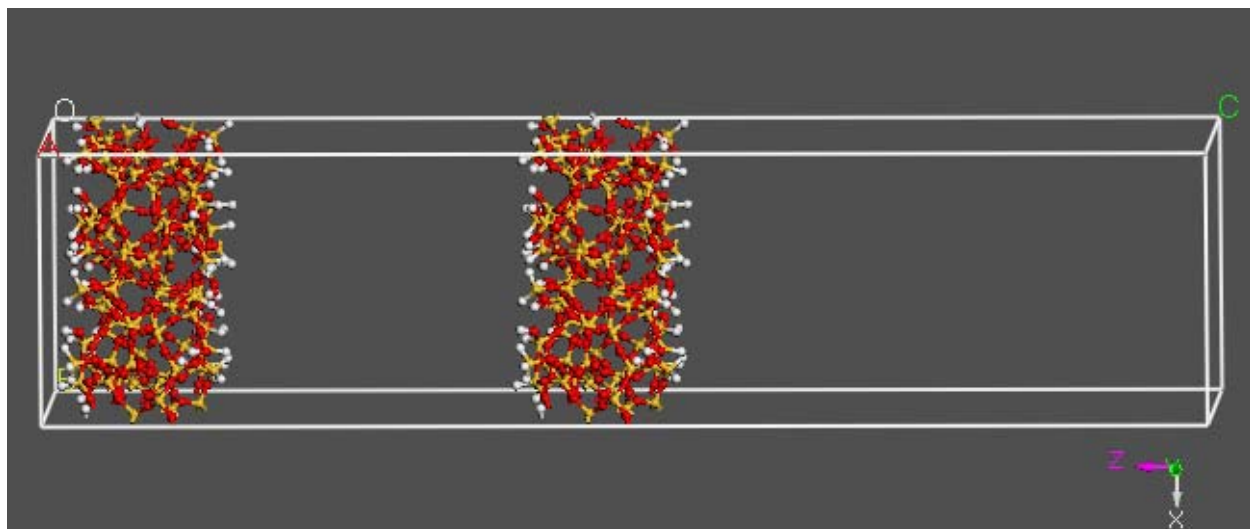
Figure 2.4 Simulation setup for calculation of the interfacial energy (ΔU_{ss-sv}) of two silica surfaces at close distance (a) and separated (b).

A similar procedure was followed for silica and polymer surfaces. We created a polymer slab by simulation of polyethylene in $21.4\text{Å} \times 21.4\text{Å} \times 10\text{Å}$ box at overall density of 0.75 g/cm^3. In two separate NVT MD simulations, we obtained the average energies of the silica slab and PE film. The silica and polymer surfaces were first separated, and then brought into contact and relaxed in a 1ns MD simulation (Figure 2.5). The surface energy ΔU_{ps} was obtained using the difference between two close surfaces of silica and polymer and two separated surfaces, and implemented into the surface tension calculation (Equation 2.6).

(a)
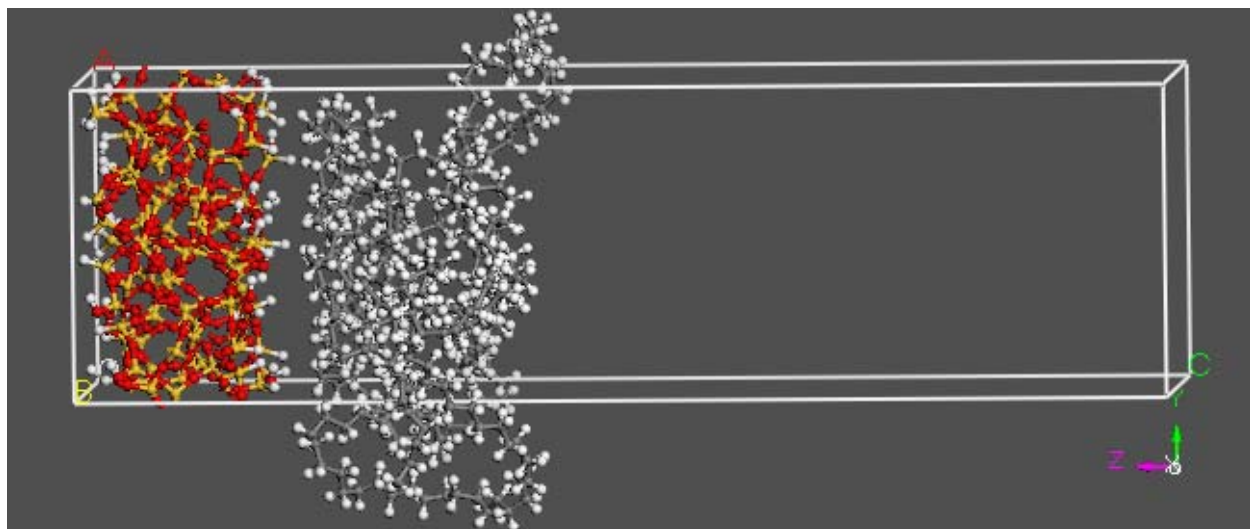
(b)
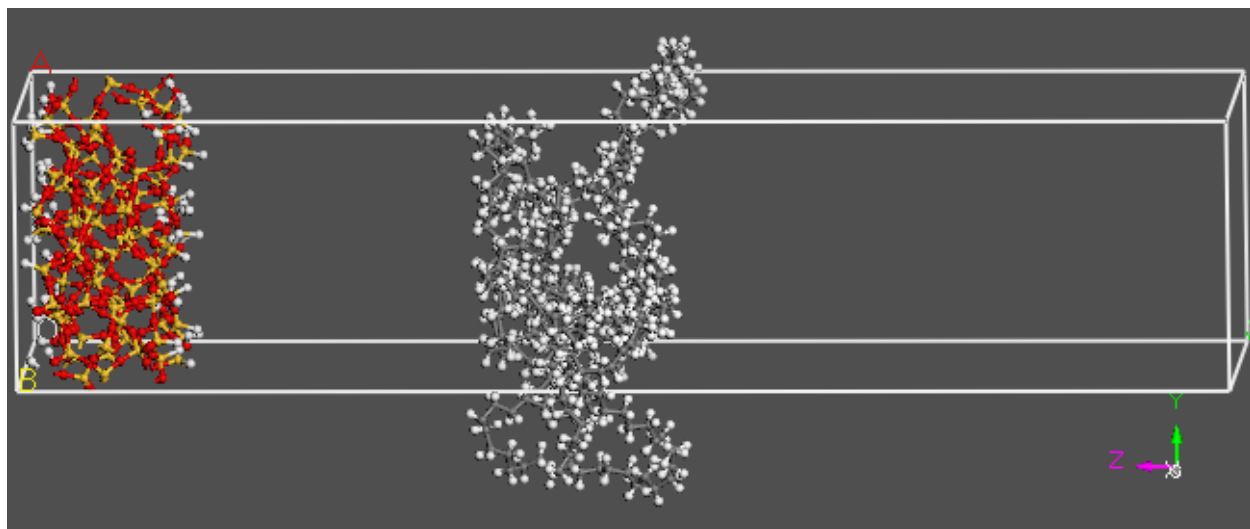
Figure 2.5 Simulation setup for calculation of the interfacial energy (ΔU_{ps}) of polyethylene chains on top of a silica surface (a) and PE-silica separated (b).

2.4.3 Surface Tension Simulations and Fitting the Repulsive Parameters

From the atomistic MD simulations, we obtained the surface energy values, ΔU_{ss-sv} and ΔU_{ps}, which were then substituted into Equation 2.6. In the same equation, we also considered the experimental value $\gamma_p = 0.027 \text{J/m}^2$, which results in the surface tension of 0.0156 J/m^2. So far we have obtained the value for the surface tension at a spherical interface. This, however, is not enough to complete the coarse grain potential (Equation 2.1), because we still do not have the repulsion parameters for the solid-fluid interaction.

To obtain the repulsion parameters, we considered a calibration curve, i.e. the dependence of the surface tension of our coarse-grained system as a function of repulsive mismatch coefficients a_1 and a_2. For this purpose, we simulated a slab consisting of our model coarse-grained silica in the coarse-grained PE in a box of the dimension $10\sigma \times 10\sigma \times 20\sigma$ (Figure 2.6), and performed a series separate simulations of a flat interface between the silica and polymer, using the coarse grained model. The surface tension was obtained from a mechanical formula:

$$\gamma_{\alpha\beta} = -\frac{1}{V} \left\langle \sum_i^{N_p} m_i u_{i\alpha} u_{i\beta} + \sum_i^{N_p} \sum_{j>i}^{N_p} r_{ij\alpha} F_{ij\beta} \right\rangle.$$
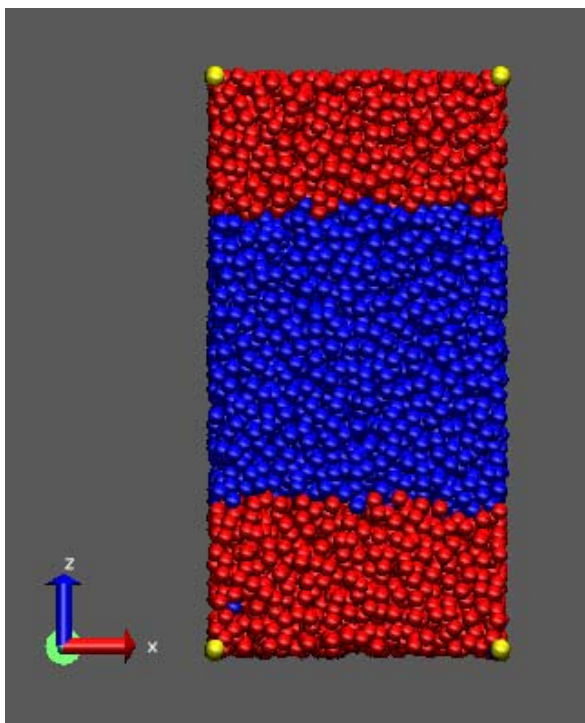
Figure 2.6 Phase separation between two different species. Red particles represent polymer beads, blue for nanoparticle beads.

The calibration plot (Figure 2.7) shows a linear relationship between surface tension and the repulsive coefficients. A repulsive coefficient of 2 means that the repulsion between a silica bead and a polymer bead is 2 times stronger then that for a couple of beads of the same component. Using the calculated surface tension, which is obtained from Equation 2.5 (giving the value 0.0156 J/m^2), on the calibration line, we extrapolated the repulsive coefficient, which is approximately equal to 2.3. This coefficient will later be used in the coarse-grained potential (Equation 2.1) as the solid-fluid interaction.
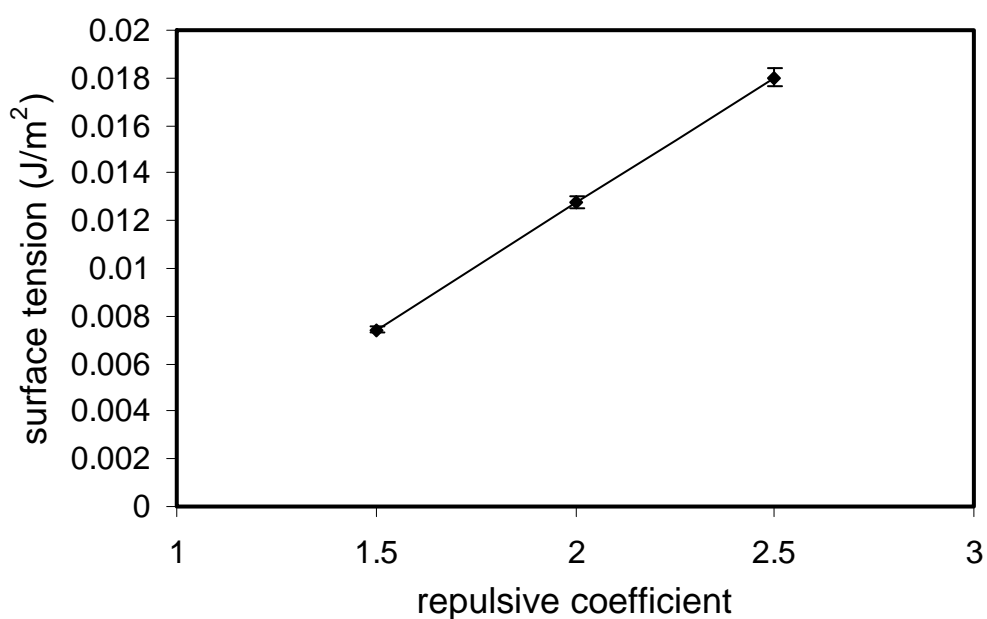
Figure 2.7 The calculated silica-polymer surface tension as a function of the relative strength of the repulsive potential.

2.5   Summary

In this chapter, we develop a coarse-grained model for silica nanoparticles in a polyethylene matrix at 423K, using a novel approach, which uses experimental data, thermodynamic theory and atomistic simulations. We employ a hybrid approach for coarse-graining, by fitting our model to structural and kinetic properties of the polyethylene melt and to the surface tension of polyethylene-silica interface.

Chapter 3

DISPERSION OF NANOPARTICLES IN A POLYMER MATRIX

In the previous chapter we have obtained the solid-fluid interaction parameters for our coarse-grained model, which can be used for studying the dispersion of silica nanoparticles in a polyethylene matrix. In this chapter, we focus on Specific Aim 2 and investigate the factors that determine the distribution of nanoparticles in a polymer melt, such as the molecular weight, chain conformation and orientation of the polymers, the interparticle forces, and the concentration of nonionic surfactants. The case study system consists of silica nanoparticles embedded in a polyethylene matrix, with oleyl alcohol as surfactant. The motivation for this choice is explained in Chapter 1 (Section 1.1.1).

In what follows, Section 3.1 introduces the model we used for silica nanoparticles. Section 3.2 explains two methods for quantifying the state of nanoparticle dispersion and the results. Section 3.3 presents the results on the effect of polymer chain length and the relative size of polymer to nanoparticle. Section 3.4 shows the results on the interparticle forces. Finally Section 3.5 first introduces the model surfactant, and then presents the results.

3.1   Nanoparticle Model and Simulation Setup

Model nanoparticles were constructed by soft quasiparticles, which are arranged in a body-centered-cubic (BCC) lattice (Figure 3.1). The quasiparticles were of the same size as the polymer beads. They were kept in a BCC structure using harmonic springs with 38 kJ/mol stiffness. The bond equilibrium length was chosen so that each

nanoparticle was composed of 108 beads and was approximately 4 nm in diameter in all our simulations. The bond lengths (0.63 nm and 0.445 nm) were chosen to maintain the same density of beads inside the nanoparticle as the density of beads in the polymer: 4.0 nm^{-3}. All atoms in the system interact via the derived coarse-grained potential (Equation 2.1). The interaction between nanoparticle beads is the same as that between the polymer beads, while the interaction between solid and fluid is 2.3 times more repulsive than the interaction between the same species. The repulsive strength parameters between different species in the coarse-grained model are listed in Table 3.1.
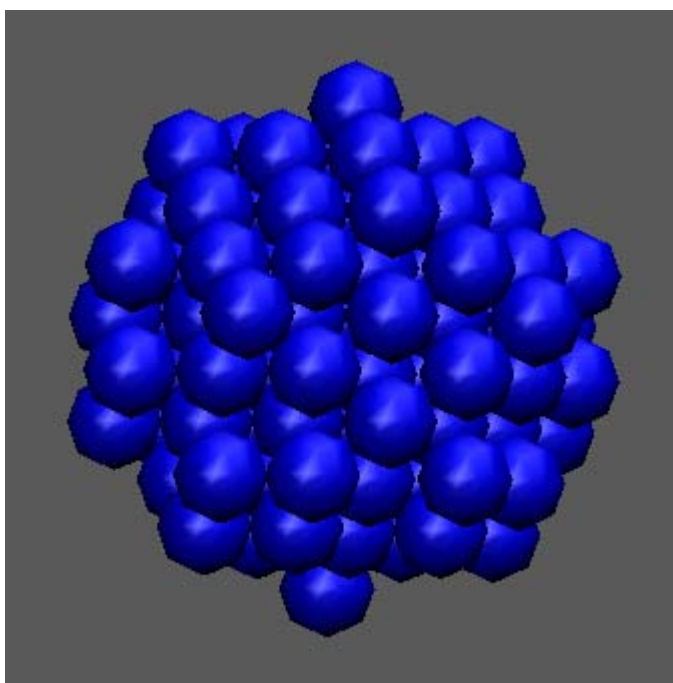
Figure 3.1 Schematic of the nanoparticle model.

In the initial configuration, all beads were given random positions in the simulation box of $30 \times 30 \times 30$ nm^3. The MD simulations were carried out in NVT ensemble with Verlet integration scheme [26] and timestep of 0.01 ps. The total simulation length ranged from 100 ns to 300 ns. Simulations of different numbers of nanoparticles in a polymer matrix were conducted systematically. They are based on standard molecular dynamics techniques in an NVT ensemble (constant number of particles, volume, and temperature).

3.2 Nanoparticle Dispersion

The state of nanoparticle dispersion is critical for the material reinforcement. Clustering of the nanoparticles reduces the intermixing of polymer and nanoparticles, thus reducing the interfacial area. The nanoparticle homogeneity is affected by a number of factors, including particle loading, interparticle interactions, and some polymer properties. Before we can explore the relative importance of these control parameters, we must have a reliable metrics to determine the state of dispersion. The spatial dispersion of nanofillers can be determined by means of the radial distribution function $g(r)$, which is an explicit measure of structure and in our case is taken from center to center of nanoparticles.

We have examined the polymer nanoparticle systems with a range of nanoparticle filling fractions. In these simulations, the polymer has a fixed chain length ($N = 8$). At lower filling fractions (1.6 wt% and 2.4 wt%) smaller clusters of 4 nanoparticles have been found. At higher filling fractions (greater than 3.2 wt%) larger clusters of 6 or 8 nanoparticles have formed. In all the cases considered, there exist a small number of

nanoparticles, which remain separated. In order to determine the state of nanoparticle dispersion we calculated $g(r)$ based on the distances between the centers of mass of the nanoparticles (Figure 3.2). There is a strong tendency for the nanoparticles to aggregate as illustrated by the sharp peak in the nanoparticle-nanoparticle radial distribution function. For a smaller filling fraction, the lower first peak in the radial distribution and the flat distribution at large distance indicate the dispersion of nanoparticles. As we increase the filling fraction, the nanoparticle density is less spatially homogeneous, yielding a second peak at large distance. The coexistence of the first and secondary peaks indicates larger degree of agglomeration.

The state of dispersion of nanoparticles can also be elucidated by the approach proposed by Starr et al. [27]. Potential energy (Figure 3.3a) and specific heat (Figure 3.3b) as a function of filling fraction are calculated. The potential energy per nanoparticle bead $u_{nn} = U_{nn}/N$ is strongly sensitive to the change in local packing, because it depends on the number of particle-particle contacts. The potential energy increases with increasing filling fraction, as relatively more contacts are made. The specific heat per particle of the nanoparticles is considered as the potential energy fluctuations $\delta u_{nn} \equiv u_{nn} - \langle u_{nn} \rangle$, and is thermodynamically quantified by $c_V^{nn} = \dfrac{N \langle \delta u_{nn}^2 \rangle}{T^2}$. At the largest and smallest filling fractions, the systems are very stable, thus there are little fluctuations in the potential energy. But for the intermediate states, particles easily aggregate into clusters, and can separate after a short period of time, resulting in large fluctuations in the potential energy, and hence a large value of c_V. As the filling fraction increases, the c_V reached a high peak at 2.7 wt% when there are possibilities for the nanoparticles to form

smaller clusters of 2~3 entities. Later as more nanoparticles are included in the system, the formation of larger clusters takes place, giving a lower peak on the c_V curve. The system is less stable when the smaller clusters are formed (higher peak on the curve), and becomes more stable when the larger clusters are formed (lower peak on the c_V curve).
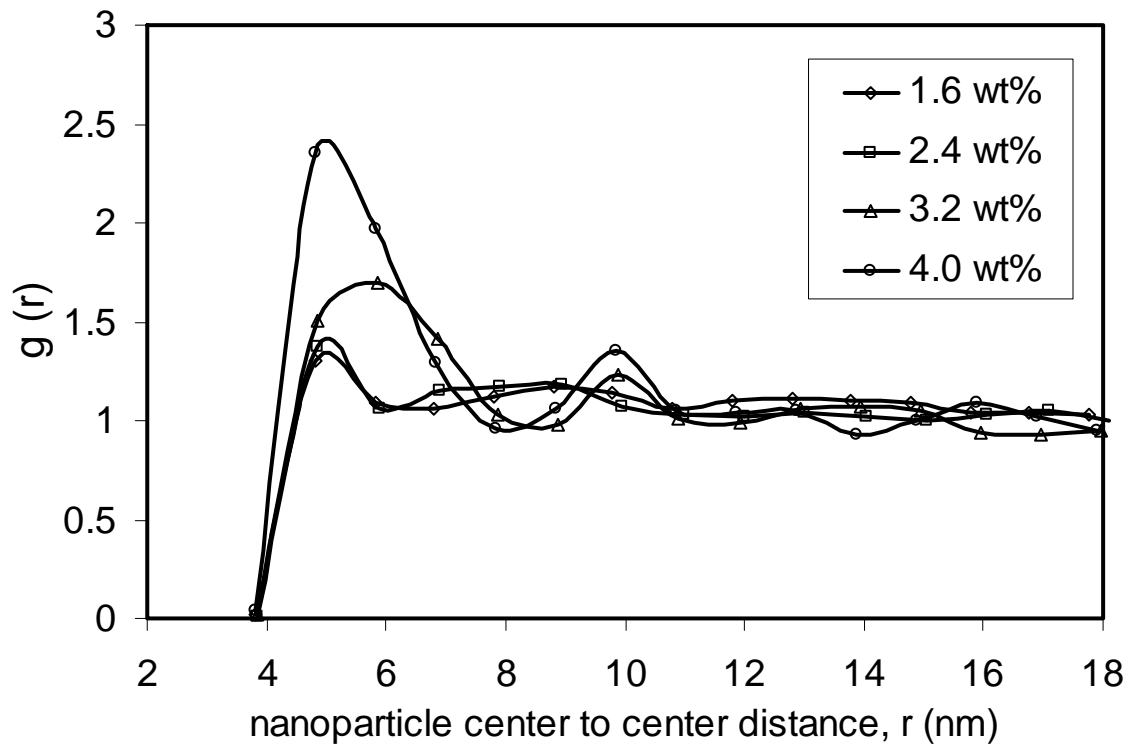
Figure 3.2 Radial distribution function of nanoparticle center of mass at different nanoparticle filling fractions.

3.3 Effect of Polymer Chain Length

The difference in the dispersion efficiency should mainly come from the polymer–nanoparticle interaction, which is a function of polymer chain length and polymer molecular structure. In this work we have also considered the effect of polymer chain length on the dispersion of nanoparticles. The polymer chain length is varied from $N = 4$ to 16. Figures 3.3 (a) and (b) respectively show the potential energy and specific heat as a function of nanoparticle filling fraction for three different polymer chain lengths. Longer chains tend to hinder the movement of nanoparticles and prevent them from agglomeration. This is also observed from the trajectories.
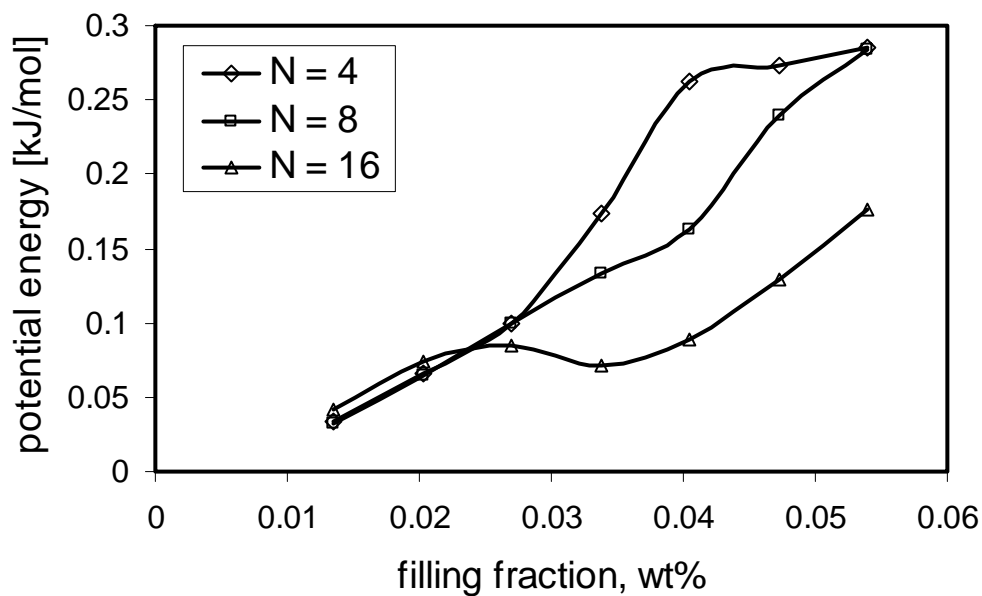
(a)
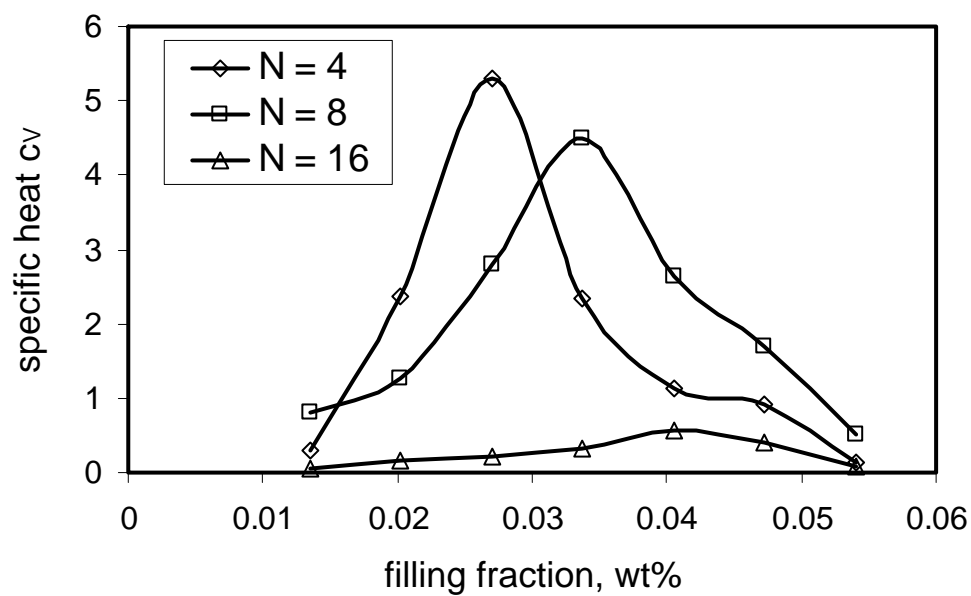
(b)

Figure 3.3 Potential energy (a) and specific heat (b) as a function of nanoparticle filling fraction for different polymer chain lengths.

In addition, the relative size of the nanoparticle and polymer is a crucial factor that causes phase separation and nanoparticle agglomeration [28, 29]. An important feature of molecular simulations is the accessibility of the molecular details of a system, which allows the direct calculation of microscopic properties, which in experiment would require sophisticated optical or scattering techniques. In this section we investigate the alignment and extension of molecules, as well as their rotation. The polymer radius of gyration is defined as the root mean square distance between monomers, i.e.

$$R_g^2 = \frac{1}{2N^2} \sum_{i,j} (r_i - r_j)^2 ,$$ which describes the dimension of a polymer chain. First, we simulated the pure system only containing polymer chains, and obtained the initial radius of gyration radius (R_{g0}) for different chain lengths. After adding nanoparticles in the system, chain stretching has been observed in some Monte Carlo simulations [30]. In our system the nanoparticle radius is about 2 nm, and the polymer R_g value ranges between 2.3 and 9.4 nm. Figure 3.4 shows the polymer radius of gyration (R_g) relative to that without nanoparticles (R_{g0}) for three different polymer chain lengths as a function of nanoparticle filling fraction. For nanoparticle size is similar to the polymer radius of gyration, the particles experience fast diffusion, and they move through the polymer melts without necessarily waiting for chains to relax their conformations, so that the chains keep to their initial dimension. However we observed chain expansion in all other cases of longer polymer chains. The nanoparticles stretch the polymer chains, and in turn they show more dispersion with larger R_g. This is due to more adsorbed amount of polymer on the nanoparticles when the chain is longer.
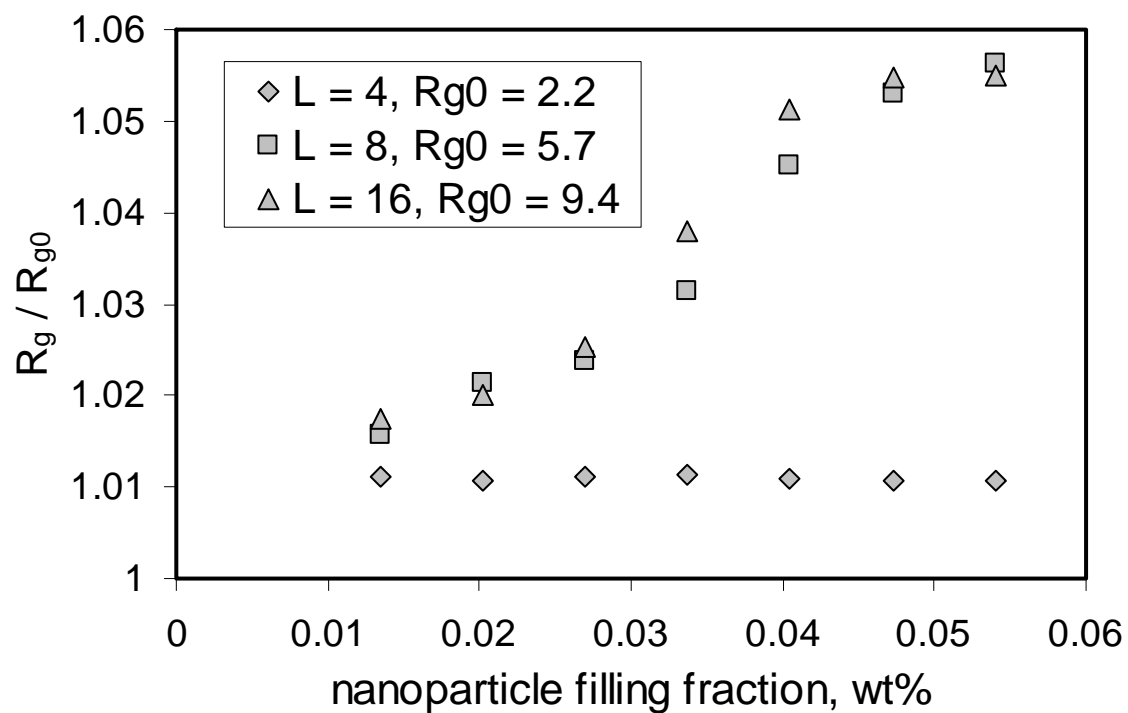
Figure 3.4 The polymer radius of gyration (R_g) relative to that without nanoparticles (R_{g0}) for three different polymer chain lengths as a function of nanoparticle filling fraction. Error bars represent standard deviation from three separate 5 ns simulations at each chain length.

3.4   Polymer Mediated Nanoparticle-Nanoparticle Forces

When particles are immersed in fluid and two surfaces approach closer than a few nanometers, they experience the fluid-mediated interactions, resulting from the confinement of fluid between surfaces. These interactions are generally called 'solvation forces', which is the key quantity governing the behavior of nanoparticle agglomerates.

In this work we have included two nanoparticles, whose positions were fixed in the simulation box, but the distance between them was varied. The solvation force was calculated as $F_s = \left\langle \sum_{i=1}^{N} \sum_{j=1}^{M} l_j f_{ij} \right\rangle$, where N is the number of fluid molecules, and M is the number of silica pseudoatoms in one nanoparticle. Here, f_{ij} is the force between fluid molecule i and pseudoatom j, l_j is a coefficient that equals 1 if the pseudoatom j belongs to the first nanoparticle and $l_j = -1$ if j belongs to the second nanoparticle. Each MD simulation lasted for 150ns. The solvation force was averaged over the last 100ns of simulation run. Figure 3.5 compares the solvation force as a function of nanoparticle center-to-center distance for two different polymer chain lengths. The oscillatory feature of the solvation force shows the dramatic consequences of oscillatory collective polymer density fluctuations on the solvation force. The attractive minimum occurs at approximately 5.6 nm, and then there is a repulsive maximum at about 7 nm for both chain lengths, after which the force seems to decrease slightly and approach to zero at larger separations. When two nanoparticles covered with chain molecules approach each other, the chains extend out and overlap with each other. At this point, the polymer chains are being compressed between the surfaces, leading to an unfavorable entropy change. Thus the nanoparticles experience a repulsive force. In the case of longer polymer chains

the forces shift up towards the repulsive region, and the repulsive maximum is higher, due to greater amount of polymer adsorption.
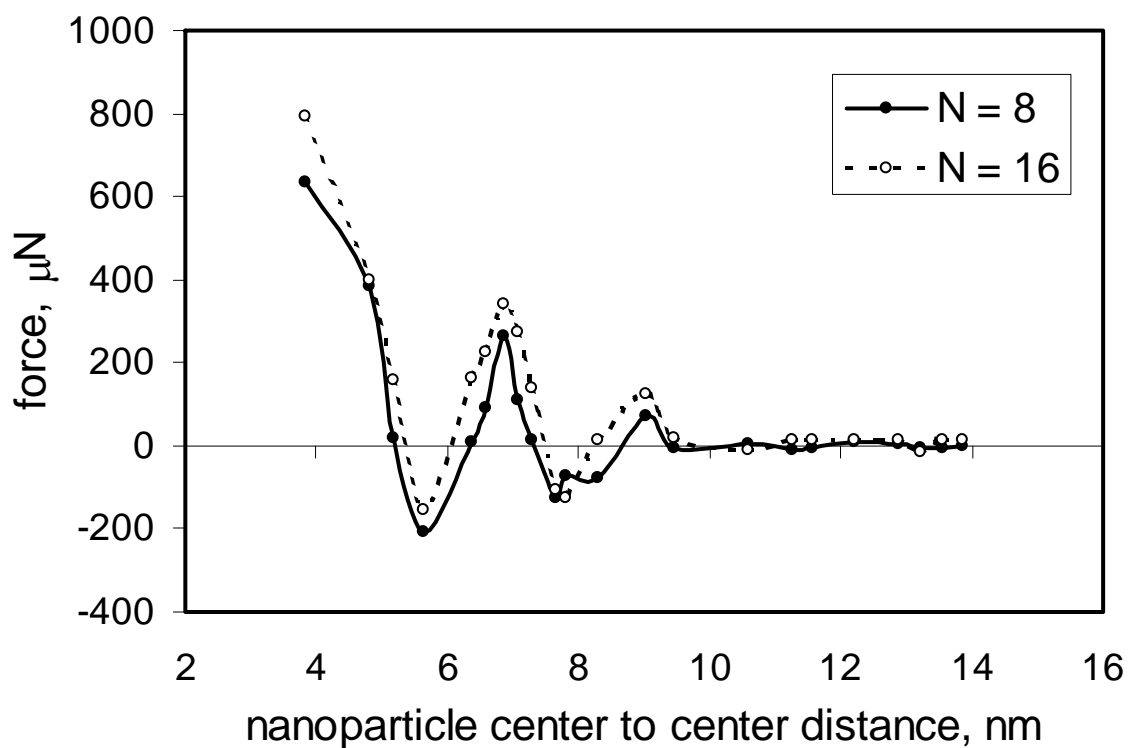
Figure 3.5 Solvation forces as a function of nanoparticle separation (two polymer chain lengths).

3.5   Effect of Nonionic Surfactants

We have also considered the effect of nonionic surfactants on the nanoparticle homogeneity. Typically, surfactant molecules consist of two chemically bounded components, one of which is soluble in the dispersion medium, while the other is generally insoluble. In an aqueous medium, the former is known as the hydrophilic group and the latter the hydrophobic group. The hydrophilic group, otherwise known as the "anchor" group, attaches itself to the colloidal particles. The hydrophobic group possesses a high affinity for the polymer, is projected away from the particle surface into the dispersion medium and is responsible for the stability of the suspension. The most common type of surfactant that is used to impart stability to a suspension comprises a polyoxyethylene oxide group -$(OCH_2CH_2)yOH$, which is hydrophilic, linked to an alkyl $CxH2x+1$ chain.

In what follows, Section 3.5.1 introduces the nonionic surfactant used in the system and its molecular model. Section 3.5.2 determines the critical micelle concentration of surfactant in polymer melt. And section 3.5.3 examines the adsorption of surfactants at the solid-liquid interface.

3.5.1   Surfactant Model Description

As mentioned earlier, we considered oleyl alcohol ($C_{18}H_{36}O$) as our dispersant. This molecule has the common components of the surfactants used in several industrial products such as shampoo, washing powder, etc. The chemical structure of the oleyl alcohol surfactant molecule is shown in Figure 3.6(a). This molecule has the common components of the surfactants used in several industrial products such as shampoo,

washing powder, etc. It consists of a weakly polar head, as the hydroxyl group, and a nonpolar hydrocarbon chain, and is modeled using coarse-grained beads. The schematic is shown in Figure 3.6(b). In the surfactant model, consecutive beads along each surfactant backbone are permanently bonded together via a harmonic spring. The CG beads in the surfactant tail should "like" the CG polymer beads, and the head bead "dislike" them. Lengths of the surfactants are expressed in total number of beads connected together in the molecule. Nonbonded interactions between different species are listed in Table 3.1. The hydrophobic interactions between the polymer and surfactant tails are strong, while the interaction between the polymer and surfactant headgroups on the micelle surface is weak.

Table 3.1 Repulsion parameters of different species.

	Polymer and surfactant hydrophobic bead (Type 1)	Nanoparticle bead (Type 2)	Surfactant hydrophilic bead (Type 3)
Type 1	1.0	2.3	2.5
Type 2		1.0	1.5
Type 3			1.0

We have previously characterized surfactant-laden systems with appropriate hydrophilic and hydrophobic particle-particle interactions. We will use those parametric values, which have already been validated with experiments [33]. Ultimately we seek to elucidate the dispersion properties of nanoparticles in a polymer matrix in the presence of non-ionic surfactant molecules.
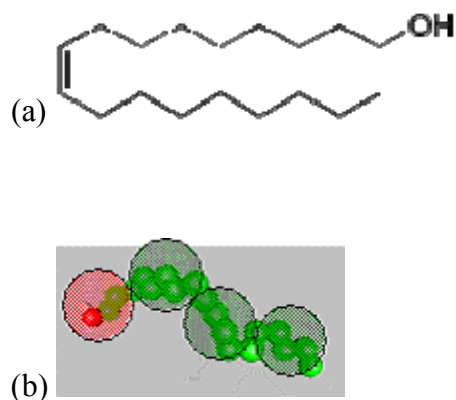
Figure 3.6 Chemical structure of oleyl alcohol (a) and schematic model of surfactant molecule (b).

3.5.2   Critical Micelle Concentration

In order to understand the aggregation of nonionic surfactants, it is crucial to know their physical properties (e.g. detergency, solubility, micelle formation and solubilization of substance) in the nonaqueous solutions. Micelle formation or micellization is an important parameter due to a number of important interfacial phenomena, such as detergency and solubilization. The concentration of surfactant at which micellization begins is called the critical micelle concentration (CMC). At concentrations below CMC, surfactants tend to adsorb as a monolayer at the water-air interface. At concentrations above CMC, they build spherical, rodlike, or disclike micelles. This parameter can be determined by many different techniques. The most popular techniques include surface tension, turbidity, self diffusion, conductivity, osmotic pressure and solubilization. All of these methods involve plotting a measure as a function of the logarithm of surfactant concentration. The breakpoint in the plot represents the CMC. The CMC is affected by several factors like as hydrophobic group, hydrophilic group, temperature, connection of the group in the structure and addition of salts and organic solvents [34, 35].

For an ideal system the surface tension (σ) reduces linearly with surfactant concentration (ϕ) until it plateaus at the critical value CMC for micelle formation; when the surfactant concentration is greater than CMC, the new surfactant does not enter the already saturated interface and instead enters into an association with other surfactant molecules in the bulk in a micellar arrangement in which hydrophilic heads come together trying to escape from the polymer.

In this work, the surface tension method was employed in the polymer + nonionic surfactant systems for determining the CMC. The bulk phase, containing the model surfactant and polymer, has been simulated through the NVT MD simulation. The concentration of surfactant is systematically varied, and the surface tension is measured by the mechanical formula: $\gamma_{\alpha\beta} = -\dfrac{1}{V}\left\langle \sum_{i}^{N_p} m_i u_{i\alpha} u_{i\beta} + \sum_{i}^{N_p}\sum_{j>i}^{N_p} r_{ij\alpha} F_{ij\beta} \right\rangle$. With increasing surfactant concentration, the surface tension first takes a constant value, and then it reduces linearly with surfactant concentration, until finally the curve levels off (Figure 3.7).
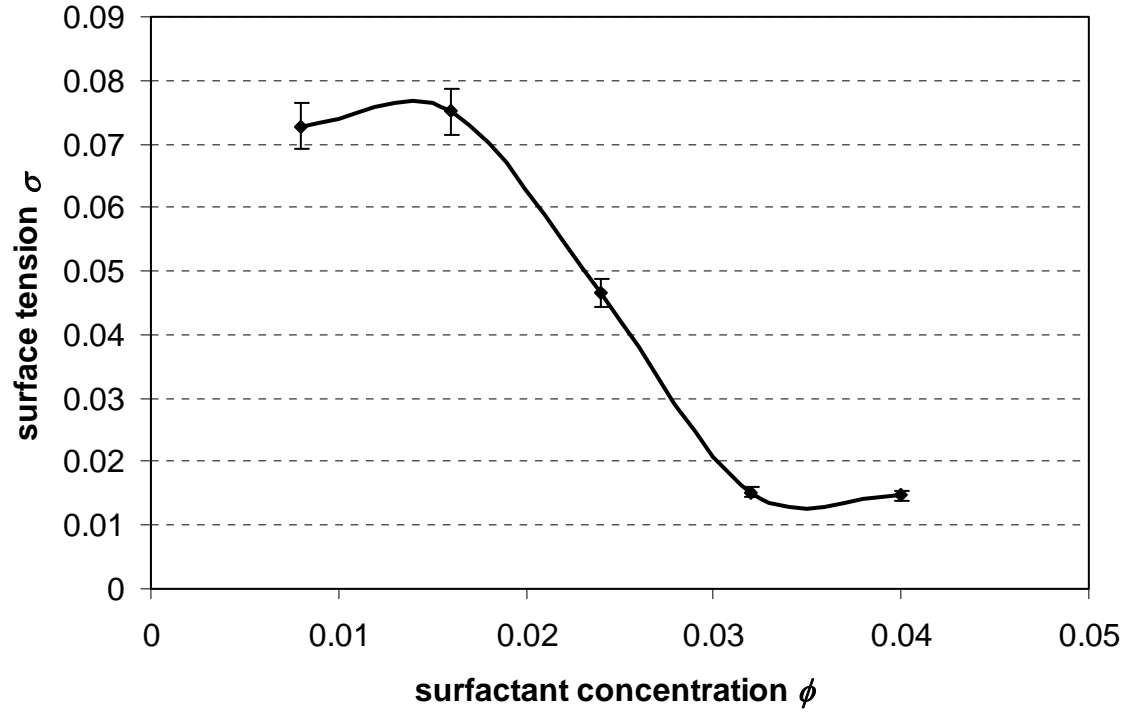
Figure 3.7 Surface tension σ versus bulk concentration φ of surfactant-polymer system. $\varphi\_$CMC is the critical micelle concentration, and $\sigma\_$CMC is the maximally reduced surface tension.

Our coarse-grain model successfully shows the formation of spherical aggregates of nonionic surfactant in polyethylene. A typical configuration snapshot of the bulk-phase simulation was shown in Figure 3.8, where the micelle structure is formed in the bulk phase. Visual inspection of the final snapshot at 20ns indicates that there is no obvious disparity in the final micelle structures, which may give evidence that the bulk phase micelle is stable. The polymer is adsorbed onto the micelle surface and in between the surfactant head groups, due to the strong hydrophobic interaction between the ethylene units and alkyl tails.
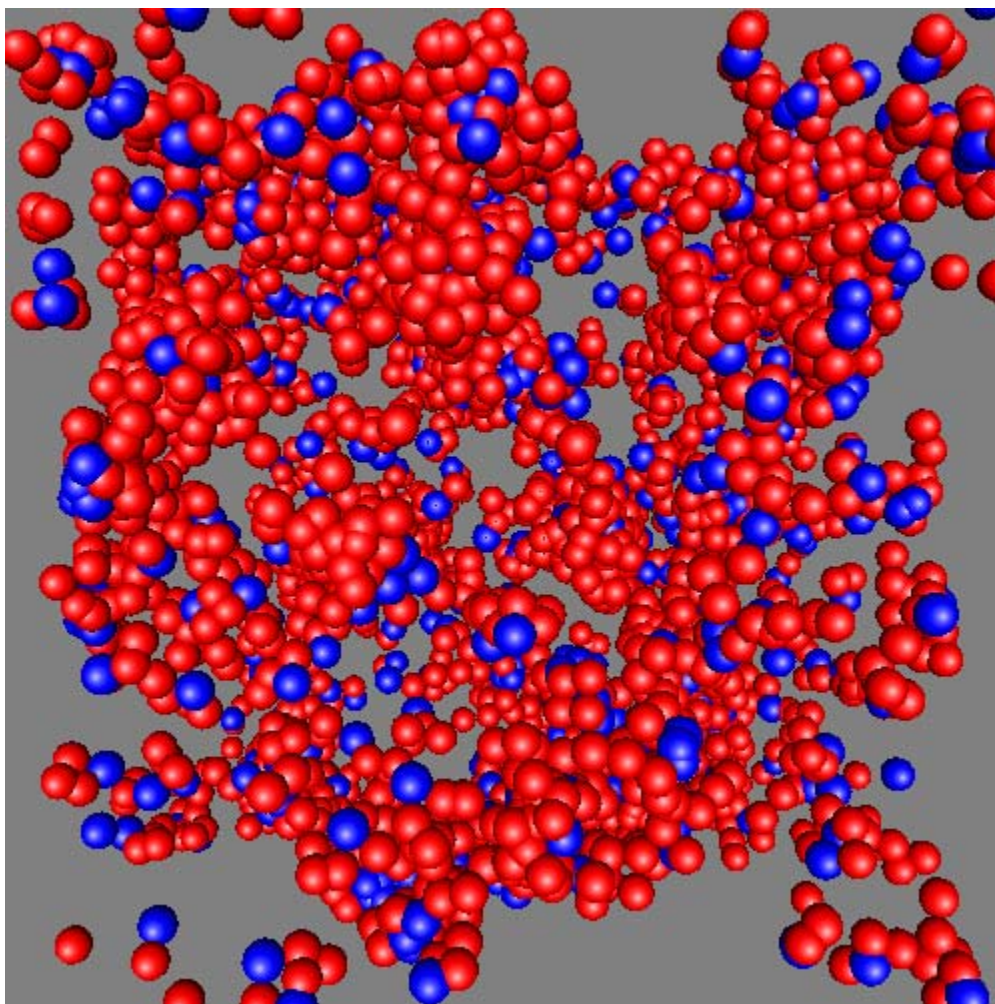
Figure 3.8 Simulation snapshot of surfactants forming micelles in polymer melt. Polymers are not shown for clarity.

3.5.3   Effect of Surfactant Concentration

The number of surfactant molecules in the PNC system is systematically varied to consider the effect of surfactant concentration on nanoparticle dispersion. This effect is later quantified by means of the potential energy and the specific heat. We have considered 3 different values for the concentration of surfactants: 1.6wt%, 3.2wt% and 6.4wt%.

Figure 3.9 shows the potential energy as a function of filling fraction for different values of surfactant concentration. We see that the potential energy decreases with an increase in the surfactant concentration. Smaller values of the potential energy indicate weaker attraction (Figure 3.9). There is no significant difference between the two cases of higher concentration, which suggests that an optimum surfactant concentration was obtained. In the presence of surfactants, the transition boundary is shifted to a larger value of the filling fraction, showing that it is easier for the system to maintain a dispersed state even when there are more nanoparticles embedded in the polymer matrix. The range of dispersed state expands. The approximate boundary between clustered and dispersed states is shifted accordingly in the presence of surfactants. Surfactant molecules act as a separator to avoid nanoparticle clustering, especially when surfactants are in excess. The addition of oleyl alcohol reduces the effective attraction between the nanoparticles, further weakening the agglomeration, which was monitored via particle-particle contribution to the potential energy and the specific heat. Our results show that, for a surfactant concentration of greater or equal than 6.4 wt%, the particles remain in a homogeneously dispersed state, which is consistent with experimental findings.

(a)
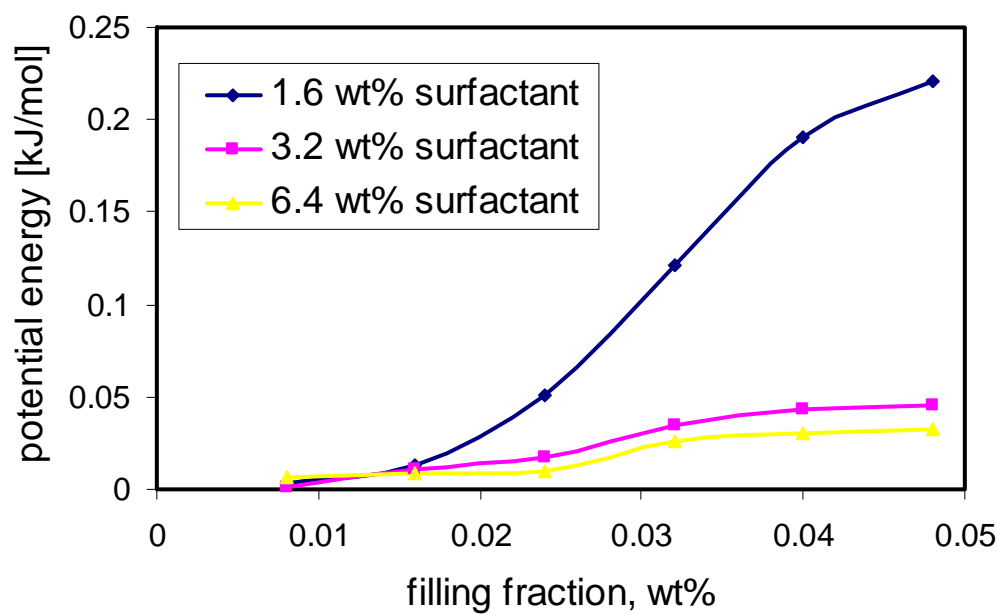
(b)
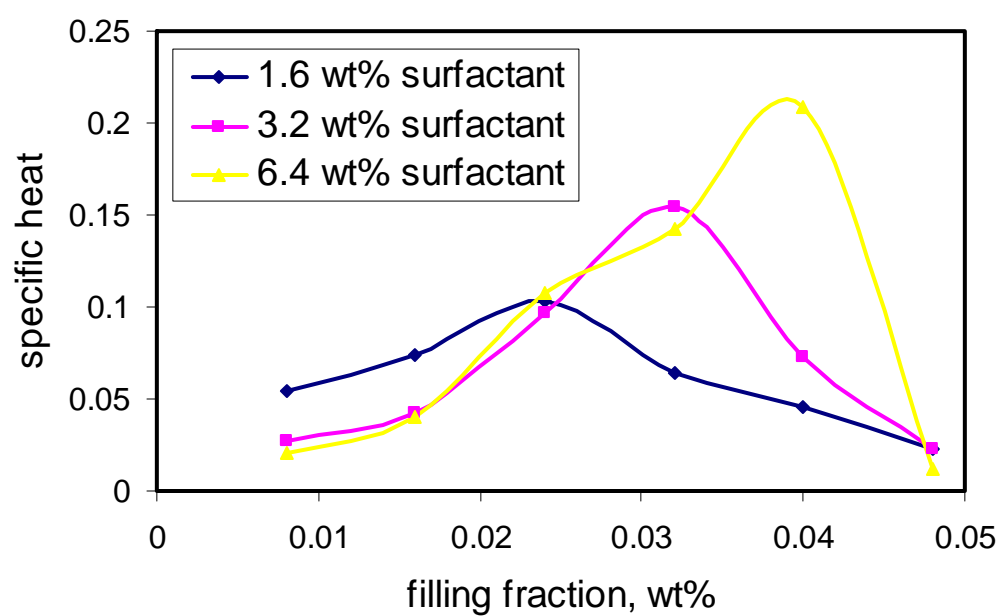
Figure 3.9 Potential energy (a) and specific heat (b) as a function of nanoparticle filling fraction for different surfactant concentrations.

3.6   Summary

In this chapter, we use the coarse-grained model developed in the previous chapter to study the dispersion of silica nanoparticles in a polyethylene matrix at 423K. The RDF and specific heat calculations indicate that for filling fractions smaller than 3 wt% the system is in a dispersed state and for filling fractions of approximately 3 wt% and larger the nanoparticles show agglomeration. We show that a thermodynamically stable dispersion of nanoparticles into a polymer melt is enhanced for systems where the radius of gyration of the linear polymer is greater than the radius of the nanoparticle. Dispersed nanoparticles swell the polymer chains, and as a consequence, that the polymer radius of gyration grows with the nanoparticle filling fraction. Polymer-mediated forces are also more repulsive in the case of longer chains than in the case of shorter ones.

CHAPTER 4

NANOPARTICLE DEAGGLOMERATION IN SUPERCRITICAL CARBON

DIOXIDE

In this chapter we report molecular simulation studies on the interaction forces between silica nanoparticles in supercritical carbon dioxide at 318K. The simulation technique is similar to the one in the previous chapters, and the system consists of, again, silica nanoparticles but a different fluid – supercritical carbon dioxide. Our goal here is to find a better understanding of the interparticle solvation forces during rapid expansion of supercritical solutions (RESS). The parameters for interatomic potentials of fluid-fluid and solid-fluid interactions are obtained by fitting our simulations to (i) experimental bulk CO_2 phase diagram at a given temperature and pressure and (ii) CO_2 sorption isotherms on silica at normal boiling and critical temperatures.

In what follows, Section 4.1 gives the introduction on the RESS process and a literature search on the studies about interparticle forces. Section 4.2 introduces the molecular models for both CO_2 and silica nanoparticle, and the method for establishing fluid-fluid and solid-fluid force field parameters from thorough comparison between MC and experimental adsorption data for CO_2 on nonporous silicas. The simulation details are also explained. Section 4.3 presents the solvation forces that are direct calculated between two small (2.2nm) nanoparticles at both subcritical and supercritical conditions. In Section 4.4, we investigate the deagglomeration of nanoparticles under shear flow using non-equilibrium MD.

4.1 Introduction

Nanoparticles are widely employed to obtain materials with unique mechanical, optical, electrical and magnetic properties that arise from small size and high surface area, and chemical activity. However, because of these same properties, nanoparticles easily aggregate, becoming unusable for the synthesis of nanoparticle-based composites or critically altering the properties of already existing materials. Currently, most popular methods of nanoparticle deagglomeration essentially rely on shearing of nanoparticle suspensions in organic solvents [10, 36], and often facilitated by surfactants/dispersants [11, 37]. Another promising deagglomeration technique is the rapid expansion of supercritical solutions (RESS). A schematic diagram of the RESS procedure is shown in Figure 4.1. In the first stage, the agglomerates of primary particles are saturated with supercritical fluid; the gas penetrates inside the pores of the agglomerates. Then after rapid depressurization, the agglomerate is broken down by the extreme pressure gradients and fluid velocities. RESS is an environmentally benign technique that allows reducing the use of volatile organic solvents and is well established for the synthesis of micron- and sub-micron size particles [3]. However, the interaction forces between nanoparticles in the RESS technique are not completely understood, especially when the particles are at the nanoscale.
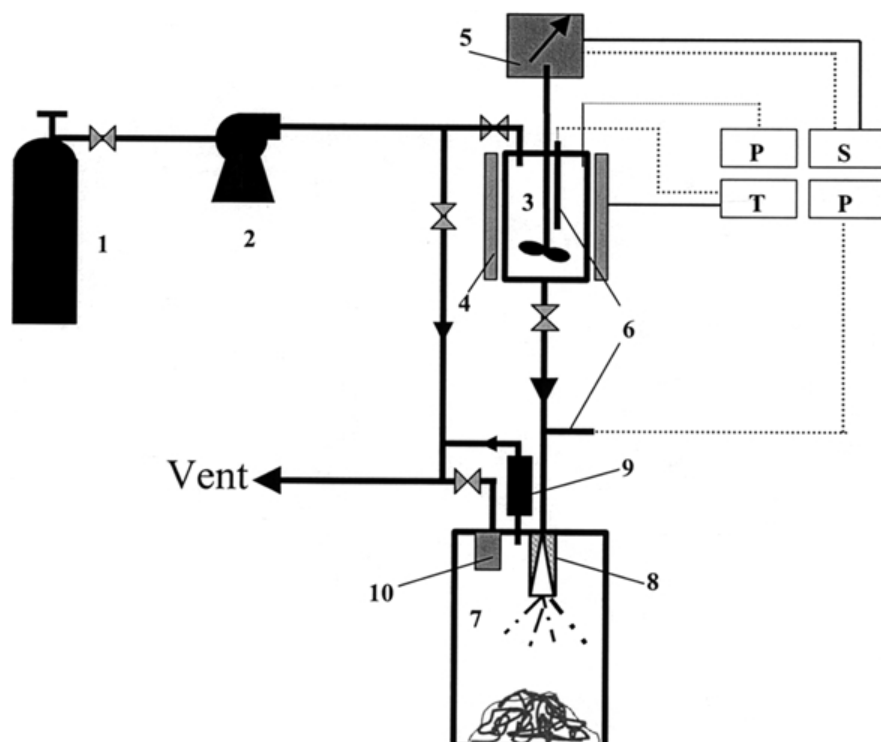
Figure 4.1 Schematic of RESS process. (1) CO_2 cylinder (2) Pump (3) Reactor (4) Heating jacket (5) Stirring system (6) Thermocouple (7) Receiving tank (8) Spray nozzle (9) Release valve (10) Filter

The total force between particles in nanoparticle suspensions can be obtained as a sum of direct forces (forces between identical nanoparticles which are identically/evenly located in vacuum) and solvation forces (forces originated from the interactions between nanoparticles and the solvent). Atomic force microscopy (AFM) and surface force apparatus (SFA) are powerful techniques for experimental measurements of the solvation forces [38]; but the application to nanoparticles is technically complicated. Molecular simulations, such as Monte Carlo (MC) and molecular dynamics (MD), can be useful for resolving the forces between nanoparticles. So far most simulation studies of colloidal nanoparticles in the literature are aimed at understanding the hydration forces between nonpolar solutes in water [39]. MC and MD simulation methods have also been used previously to explore the solvation forces in slit-like pore fillers with hard spheres, Lennard-Jones (LJ) fluids, water, alkanes [40, 41] and polymers at "gas like" and "liquid like" polymer densities [42]. A few recent papers report MD modeling of two nanoparticles in Lennard-Jones (LJ) and soft-sphere fluids. Shinto et al. have varied the solid-fluid interactions to study the van der Waals and solvation forces between liophobic and liophilic nanoparticles [43, 44]. Qin and Fichthorn also performed similar studies in which they represented the nanoparticles as rigidly fixed clusters of LJ atoms and determined the effect of particle size, shape, and roughness on the solvation forces [45, 46]. The force profiles between two nanoparticles obtained in all these studies are similar in form to those predicted for fluids confined between flat and infinite surfaces (attractive for lyophobic and oscillatory for lyophilic nanoparticles) [47-49]. Bedrov et al. simulated solvation forces between fullerenes and carbon nanotubes in water and found deviations from standard hydrophobic behavior [50]. Other simulation studies have considered the

capillary forces between rough surfaces with the inclusion of the formation of liquid bridges [51, 52].

In summary, most of the published work has been focused on the solvation forces between nanoparticles in vapors and liquids, but not in supercritical fluids. In vapors, the adsorption field of the two bodies typically leads to the formation of a liquid-like junction between them [13, 14]. In these cases, solvation forces can be interpreted in terms of the surface tension of the formed meniscus, and essentially the forces vanish when the liquid junction breaks up. The other group of simulation studies deals with solvation forces between planar surfaces and particles in liquids and polymers. Neither of these groups considers the dense supercritical fluids, where meniscus formation is not really possible (unlike vapors), but strong density variations are (unlike liquids).

In this work, we calculate the solvation forces between two silica nanoparticles in CO_2 at supercritical temperature $T = 318K$ and near-critical pressure of $p = 69atm$ (the critical point of CO_2 are $Tc = 304.1K$ and $pc = 72.8atm$ [53]). We analyze the available experimental data on CO_2 interaction with silica surfaces and choose carefully the models and parameters for fluid-fluid and solid-fluid interactions. The system is similar to the one considered in Ref. [12], but our nanoparticles are smaller (2.2nm) because of computational expenses. For larger nanoparticles, like those studied in Ref. [12] is also considered using an indirect approach.

4.2   Molecular Models and Simulation Details

4.2.1 CO_2 Models

We followed a well-established approach for choosing intermolecular potentials [54]: the fluid force field is chosen to reproduce the bulk phase diagram at similar conditions, while the solid-fluid interactions are fitted to the experimental sorption isotherms on non-porous or mesoporous surfaces. Several molecular models reproduce the experimental conditions of vapor-liquid equilibrium of bulk CO_2 [55, 56]. In this work, we used a model proposed by Möller and Fischer [57] (from now on referred to as the dumbbell model), which combines two LJ pseudo atoms connected by a rigid bond with a point quadrupole located in the center. The parameters are listed in Table 4.1. This model described accurately the liquid-vapor equilibrium properties and the saturation pressures of bulk CO_2 at subcritical temperatures [58, 59]. We performed a series of gauge cell MC [60, 61] and constant-pressure (NPT) MD simulations of bulk CO_2 at $T =$ 323.15K and $p < 105$atm with the dumbbell model and verified that the model reproduces reasonably well the bulk PVT data (see Figure 4.2) [62]. We also employed a simpler LJ model for bulk CO_2. Carbon dioxide cannot be considered as a LJ fluid mostly because the LJ potential cannot account for the anisotropic quadrupole-quadrupole interactions. However, it is possible to account for the electrostatic interactions effectively via Boltzmann averaging [63] and use temperature-dependent LJ energy parameters ε_{ff} [64]. Here, we obtained the LJ parameters (σ_{ff} and ε_{ff}) for CO_2 by fitting the Johnson's equation of state [65] for LJ fluid to the experimental bulk isotherm at 323.15K [62]. The simple LJ model gives excellent agreement with the experimental isotherm up to very high pressures (see Figure 4.2).

Table 4.1 CO_2 models and interaction parameters.

fluid	CO_2					N_2	
fluid model	Dumbbell				LJ	LJ	
ε_{ff}/k, K	125.3				286.2	101.5	
σ_{ff}, Å	3.035				3.68	3.6154	
Q^{*2}	3.0255				---	---	
l, Å	2.121				---	---	
r_c, Å	15.175				9.2	18.077	
solid model	Spherical Shell				FCC	Sph. Shell	FCC
hydroxylation	high	medium	dehydroxyl	high	high	---	---
$\rho\varepsilon_{sf}/k$, Knm^{-2}	2515	2353	1931	3112	---	799	---
σ_{sf}, Å	3.217	3.217	3.217	3.43	3.43	3.494	3.17
ε_{sf}/k, K	---	---	---	---	269	52.22	147
Δ, Å	---	---	---	---	2.55	---	2.55
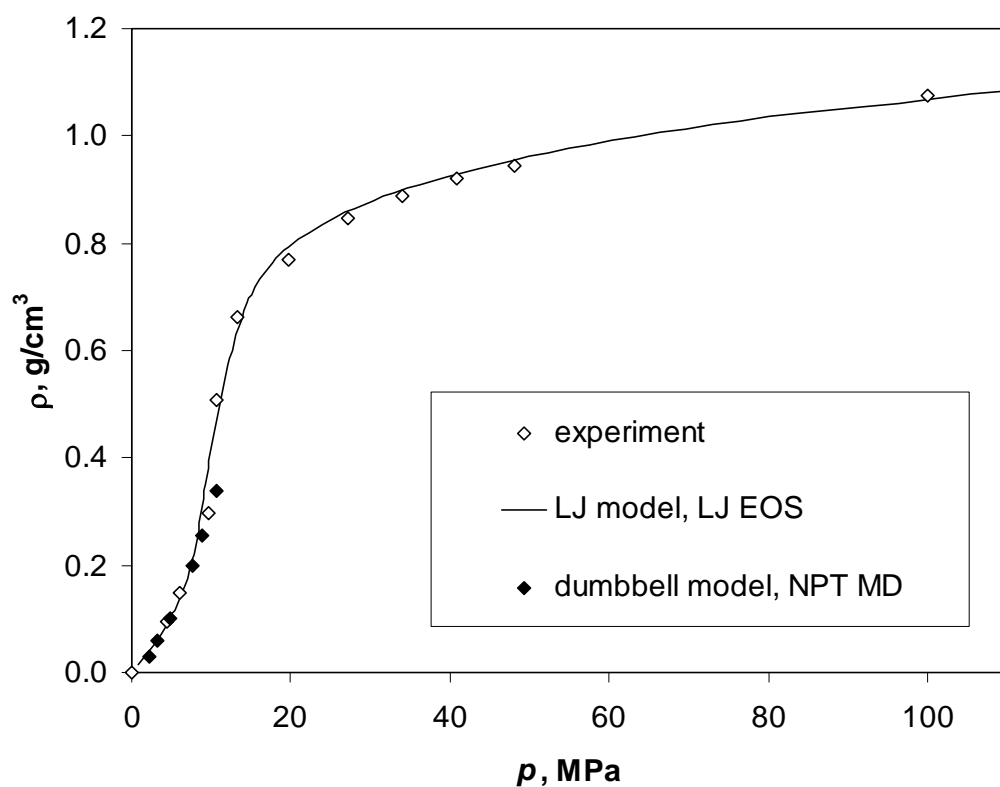
Figure 4.2 CO_2 bulk isotherm at T = 323.15K. Experimental data from Ref. (Span and Wagner 1996). The data for LJ model obtained using LJ equation of state (Johnson, Zollweg et al. 1993). The isotherm for the dumbbell model was obtained using constant-pressure MD simulations.

4.2.2 Solid-Fluid Interactions

In our work the interactions between CO_2 molecules and silica are quantified in terms of CO_2 sorption isotherms on the nonporous or mesoporous silica surfaces. A detailed review on different types of silica surfaces can be found in Ref. [66]. Published experimental data about the adsorption of CO_2 on silica surfaces include: (i) isotherms at normal boiling point $T > 195K$ and $p < 1atm$ [67-69] and (ii) isotherms at elevated temperatures $T \geq 273K$ and at atmospheric and higher pressures [70-72]. These isotherms reveal that sorption of CO_2 gas strongly depends on the degree of silica surface hydroxylation (that is, the surface density of accessible hydroxyl groups) due to hydrogen bond formation between the surface hydroxyls and CO_2 oxygen atoms. The hydroxylation depends on the process conditions of synthesis, thermal treatment, and subsequent modification via grafting or presorption. In strongly hydroxylized silicas, the concentration of hydroxyl groups reaches 4.6 nm^{-2} [66, 73]. Katoh et al. [70] systematically studied the effect of silica hydroxylation on CO_2 sorption on the folded sheets mesoporous (FSM) silicas, varying the number of hydroxyl groups from 0.7 to 3.5 nm^{-2} (from 3.3 to 6.4 nm^{-2} according to Ref. [74]). Detailed comparison of the CO_2 isotherms on silicas from different sources [67, 69-72, 75] is given in Figure 4.3 (a) and (b). A few more isotherms at both cryogenic and critical temperatures are also given in Figures 4.4 (a) and (b).

At normal boiling temperature of 195K, CO_2 exhibits a sub-monolayer region (Figure 4.3 a), followed by a distinct monolayer formation and then by capillary condensation in meso- and macro- pores [67, 68]. However, a distinct transition attributed to monolayer formation, which is well established on crystalline samples such

as graphite [76], is not seen on amorphous silicas, also because of their surface heterogeneity. At all hydroxylation levels, the CO_2 isotherm at near-critical temperature (303K) shows sub-monolayer sorption region (Figure 4.3b). The isotherms on weakly hydroxylated samples (FSM-14 and FSM-16) are practically linear, suggesting that the sorption does not go beyond the Henry region, where the sorbent concentration on the surface is proportional to that in the equilibrium bulk. On strongly hydroxylated silicas (FSM-10 and FSM-12), the isotherms show pronounced non-linearity, which may originate from surface heterogeneities, which are most likely due to the distribution of hydroxyl groups.
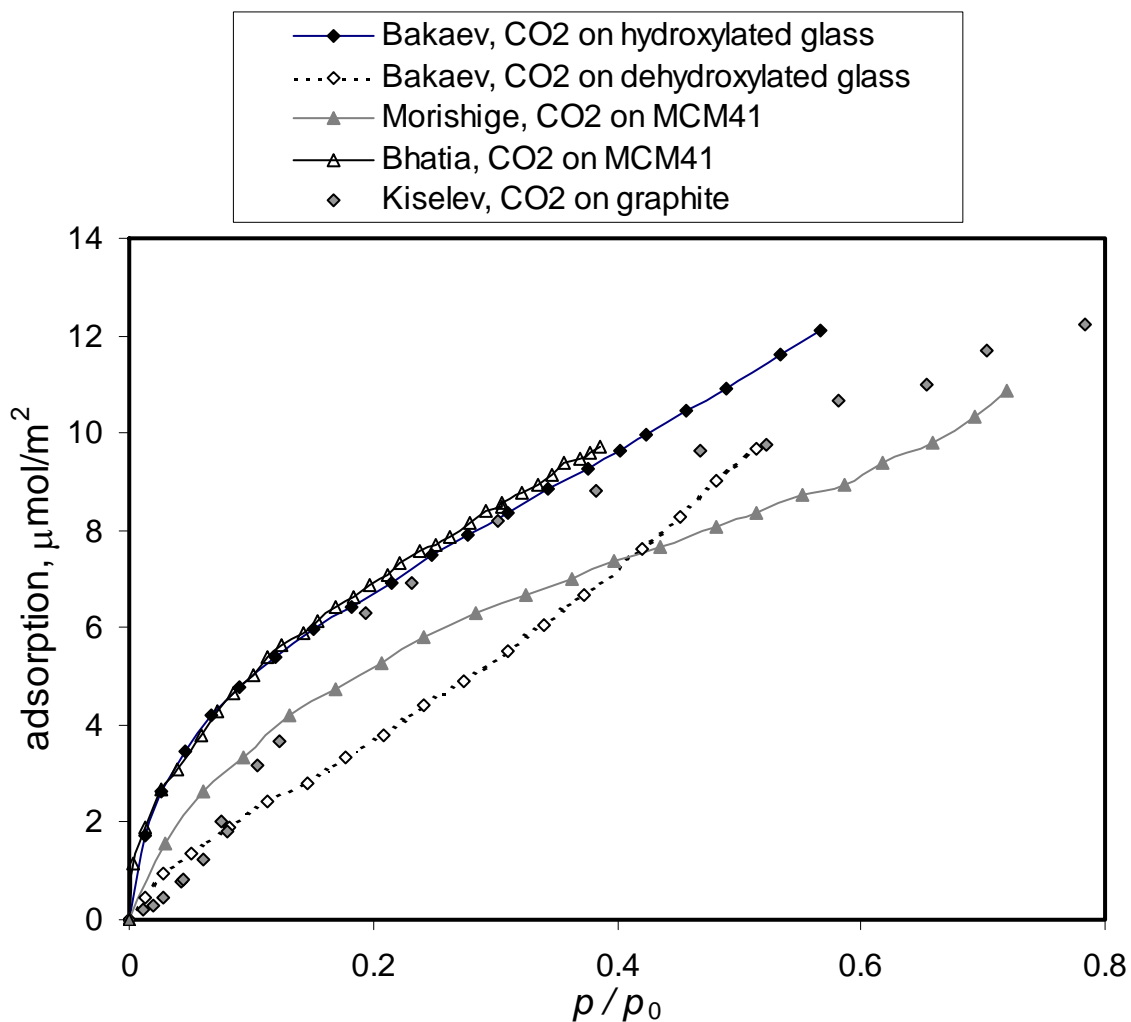
Figure 4.3 (a) Experimental isotherms of CO_2 on amorphous silica and graphite surfaces at the normal boiling temperature (195K), data taken from Refs. (Beebe, Kiselev et al. 1964; Morishige, Fujii et al. 1997; Sonwane, Bhatia et al. 1998; Bakaev, Steele et al. 1999).
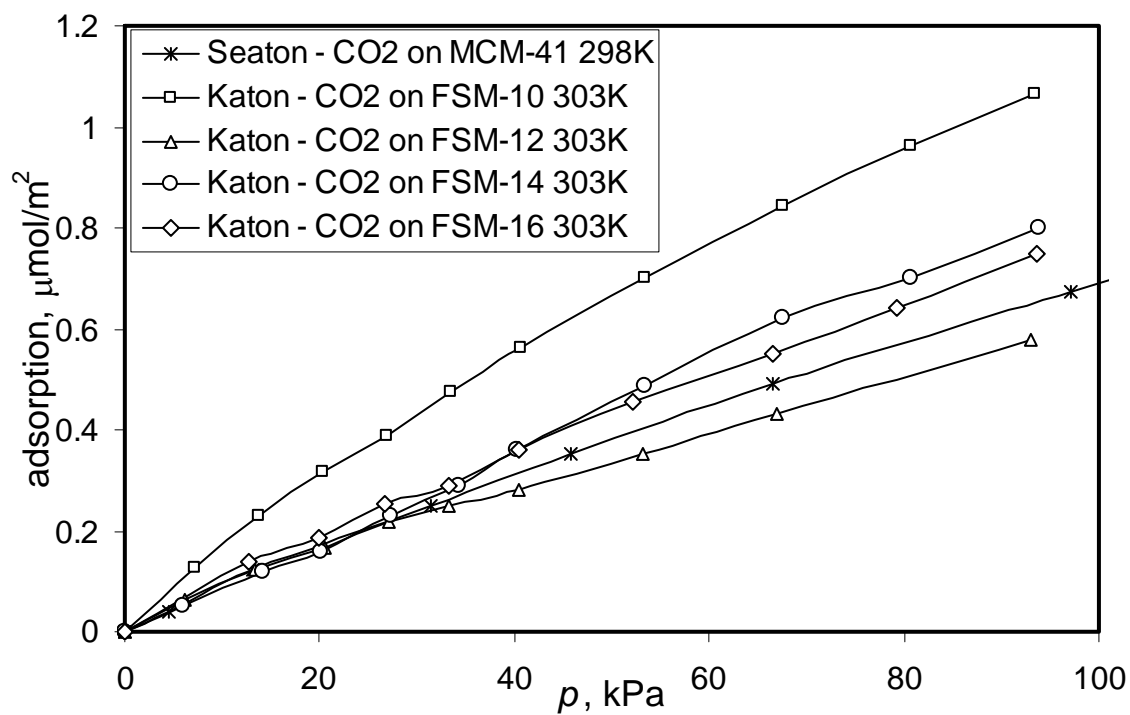
Figure 4.3 (b) Experimental isotherms of CO_2 on MCM-41 at T = 298K (He and Seaton 2006) and on different FSM crystals at T = 303K.

A comparative analysis of the isotherms obtained by different authors on different samples shows substantial differences in monolayer density. In particular Sonwane et al. [68] measured CO_2 sorption in MCM-41 mesoporous molecular sieves. Although qualitatively the isotherms are very similar, the CO_2 amount per unit area adsorbed at same pressures differs significantly (the isotherms scale almost exactly by a factor of 1.33 in the entire pressure range below capillary condensation). This difference cannot be explainable by the fact that there might exist an inconsistency in the definition of the surface area or in evaluation procedures; at least. Pore size and volume measurements are consistent with the surface areas obtained in both works. The CO_2 sorption isotherm on glass fibers reported by Bakaeva et al. [77] has very close values to the isotherm of Sonwane et al. [68] (Figure 4.3b). In this case, we decided to use the average of the three isotherms as a reference. The monolayer density of isotherm from Ref. [68] is close to that on graphitized carbon blacks (Figure 4.3a).

4.2.3   Models for Silica Nanoparticles

In this work, we employ two different models for silica nanoparticles. The first model, used in the grand canonical Monte Carlo (GCMC) simulations, consists of a spherical shell of implicit LJ centers, which are uniformly distributed over the nanoparticle surface (Figure 4.5a). For a LJ fluid located at a distance h from the center of a particle of radius R, the integration of the LJ potential gives the following expression for the fluid-particle interaction energy:

$$U_{sf}(R,h) = 2\pi\rho_s\varepsilon_{sf}\sigma_{sf}^2\left(\frac{R}{h}\right)\left[-\frac{2}{5}\left(\frac{\sigma_{sf}}{R+h}\right)^{10} + \frac{2}{5}\left(\frac{\sigma_{sf}}{R-h}\right)^{10} + \left(\frac{\sigma_{sf}}{R+h}\right)^{4} - \left(\frac{\sigma_{sf}}{R-h}\right)^{4}\right]$$

(4.1)

where ρ_s is the surface density of the LJ atoms distributed over the nanoparticle surface,

ε_{sf} and σ_{sf} are the LJ parameters for the solid-fluid interactions (both LJ centers of the

dumbbell model interact with the silica surface). This potential reduces to the 10-4 form

of Steele (Steele 1974) potential at $R \rightarrow \infty$, i.e. for a planar surface.

(a)

(b)
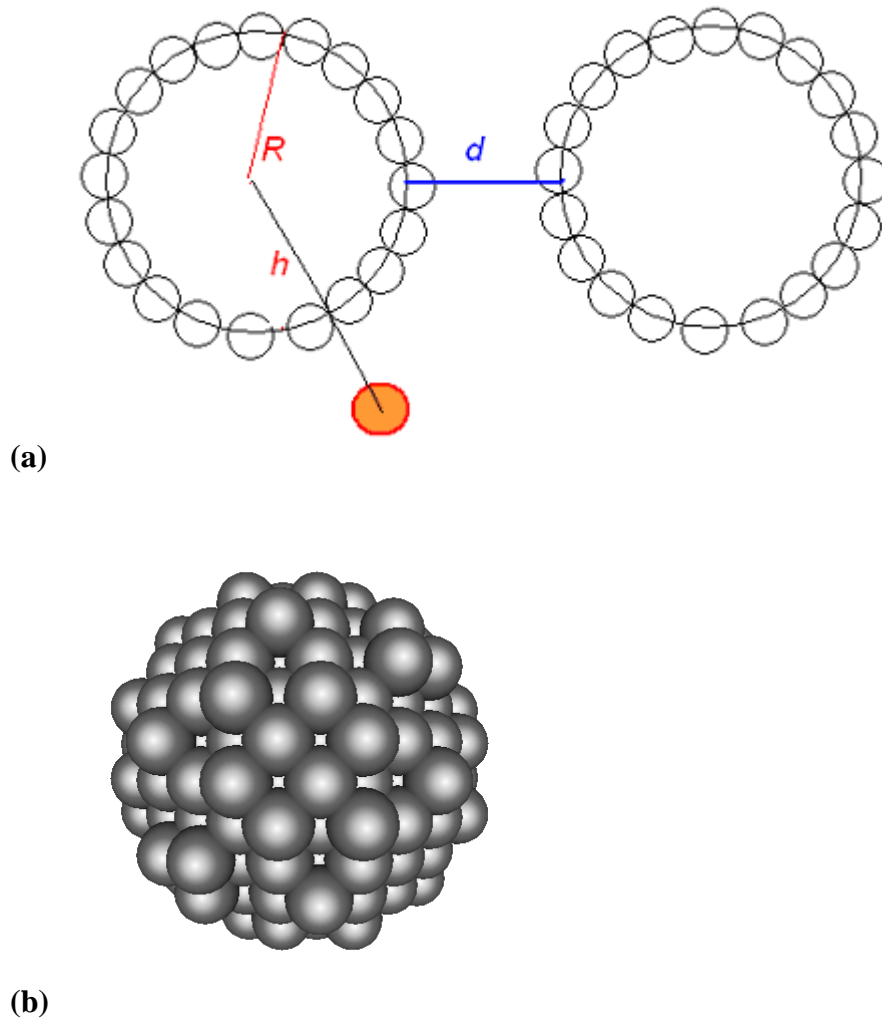
Figure 4.4 Schematic of silica nanoparticle model: (a) spherical layer of implicit LJ (b)

units spherical cluster of LJ units arranged in an FCC structure.

In order to examine how the solid-fluid interactions affect interparticle solvation forces, we used three different values of ε_{sf} for the dumbbell model, which accounts for the hydroxylation factor. We evaluated $\rho\varepsilon_{sf}$ and σ_{sf} by fitting the simulated isotherms at a uniform flat surface to the experimental isotherms data at two temperatures: $T = 195K$ and $T = 303K$ [54, 64, 76]. The low-temperature isotherms are shown in Figure 4.5 (a). Here, the GCMC isotherm shows a visible transition corresponding to the formation of an adsorbed monolayer, which is smeared out in experiments because of surface inhomogeneities. However, the overall agreement between simulated and the reference isotherm is very reasonable, and the monolayer capacity agrees well and is close to that of the graphite surfaces [64, 76, 78]. Figure 4.5 (b) displays GCMC [79] isotherms at $T = 303K$. In this case, the solid-fluid potentials were uniform, i.e. the silica surfaces do not have inhomogeneities (the role of inhomogeneities will be considered later). However, the first set of parameters ($\rho\varepsilon_{sf}/k = 2515Knm^{-2}$) reproduced reasonably well the experimental isotherm on a strongly hydroxylated FSM-10 silica surface (3.5 hydroxyl groups per nm^2, Figure 4.4b). Lower ε_{sf} were used to model CO_2 sorption on silicas with medium level of hydroxylation, here represented by FSM-12 silica, and the dehydroxylated surface.
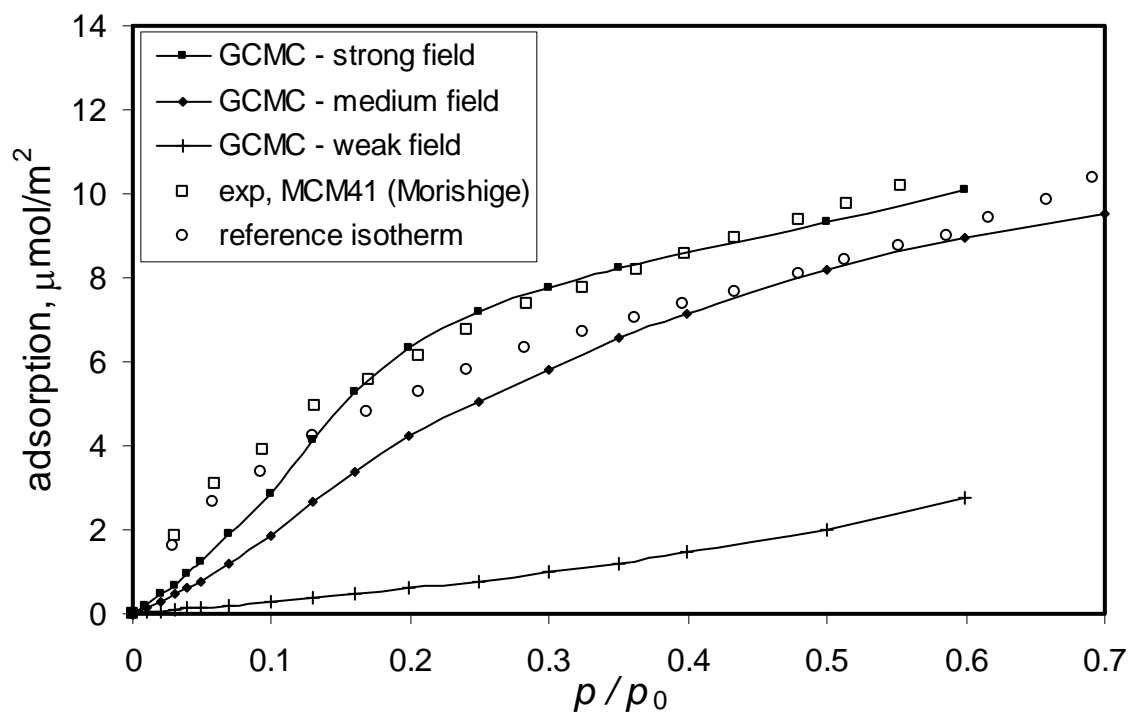
Figure 4.5 (a) The experimental and simulated isotherms at flat surfaces at the normal boiling temperature of 195.5K.
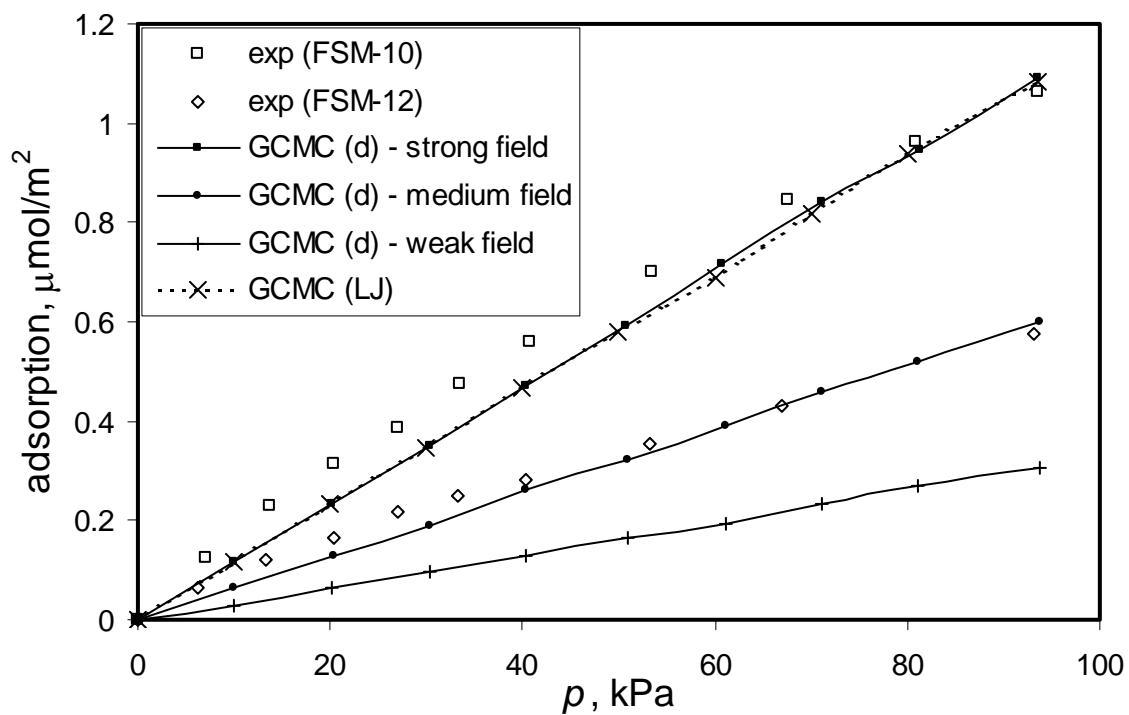
Figure 4.5 (b) CO_2 sorption isotherms at mesoporous amorphous silicas of strong (FSM-10) and weak (FSM-12) hydroxylation and GCMC isotherms at T = 303K. The letters in brackets denote the fluid model used (d – dumbbell and LJ – Lennard-Jones).

The procedure for deriving the parameters was repeated with the LJ model of CO_2 molecule. Here, we only targeted the strongly hydroxylated surfaces. We fitted the parameters of 10-4 potential for the LJ model of CO_2 to the experimental isotherm on FSM-10 [70] at 303K, which is shown in Figure 4.5b. We did not calculate the low-temperature isotherm, since the LJ model of CO_2 does not give reliable results for CO_2 monolayer adsorption [54, 64]. The resulting potential for the interaction between silica nanoparticles and CO_2 molecules is shown in Figure 4.6 together with the corresponding 10-4 potential. From this figure we can observe that the minimum of the sorption potential for the flat surface is much deeper than the curved surface. The reason is simply that more adsorption sites are available on a flat surface than on a curved surface, which contributes to the stronger attraction.
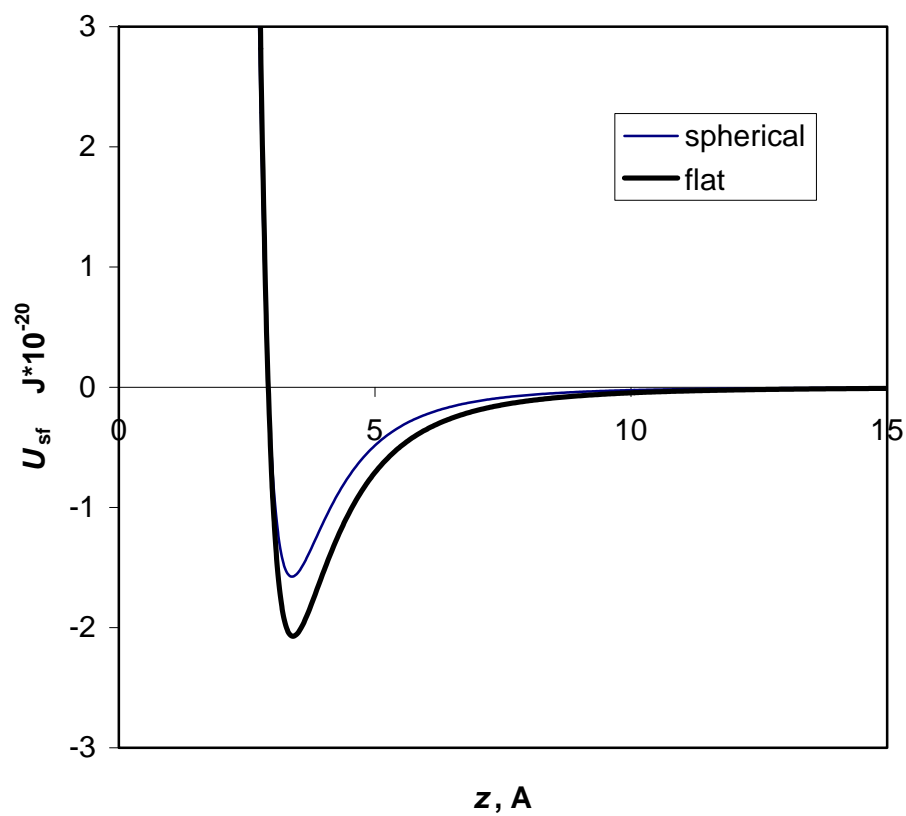
Figure 4.6 Potential of a CO_2 molecule modeled by a LJ model in the vicinity of a spherical nanoparticle.

The second model for silica nanoparticle has the same size of 2.2nm. It is composed of 276 silica LJ pseudoatoms arranged in a face cubic center (FCC) lattice (Figure 4.4b). The solid-fluid interaction energies were calculated via direct summation of the LJ between fluid molecule and silica pseudoatoms. When the solid particle becomes infinitely large, the interaction energy can be approximated using the 10-4-3 potential of Steele (Steele 1974):

$$U_{sf}(z) = 2\pi\rho_s\varepsilon_{sf}\sigma_{sf}{}^2\Delta\left[-\frac{2}{5}\left(\frac{\sigma_{sf}}{z}\right)^{10} + \left(\frac{\sigma_{sf}}{z}\right)^4 - \frac{\sigma_{sf}{}^4}{3z(z+0.61\Delta)^3}\right]$$

(4.2)

where ρ_s is the *volume* density of the LJ pseudoatoms in the lattice, Δ is the distance between the layers in the lattice, ε_{sf} and σ_{sf} are the LJ parameters for the solid-fluid interactions, z is the distance between the fluid molecule and the plane that contains the centers of the pseudoatoms of the surface layer of the FCC lattice (z is similar to *R-h* in Eq. 4.1). For our FCC model, ρ_s=0.03Å^{-3}, Δ = 2.55 Å. The solid-fluid parameters σ_{sf} and ε_{sf} were found by fitting the GCMC isotherms at a flat surface with the referenced experimental isotherms (Figure 4.5a). These parameters are listed in (Table 4.1). Both the spherical shell model and the model composed of silica pseudoatoms have their advantages and problems. The spherical shell model is more efficient computationally but is essentially a hollow particle and has a uniform surface. The FCC model has no such shortcomings, but its structure is artificially regular and the LJ potential is truncated at the cutoff distance of 2.5σ_{ff} (same as the fluid-fluid potential), which is also unrealistic.

For comparison, we also measured the solvation forces in a LJ fluid that mimic nitrogen at its normal boiling point 77.4K. We used a spherical shell model with fluid-fluid parameters were taken from Ref. [54]; and the solid-fluid parameters were taken

from Ref. [80, 81]. All the parameters are listed in Table 4.1. A similar spherical shell

model was used for the surface of a silica pore and good agreement with experimental

sorption isotherms was achieved.

4.2.4   Simulations of Bulk Fluid

Simulations of bulk CO_2 were involved in the verification of the fluid-fluid

parameters. Utilizing the dumbbell model of CO_2, we conducted a series of gauge cell

MC and constant-pressure MD simulations of bulk fluid at T = 323.15K. The MD

computations were performed using a parallel MD code, MDynaMix version 4.4 [82].

Constant number of particles, pressure and temperature (NPT) ensembles were employed

to study the dependence of the density on pressure. The equilibration time was about

300ps, and then statistics were collected over 500ps.

4.2.5   Gauge Cell Method

The relation between density and chemical potential that is necessary for GCMC

simulations of solvation forces was performed using the mean density gauge cell method

as implemented in SORSIM1.0 program [83]. The equilibration was performed over the

first 20,000 steps per molecule and the average properties were collected over additional

20,000 steps per fluid molecule. The same procedure was applied for the fitting of the

solid-fluid parameters. The latter were performed in a $20\sigma_{ff}$ slit pore with lateral

dimensions of 12×12 σ_{ff}^{2} .

4.2.6   Simulations of Silica Nanoparticles with CO_2 Fluid

In order to calculate the solvation forces between the nanoparticles, two nanoparticles were placed in an orthorhombic box of $30 \times 30 \times 30$ σ_{ff}^{3} (minimum) to $40 \times 40 \times 50$ σ_{ff}^{3} (maximum). Typical simulation included 2,000 to 6,000 CO_2 molecules. The constant number of particles (N), volume (V) and temperature (T) MD technique was applied with the FCC nanoparticle model. The distance between the centers of nanoparticles was fixed, but the positions of individual silica pseudoatoms in the simulations performed with FCC nanoparticle model were allowed to fluctuate.

A strict approach for measuring the nanoparticle interactions in supercritical solvent should focus on finding an effective Hamiltonian dependent only on the concentration and coordinates of nanoparticles and the fugacity of the solvent but not on the coordinates of the solvent molecules. Monte Carlo simulations of an ensemble of nanoparticles with this Hamiltonian would sample configurations identical to those sampled in a full atomistic simulation of the corresponding system with explicit solvent. This mapping of a partition function of a simplified system onto that of full atomistic system was applied to asymmetric mixtures of hard spheres [41] and simple Lennard-Jones mixtures [84]. However, its application to more complex systems as the one considered here is very complicated. Here, we employ simplistic mechanical approach by defining the solvation force as the average effective force acting to increase nanoparticle separation. Because the direct interaction between the nanoparticles are not included into the solvation force, it may be calculated simply as $F_s = \left\langle \sum\limits_{i=1}^{N} \sum\limits_{j=1}^{M} l_j f_{ij} \right\rangle$, where N is the number of fluid molecules, and M is the number of silica pseudoatoms in one nanoparticle (M = 1 for the spherical shell model), and the angular brackets denote the

averaging over ensemble. Here, f_{ij} is the force between fluid molecule i and pseudoatom j, l_j is a coefficient that equals 1 if the pseudoatom j belongs to the first nanoparticle and l_j = -1 if j belongs to the second nanoparticle. Each MD simulation lasted for 1.5ns. The solvation force was averaged over the last 1ns of simulation run. The simulation setup was similar for obtaining the force in the GCMC simulations. The total number of attempted steps was 30,000 per molecule. In all GCMC simulations we used the original algorithm of Norman and Filinov [79]; one insertion and one removal were attempted per one displacement/rotation.

4.3   Solvation Forces Between Nanoparticles

4.3.1   Under Subcritical Conditions

First we placed two nanoparticles in a subcritical vapor of LJ fluid at kT/ε = 0.762, modeling nitrogen at 77.4K. The parameters for the solid-fluid interaction have been obtained and validated in the previous studies. The pressure was kept at a constant value, p = 0.38p_0 . Under these conditions the fluid forms a monolayer on the surface of each individual particle, and the particles are surrounded by low density nitrogen vapor. When two particles are in contact, the monolayer covers both particles, and a liquid-like neck starts to form around the point of contact. When the separation increases, the liquid junction breaks and the particles become completely separated (Figure 4.7).
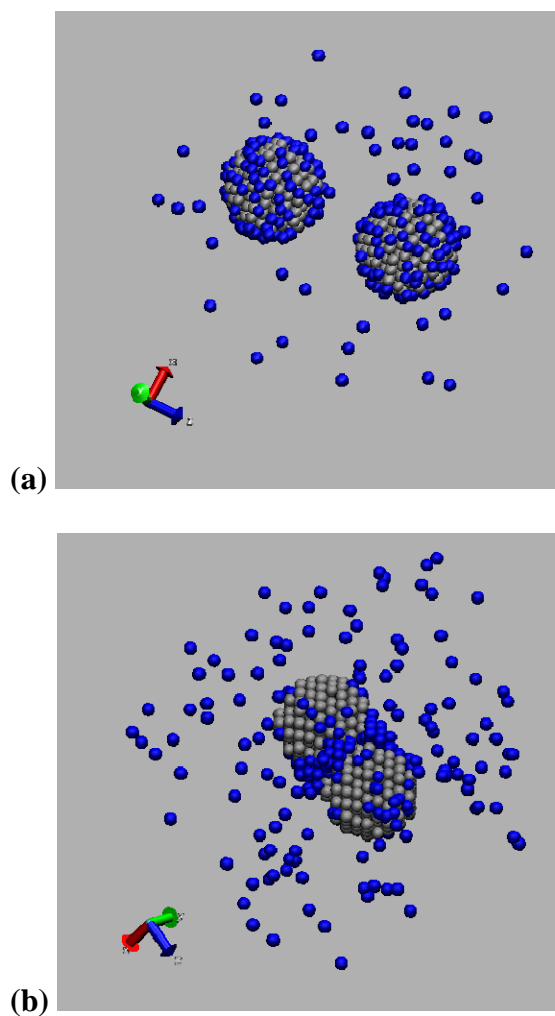
Figure 4.7 Simulation snapshots of two nanoparticles in subcritical liquid nitrogen separated (a) and at contact (b) obtained from MD simulations using FCC nanoparticle model. Fluid adsorbs at the particles, surrounded by rare gas. A liquid junction is formed between the particles when they are close enough and breaks when the distance increases.

The solvation force is strongly repulsive because of the layering near the points of contact, which has been well documented in slit pores and corners [47, 48]. As the distance increases, a distinct liquid junction is formed. This can be expressed in terms of the excess number of fluid molecules, which is defined by equation $\Delta N_{ex} = \overline{N} - V\rho_{bulk}$, i.e. the average number of the fluid molecules in the simulation cell minus the average number of molecules in the same volume of the equilibrium bulk fluid (Figure 4.8a). We see that ΔN_{ex} increases with the increasing of interparticle distance, because of the gradual elongation of the junction; the oscillations of the dependence of ΔN_{ex} on d demonstrate that fluid layering in the junction is visible even with particles as small as approximately six molecular diameters. The junction gradually breaks at $d = 1.0$ to 1.5nm. The continuous nature of the snap-off indicates an absence of a substantial potential barrier associated with the junction breakup.
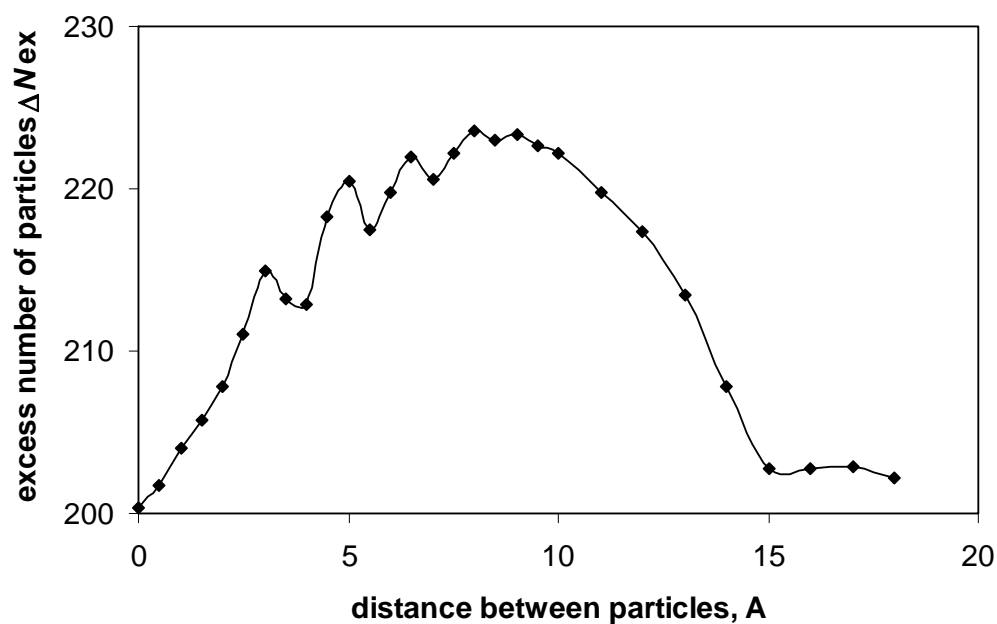
Figure 4.8 (a) Excess number of fluid particles as a function of nanoparticle separation under subcritical conditions, T = 77.4K, p = 0.38p0. The fluid is modeled as LJ particles with parameters listed in Table 4.1.

The interparticle force in Figure 4.8 (b) becomes attractive as soon as the distance exceeds the diameter of a single molecule. Interestingly, this happens at smaller separations when the FCC model is used. It is possibly due to that the particles reorient and form a commensurate configuration. In both GCMC and MD simulations, the force shows two minima at approximately 0.5 and 1.0nm. This non-monotonic behavior is reproducible with the spherical shell and the FCC models. The second minimum roughly corresponds to the maximum of ΔN_{ex} ; this is where the junction starts to break up. As the distance increases, ΔN_{ex} becomes constant (corresponding to two monolayers on the surfaces of two distant nanoparticles) and the solvation force approaches zero at $d_0 =$ 1.5nm.
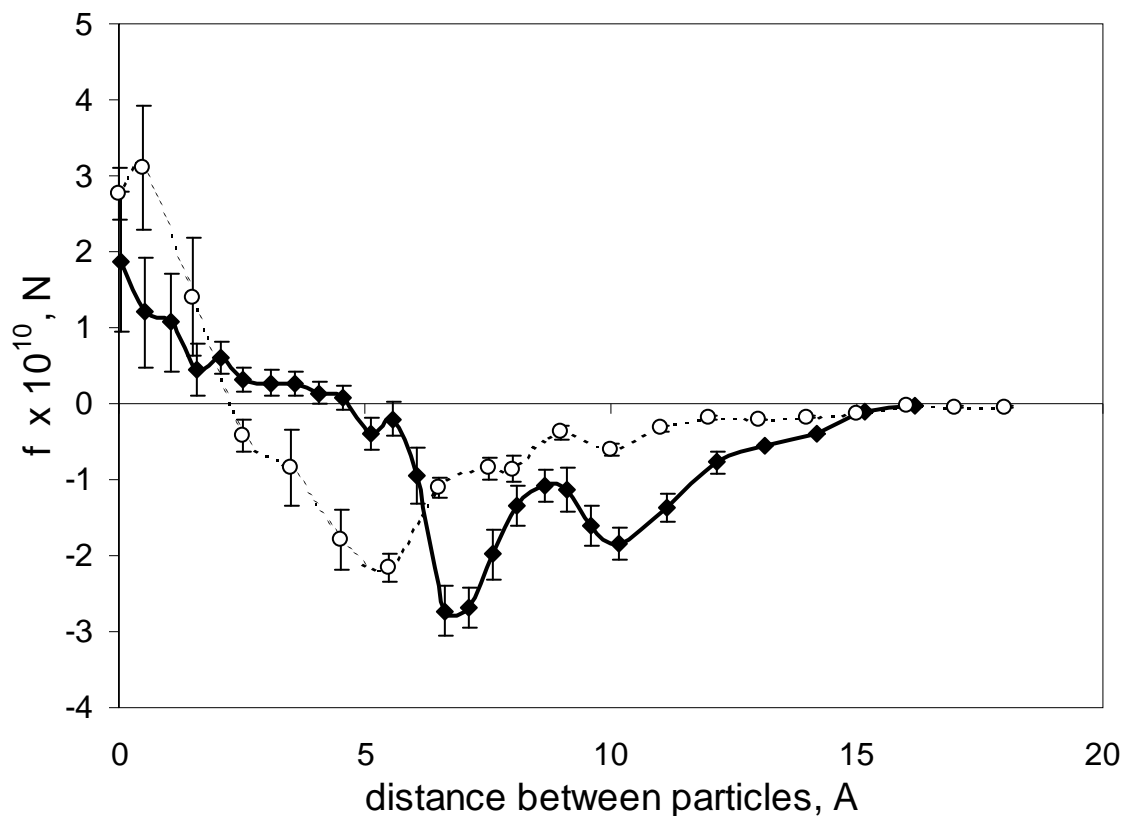
Figure 4.8 (b) Properties under subcritical conditions, T = 77.4K, p = 0.38p0. Solvation force as a function of nanoparticle separation. The solid line and dark points represent the simulation results obtained from spherical shell nanoparticle model, using GCMC method. The dotted line and blank circles represent the simulation results from FCC arranged LJ pseudoatom nanoparticle model, using MD method.

Thermodynamically the solvation force is related to the excess number of particles ΔN_{ex}. In the grand canonical ensemble, the solvation force f_s is equal to the derivative of the grand potential with respect to the distance:

$$f_s = -\left(\frac{\partial \Omega}{\partial d}\right)_{\mu VT} \tag{4.3}$$

where Ω is the grand potential, which can be obtained from the total isotherm $N(\mu)$:

$$\Omega(\mu^*,V,T) = -\int_{-\infty}^{\mu^*} N(\mu)d\mu = -\int_{-\infty}^{\mu^*}\{\rho_{bulk}V + \Delta N_{ex}(\mu)\}d\mu = \Omega_{bulk} - \int_{-\infty}^{\mu^*}\Delta N_{ex}(\mu)d\mu \tag{4.4}$$

Here, Ω_{bulk} is the grand potential of the bulk fluid in the same volume, which is independent of the interparticle separation d, and μ^* is a given value of the chemical potential. Therefore:

$$f_s(\mu^*) = -\int_{-\infty}^{\mu^*}\left(\frac{\Delta N_{ex}(\mu)}{\partial d}\right)_{VT}d\mu \tag{4.5}$$

This equation could have been used for the calculation of the solvation force, if we knew the entire sorption isotherm from $\mu = -\infty$ ($p_{bulk} = 0$) to our pressure of 69atm for any interparticle distance d. In this work we did not calculate the entire sorption isotherms; however, the comparison of the solvation force f_s and $\left(\frac{\partial \Delta N_{ex}}{\partial d}\right)$ may give us a useful insight on the behavior of f_s at lower pressures.

Table 4.2 Simulation results under subcritical and supercritical conditions.

fluid	CO$_2$					N$_2$	
fluid model	Dumbbell			LJ		LJ	
solid model	Spherical Shell				FCC	Sph. Shell	FCC
hydroxylation	high	medium	dehydroxyl	high	high	---	---
Conditions							
T, K	318					77.4	77.4
p, atm	69					0.38p_0	0.38p_0
Results							
d_{min}, Å	6.7	6.7	6.7	7.1	6.2	---	---
f_{min}, 10^{-10}N	-3.6	-2.2	-0.8	-3.7	-1.8	---	---
d_0, Å	27.7	27.6	19.7	18.3	29.6	---	---

In Figure 4.8 (a), we plotted the excess number of particles as a function of particle separation d at p_{bulk} = 69 atm. As seen in Eq. (4.5), we would expect that the more positive the slope of $\left(\dfrac{\partial \Delta N_{ex}}{\partial d}\right)$, the more negative the value of the solvation force.

From Figure 4.8a we can see that ΔN has a maximum at about 0.9nm, which means that $\left(\dfrac{\partial \Delta N_{ex}}{\partial d}\right) = 0$ at this distance; while f_s is negative in the entire range of interparticle distances d > 0.4nm. The discrepancy between the values of the distances d corresponding to zero solvation force and maximum of ΔN_{ex} makes us suggest that at low bulk pressures the maximum of ΔN_{ex} occurs at very small separations (d < 0.4nm), i.e. in the systems which can accommodate only one layer of molecules between the nanoparticles. A summary of results is listed in Table 4.2.

4.3.2   Under Supercritical Conditions

Next, we consider particle interactions at supercritical temperature. The density of the fluid at p_{bulk} = 69atm is about 0.16g/cm^3, which is much larger than the normal vapor densities but still substantially lower than the densities of liquid-like CO_2. In Figure 4.2 it shows that at 323K CO_2 is not far from the critical point and still has a visible gradual transition from "vapor-like" to "liquid-like" about p_{bulk} = 130atm. According to the Johnson equation, for the LJ model the difference in chemical potentials between p_{bulk} = 69atm (our conditions) and p = 130atm (effective "transition point" where the compressibility reaches a maximum) is -2.3 kJ/mol, which is far exceeded by the depth of the adsorption field. Therefore, we could expect relatively long-range density fluctuations in the fluid surrounding the nanoparticles and therefore the solvation force acting at

longer distances (in comparison with the subcritical system). A summary of results is listed in Table 4.2.

Figure 4.9 (a) shows ΔN_{ex} for all nanoparticle and fluid models considered at $T =$ 318K. Qualitatively, the supercritical systems show behaviors similar to those in the subcritical systems: ΔN_{ex} exhibits a maximum that gradually levels off at large particle separations. The isotherm $\Delta N_{ex}(h)$ depends strongly on the strength of the adsorption field, which accounts for the hydroxylation level. For dehydroxylated particles, the value for ΔN_{ex} obtained with the dumbbell model is nearly independent on the interparticle distance. Only at $d < 0.5$nm, ΔN_{ex} shows visible growth due to the increase of the available surface area because of particle separation. Then $\Delta N_{ex}(d)$ levels off, showing an almost constant value with a hardly visible maximum at 0.9nm. Correspondingly, the solvation force shows a minimum at 0.7-0.8nm and then approaches to zero, vanishing at a distance of approximately 2.0nm.

As the hydroxylation increases and the sorption field strengthens, the non-monotonous behavior of ΔN_{ex} becomes more pronounced, and the solvation force becomes more negative and long-ranged. This can be interpreted in terms of the formation of a liquid-like "junction". Although no distinct menisci could be identified in a supercritical fluid of this density, we could observe a visible densification of the fluid within the range considered. The maximum attraction force reaches a value of 3.6×10^{-10}N, and the attraction vanishes at, $d_0 = 3.5$nm, twice as much as the distance between two dehydroxylated particles.
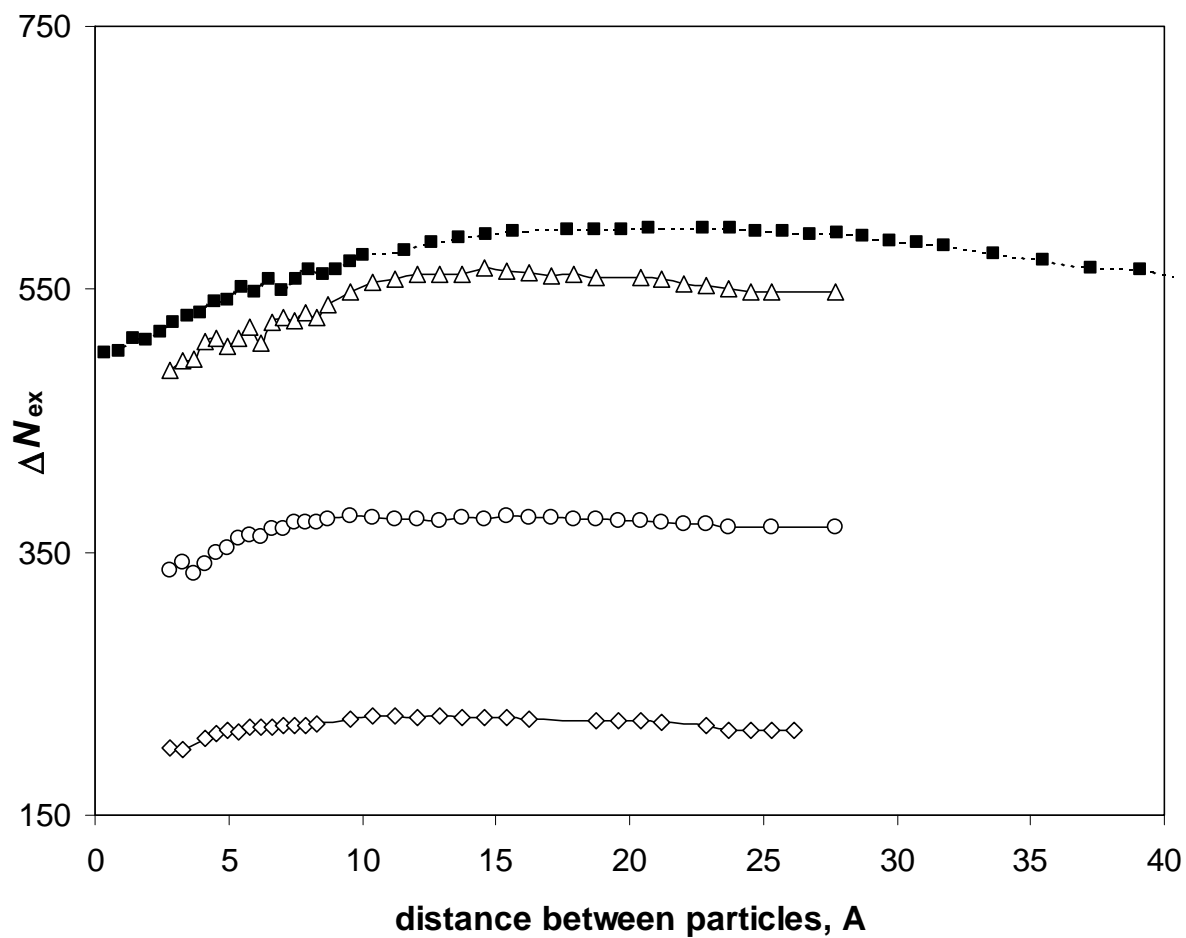
Figure 4.9 (a) Excess number of fluid particles as a function of nanoparticle separation under supercritical conditions, T = 318K, p = 130atm, using different fluid and solid models. LJ and dumbbell models are referred to the fluid model.
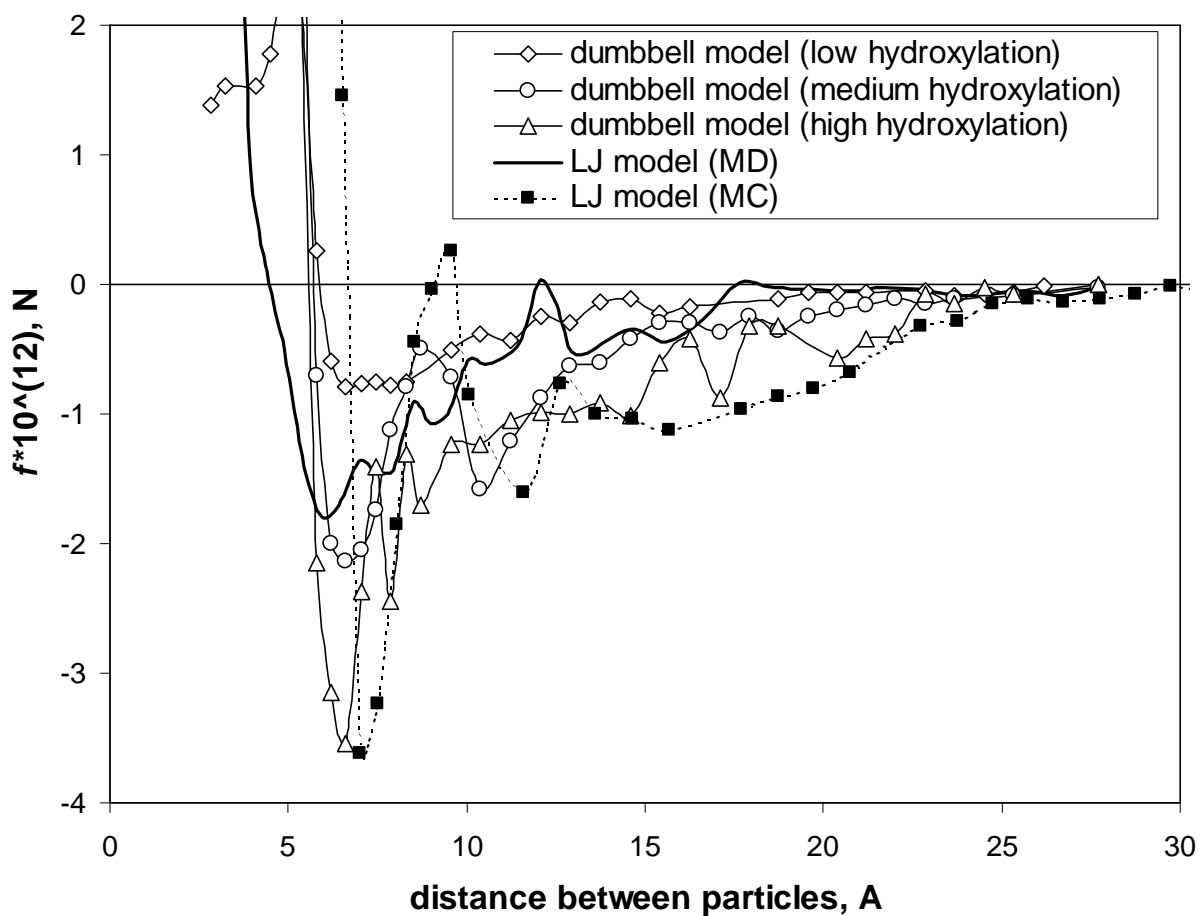
Figure 4.9 (b) Solvation force as a function of nanoparticle separation under supercritical conditions, T = 318K, p = 130atm, using different fluid and solid models. LJ and dumbbell models are referred to the fluid model.

Figure 4.9 (a) and (b) also show the dependence of the excess number of particles ΔN_{ex} and the solvation forces on the molecular model. The results for the dumbbell model at the highest level of hydroxylation and the LJ models were expected to agree well, since they represent the same target system. Our results, however, do not show that level of agreement, and even when the same nanoparticle model is used, ΔN_{ex} differs significantly. This difference can hardly be related to just the difference in monolayer capacity for the dumbbell and spherical models (indeed, the dumbbell model shows greater monolayer capacity [64]). Rather, we tend to believe that this discrepancy is due to the difference in fluid compressibility between the two models. The density change caused by the adsorption field is roughly equivalent to the shift in chemical potential. Larger compressibility $dN/d\mu$ leads to a larger density shift (outside the first monolayer, which is already liquid-like). From our GCMC simulations of bulk CO_2 it appears that the dumbbell model slightly overestimates the critical point. As a result, it underestimates the compressibility of CO_2 in the range $68 < p_{bulk} < 100$atm. This leads to lower ΔN_{ex} and shorter range for the attractive solvation force, which vanishes earlier for the dumbbell model than for the LJ model. However, the location and the depth of the first minimum of the solvation force agree well between the two fluid models. The difference in compressibility did not have any substantial effect on the reference isotherm at critical temperature (See Figure 4.3b) since a lower pressure was considered in Section II; the compressibility was well reproduced. Thus, we believe that the results obtained with the LJ model are more reliable since the LJ model describes more accurately the bulk equation of state at the given temperature and pressure range, despite the model simplicity.

Moreover, the comparison between the FCC and spherical shell models sheds light on the influence of the cutoff of the solid-fluid potential. The short-range cutoff undoubtedly reduced the attractive force, which vanished at distances as short as 18nm, compared to 25nm, showed by the spherical shell model.

The sorption of CO_2 at the particle surface and the resulting interparticle force can be expressed in terms of the formation and breakup of a fluid "junction" between the particles as the interparticle distance increases. That is, in general the situation is similar to that in a subcritical system. Therefore, the resulting solvation force is mostly negative (attractive) and its dependence on the interparticle distance shows a minimum. The important differences become evident by the long-range nature of density shift in the fluid created by the sorption field of the particles: the interparticle force becomes effectively long range and strongly depends on the strength of particle-fluid interaction, which increases with the level of hydroxylation. The attraction is strongest for the densely hydroxylated particles. Thus, we expect the RESS technique to be more efficient for solid materials and gases with weaker solid-fluid interactions. The thermodynamic comparison of the excess sorption isotherm and solvation force shows that the attraction extends to larger distances as the fluid pressure increases.

In this work, we examined the forces between a pair of nanoparticles. It is worth mentioning that the forces in an ensemble of nanoparticles in a molecular solvent cannot be successfully represented by pairwise potentials between the nanoparticles. That is, the forces in a cluster of three particles located in a close proximity of each other is not equal to the sum of forces between the pairs of the same particles considered separately, i.e. without the third one in close proximity. We suspect that not only three-particle, but even

four-particle effective interactions may become important in nanoparticle assemblies, and therefore our estimates would not be valid, for example, for deaggregation of a dense nanoparticle agglomerate. However, in relatively loose agglomerates with the estimated fractal dimension of 2.57 as considered in ref [85], three- and four- way contacts become relatively rare, and the deagglomeration is still controlled by the forces between individual nanoparticles considered in the present work.

4.4   Deagglomeration of Nanoparticles

Here we focus on exploring the shearing forces necessary to break silica agglomerates in supercritical carbon dioxide. This is very costly computationally, so we considered small agglomerates of the order of 8-10 nm under the effect of shearing forces. In general, agglomerate breakup may occur by two modes: collisional mechanical breakup and turbulent fluid mechanical breakup. In this present work, our goal is to develop a fundamental understanding of the second one, using a fluid shearing flow for the breakage of nanoparticle agglomerate. The research tasks include characterization of the degree of deagglomeration as a result of applying shearing forces of different magnitude along with the development of a fundamental understanding of the strength and breakup of the agglomerates of nanoparticles through molecular dynamics modeling.

4.4.1   Simulation Setup and Visualization

In this part of work, we use the LJ model for CO_2 and the FCC model for silica nanoparticle. In a box of $55 \times 40 \times 40 \, \sigma_{ff}^3$, 27 nanoparticles aggregate and form a cluster after 10ps of equilibration, having a diameter of approximately 10 nm. We choose a

longer dimension in the x-direction, in which the shearing forces are applied. Typical simulation includes 30,104 CO_2 molecules, giving a density of 0.6 g/cm^3. The constant number of particles (N), volume (V) and temperature (T) MD technique is applied. The LJ potential was truncated at the cutoff distance of $2.5\sigma_{ff}$ (same as the fluid-fluid potential). The temperature of the system is adjusted to its value of 318 K (this temperature is slightly above the critical point 304K). External forces of opposite directions are applied onto the top and bottom of agglomerate to create the shearing motion (Figure 4.10).
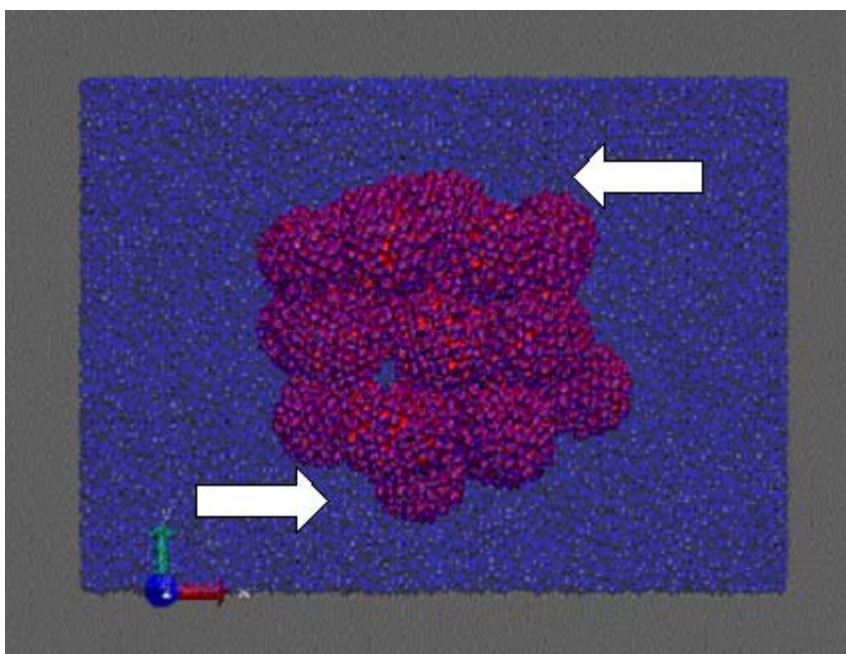
Figure 4.10 External forces of opposite directions are applied onto the top and bottom of agglomerate.

First we examined the strength of the external forces. Two values were considered: 4.28×10^{-8} N (strong), and 1.07×10^{-8} N (weak). They are in the same order of magnitude, for both cases, the agglomerate breakup after applying the shearing forces. Simulation snapshots of the silica nano-agglomerate and after applying forces broken pieces are shown in Figure 4.11. We can clearly see that at the beginning, the nanoparticles do not deform and they remain spherical throughout. When applying the forces, the nanoparticles start to merge, forming an agglomerate. Then the agglomerate breaks into two pieces, with the upper and lower parts moving in the opposite directions. When the system is under strong shearing forces, the agglomerate starts to break apart after 0.1 ns. For the case of applying relative weak shearing forces, the agglomerate also experience the same process of deformation followed by elongation, and finally breaks-up, but it happens at a later time.

(a)

(b)

(c)

(d)

(e)

(f)
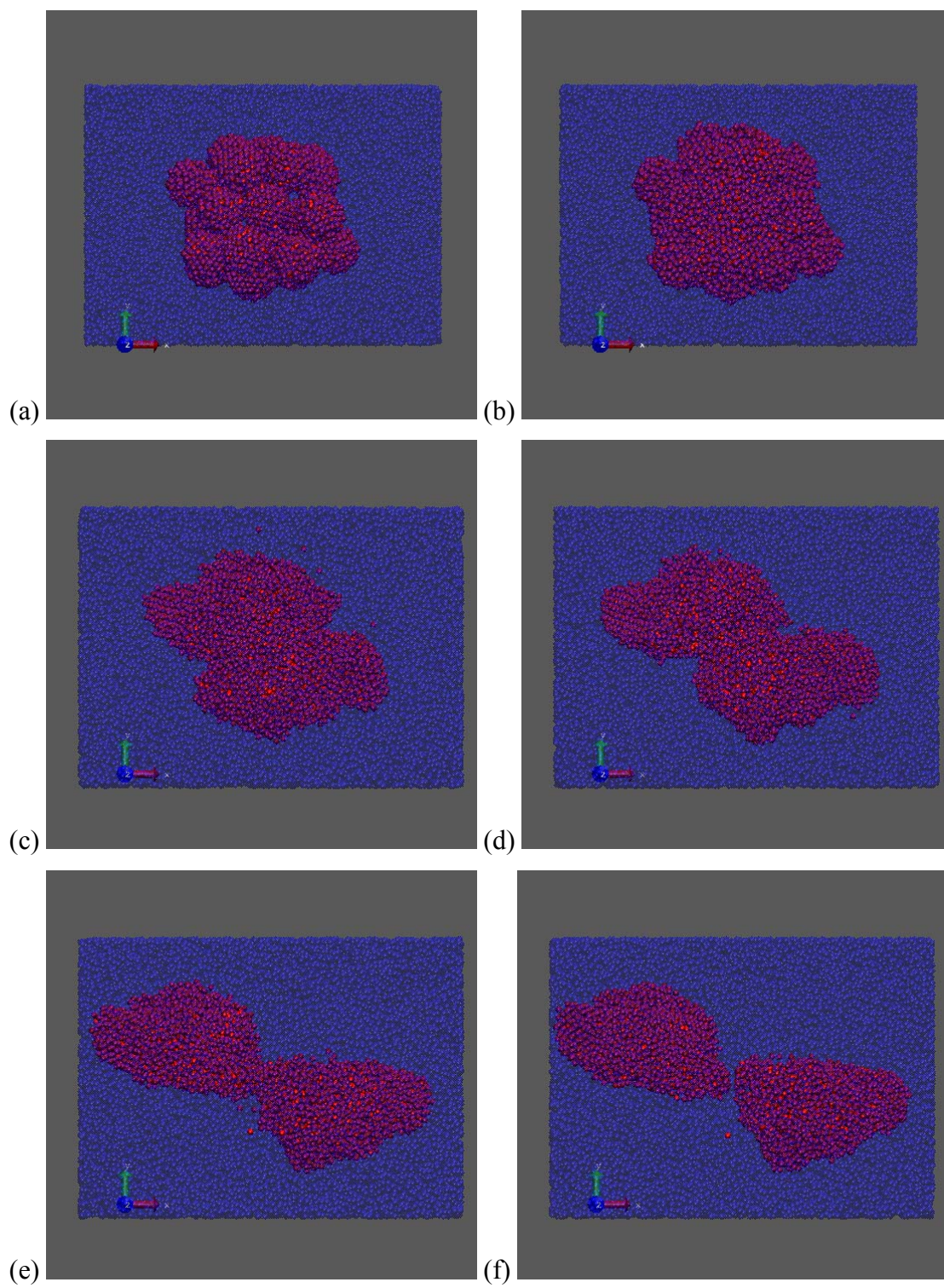
Figure 4.11 Simulation snapshots of the agglomerate deformation and breakage under the stronger forces: (a) t=0 (b) t=0.08ns (c) t=0.10ns (d) t=0.11ns (e) t=0.12ns (f) t=0.15ns.

4.4.2   Quantify the Breakage

Besides visualization, the agglomerate breakage can also be quantitatively measured by a histogram, which is obtained by counting the total numbers of silica units along the axis. At the breakup point, the density profile shows a big discontinuity in the x-direction (Figure 4.12). A group at Princeton also studied this process theoretically, and obtained that the flow of the supercritical fluid inside the nozzle in the RESS device generates shear forces of the same order. We could quantitatively confirm that deagglomeration occurs under the influence of those values of the shear force.
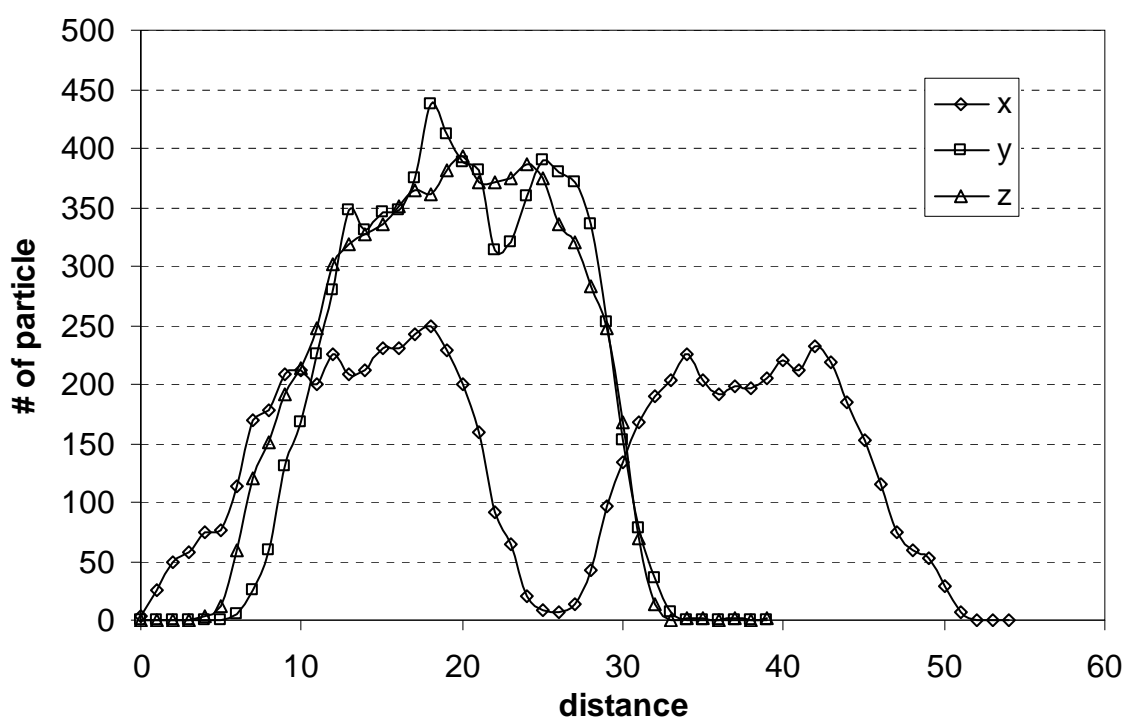
Figure 4.12 Histogram of agglomerate as a function of distance at the breakup point.

In order to understand the effect of agglomerate size, we performed similar simulations of smaller agglomerate under shearing forces. In this case, the agglomerate is composed of 18 nanoparticles, giving a diameter of approximately 7 nm. While applying the shearing forces of the same order of magnitude as previously for the large agglomerate, the small agglomerate experiences elongation, but no breakage. Then the shearing forces are increased to one order of magnitude larger, and the agglomerate was ruptured (Figure 4.13). This can be confirmed by the Rumpf theory, stating that the maximum tensile strength is inversely proportional to the diameter of the granular particle. We expect to develop a force model balance in the nanometer scale, and to correlate the agglomerate size with the shearing force needed to break the agglomerate.
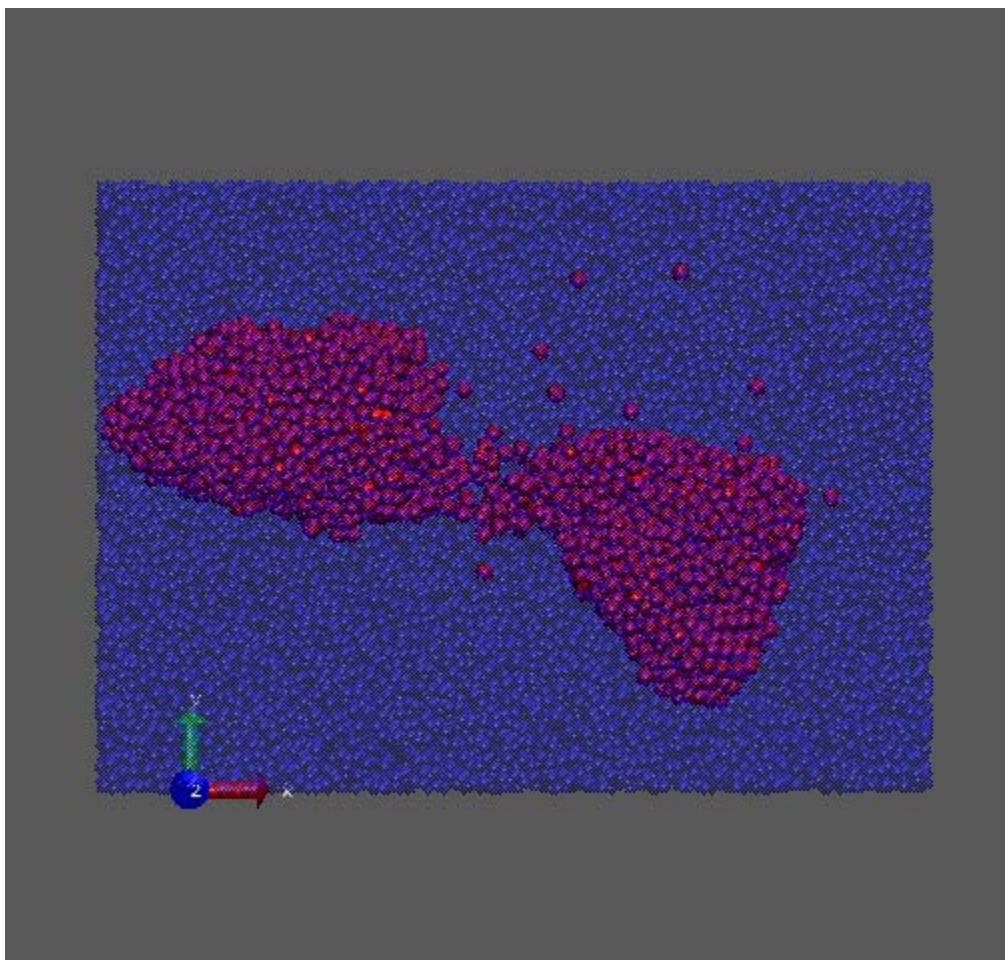
Figure 4.13 Final simulation snapshot of the small agglomerate breakage.

4.4.3   Diffusion of the Fluid

The mean square displacement (MSD) of atoms in a simulation can be easily

computed by its definition: $MSD = \left\langle \left| \vec{r}(t) - \vec{r}(0) \right|^2 \right\rangle$ (4.6)

where $\langle \ \rangle$ denotes here temporal averaging over all the atoms (or all the atoms in a given

subclass) and $\vec{r}$ is the molecular position. Care must be taken to avoid considering the

"jumps" of particles to refold them into the box when using periodic boundary

conditions. The MSD contains information on the atomic diffusivity. Figure 4.14 shows

the mean square displacement of fluid particles as a function of time. As we can see, the

fluid diffusion increases extremely after agglomerate breakage, especially in the x-

direction, where the shear is applied.
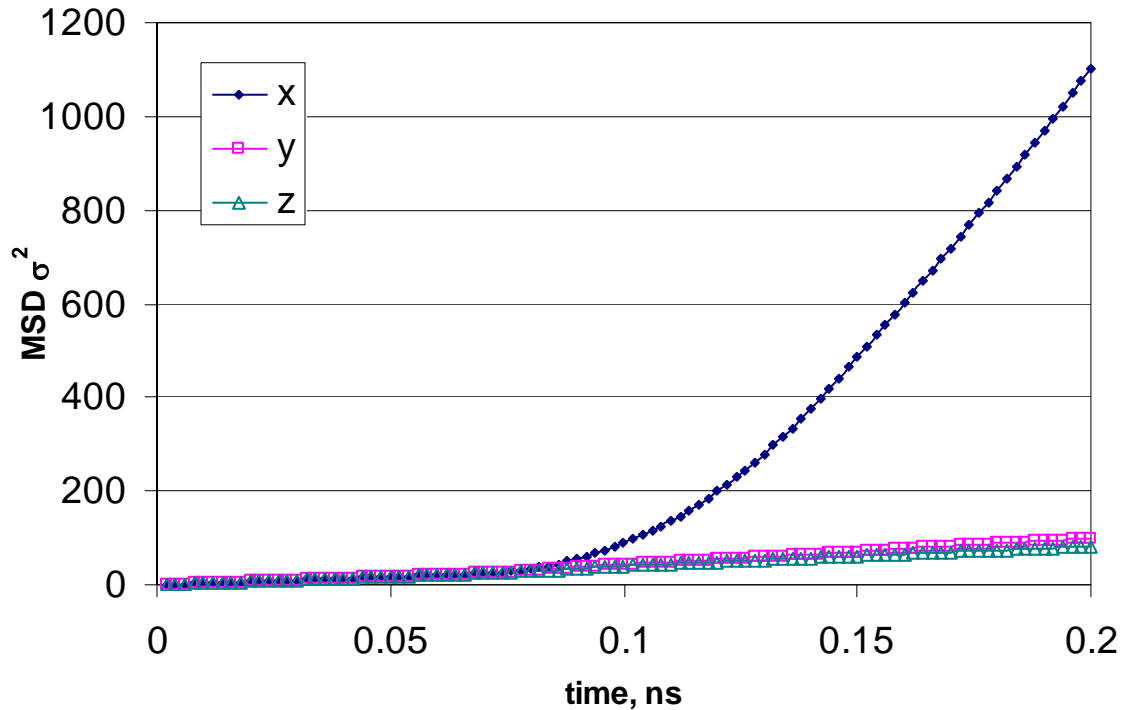
Figure 4.14 The x, y, and z components of fluid mean square displacement as a function

of time.

For our system, MSD grows linearly with time. In this case it is useful to characterize the system behavior in terms of the slope, which is the diffusion coefficient D from Einstein relation:

$$D = \lim_{t \to \infty} \frac{1}{6t} \left\langle |\vec{r}(t) - \vec{r}(0)|^2 \right\rangle \qquad (4.7)$$

The diffusion coefficient can be calculated from the slope of the curve: $D = \frac{1}{2d} \times \frac{\partial r^2(t)}{\partial t}$. In both y and z directions, the MSD increases monotonically with time, giving a constant diffusion coefficient:

$$D = \frac{1}{2 \times 3} \times 424.61 \frac{\sigma^2}{ns} = \frac{1}{2 \times 3} \times 424.61 \times \frac{(3.68 \times 10^{-8} \, cm)^2}{10^{-9} \, s} = 9.58 \times 10^{-5} \, cm^2/s$$

It is reported in many experimental and computational studies [86] that the self diffusion coefficient of CO_2 is in the magnitude of 10^{-4} cm^2/s, ranging from 1.2 to 1.4×10^{-4} cm^2/s. Our calculated value of CO_2 self diffusion coefficient is expected to be smaller than the experimental value, because the nanoparticle agglomerate hinders the fluid movement. When the agglomerate starts to elongate, the fluid diffusion is accelerated almost 2 times faster. We also expect to see a more free fluid motion when the agglomerate is completely stretched apart, and the slope of the curve can be good indicator for the breakage of the agglomerate.

4.5   Summary

In this chapter we report molecular simulation studies on the interaction forces between silica nanoparticles in supercritical carbon dioxide at 318K. We have explored the interactions of silica nanoparticles in supercritical CO_2. Through a comprehensive

analysis of the available experimental data on CO_2 sorption at siliceous surfaces we examined the solid-fluid interactions and fitted the parameters of solid-fluid potentials. We have applied external shearing forces at the top and bottom of the agglomerate. The agglomerate experiences a process of deformation followed by elongation, and break-up. The particle distribution histogram shows a discontinuity at the break point. For smaller agglomerates, larger shearing forces have to be applied. Our calculated value of CO_2 self diffusion coefficient is expected to be smaller than the experimental value, because the nanoparticle agglomerate hinders the fluid movement. In the direction of the shearing forces, the diffusion of CO_2 shows a steep increase as the agglomerate breaks, confirming the rupture of the agglomerate. It can be suggested that simulating the behavior of one single agglomerate can be quite representative of the whole deagglomeration process as long as the interactions between primary agglomerates are not overwhelming.

Chapter 5

RHEOLOGICAL PROPERTIES OF POLYMER NANOPARTICLE

COMPOSITES

Chapter 2 explains the molecular model built for the system of silica nanoparticles embedded in polyethylene melt, and Chapter 3 investigates the dispersion of nanoparticles in a polymer matrix. In this chapter, we focus on studying the rheological properties of polymer nanoparticle composites.

In what follows, Section 5.1 introduces and reviews the simulations of simple shear (or Couette) flow. Instead of applying the Lees-Edwards boundary conditions, we employ a different method for generating shear. In Section 5.2, we validate our coarse-grained model for polyethylene and compare the calculated structural and dynamic properties with current experimental data and theories. Section 5.3 focuses on studying the mechanisms governing the linear viscoelastic behavior of the composites, with spherical nanofillers dispersed in polymer melt matrices.

5.1 Introduction to Simple Shear Flow

Simple shear is defined as an idealized treatment of a fluid between two large parallel plates (to permit ignoring edge effects) of area A, separated by a distance h. If one plate moves relative to the other with a constant velocity V, requiring a force F acting in the direction of movement, and the density, pressure, and viscosity throughout the fluid are constant, the Newtonian equation can be coupled with the equations of motion and continuity to show that the velocity gradient in the fluid is constant. This idealized case

(simple shear) is usually used to define shear viscosity. Thus simple shear flow may be expressed as $v_x = G \cdot z$ and $v_y = v_z = 0$ where the flow in the x-direction changes in magnitude along the z-direction, and G is a scaling parameter. Simple shear flow often occurs in many industrial processes, and regularly serves as the characteristic flow by which the interaction coefficient is based upon [87].

A Newtonian fluid is one in which the viscosity is independent of the shear rate. In other words a plot of shear stress versus shear strain rate is linear with slope η. In Newtonian fluids all the energy goes into molecules sliding. In non-Newtonian fluids, the shear stress/strain rate relation is not linear. Typically the viscosity drops at high shear rates — a phenomenon known as shear thinning. A schematic plot of shear force vs. shear rate for typical Newtonian and non-Newtonian fluids is given in Figure 5.1.
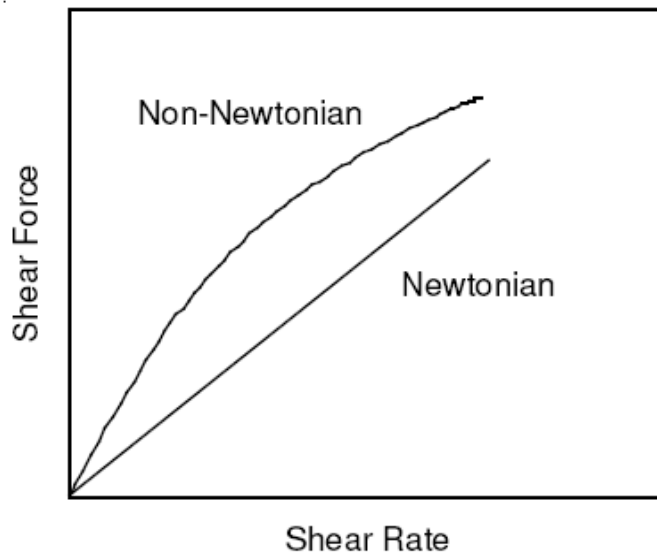
Figure 5.1 Schematic plots of shear force vs. shear rate for Newtonian and non-Newtonian fluids.

In molecular dynamics, the standard way to model shear flow is by applying the Lees-Edwards boundary condition [26]. Here in this work, we shear the liquid by moving the solid wall past the liquid. The positions and velocities of the fluid particles are updated using the Verlet or a similar algorithm. The walls are assumed to be made up of "virtual" particles, and the positions and velocities of them are not updated using the Verlet algorithm. The interactions between the fluid particles and wall particles are determined by Equation 2.2 but are more repulsive than the fluid-fluid interaction. In our simulations, the upper wall is given a velocity in the x-direction and the lower one is given a velocity of the same magnitude, but in the opposite direction. The periodic boundary conditions are enforced in other directions. These movements of the imaginary walls create the drag forces that act on the fluid particles, and a velocity gradient in the fluid between the plates, which can be used to obtain the shear rate.

Figure 5.2 presents the flow velocity profiles from the center point to one side of the walls at different wall moving speeds, showing the velocity of fluid in x-direction as a function of z. The velocity increases linearly with increasing the z-distance from the center. The shear rate can be given by the velocity gradient dv_x/dz of the linear part in Figure 5.2. The calculated results are listed in Table 5.1. The velocity gradient increases with the increasing wall moving speeds. From now on, we refer these cases in terms of shear rate, instead of wall velocity.
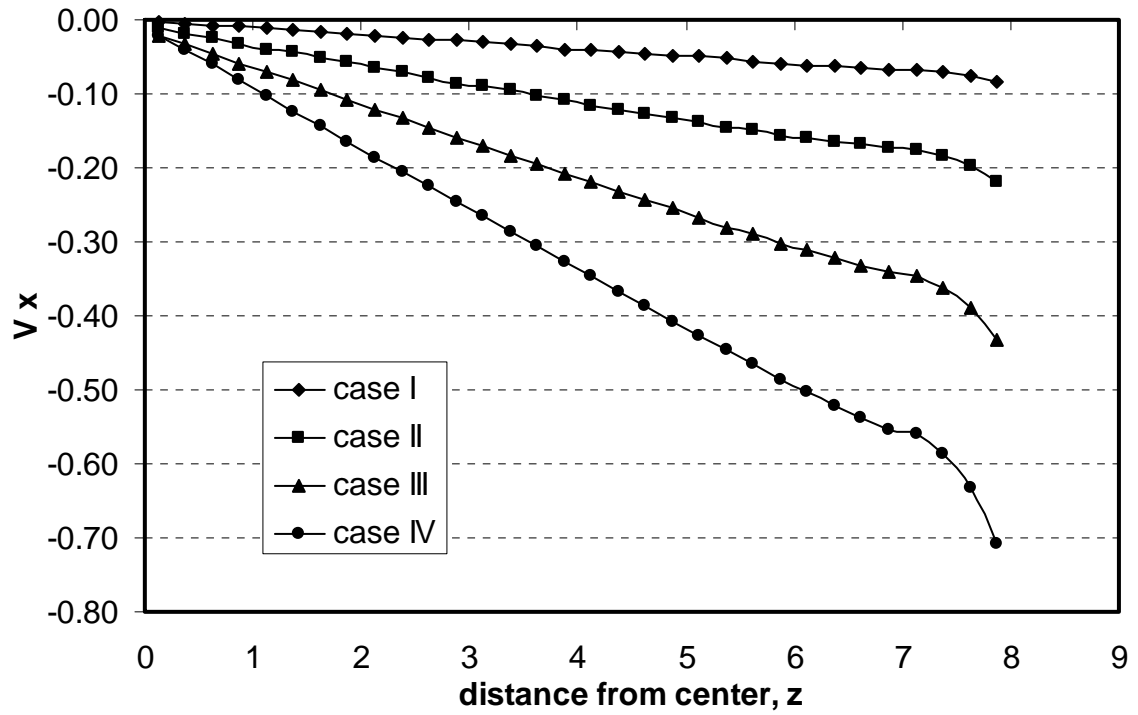
Figure 5.2 Velocity profiles of different cases. The shear rates are in the unit of 10^{14} s^{-1}.

Table 5.1 Calculated shear rates of different cases. The wall velocities and shear rates are in units of 10^5 m/s and 10^{14} s^{-1} respectively.

Case #	I	II	III	IV
Wall velocity σ/t_0	0.2	0.5	1.0	1.7
Shear rate $\gamma = dv_x/dz$	0.0098	0.0244	0.0484	0.083

5.2 Polyethylene Under Shear

Several interesting phenomena exhibited in polymeric liquids in flows are typically due to the non-Newtonian nature of the macromolecular fluid. For example, the viscosity of polymer solutions and melts in shear flows undergo a decrease with increase in shear rate. This shear-thinning behavior is observed in most polymer solutions that have a shear rate dependent viscosity, although there are a few polymer solutions that are dilatant (i.e. that exhibits shear-thickening). The normal stresses are also non-zero and shear rate dependent. There are many experimental investigations of shear thinning [88, 89]. Recent work by Micic and Bhattacharya on the rheology of various polyethylene and their blends used a Rosand Precision Twin Bore Instrumented Rheometer to measure the shear viscosity [90].

Several simulation methods can be used to study polymer melts and solutions under shear. Examples of the use of equilibrium molecular dynamics simulations for polymeric liquids include the work of Paul et al. [91, 92] and Harmandaris et al. [93, 94]. In both of these works, dynamical properties of chain molecules are compared to the predictions of the Rouse model. Moreover Paul et al. [92] found quantitative agreement between simulation and experiment for the dynamic structure factor of C_{100} after correcting for a 20% difference in the self-diffusion coefficient. Shear thinning of chain molecules in molecular simulations was observed for the first time by Morriss et al. (1991). Kremer and Grest [95] have performed simulations at equilibrium with a Brownian dynamics algorithm with many aspects similar to deterministic equilibrium MD. Using a non-equilibrium molecular dynamics algorithm developed by Edberg et al. (1986) they simulated planar Couette flow of decane and eicosane. At a single strain rate

expected to fall within the Newtonian regime, Mondello and coworkers [96] used NEMD to calculate the viscosity of $C_{66}H_{134}$ and found excellent agreement with predictions of the Newtonian viscosity based on a combination of equilibrium properties and the Rouse model.

In this work, the rheological properties of polyethylene are first studied in order to validate the coarse-grained model. Several static and dynamic properties are carried out, such as the end-to-end distance and the shear viscosity of the linear polymer melts. Rouse scaling behavior is reproduced for monodispersed polymeric systems with different chain lengths. Equilibrium molecular dynamics is used in these cases where information about the time dependent dynamics, rather than just the configuration, is desired.

The simulation data under planar Couette flow (PCF) were obtained by performing constant particle number, volume, and temperature (NVT) simulations using the Verlet algorithm incorporating the Nosé-Hoover thermostat. The coarse-grained model was used to describe polyethylene. This model does an excellent job of describing the thermophysical properties of liquid and gaseous n-alkanes under quiescent conditions. Chain lengths investigated vary from 8 to 20-beads per chain. The simulations are performed in a parallelepiped box with periodic boundary conditions applied in the x and y directions; in the z direction the fluid is confined by two imaginary walls. The reduced cell dimensions are $L_z = 16 r_c$, and $L_x = L_y = 30 r_c$. The total number of particles in the box is fixed at 57600, which gives an overall reduced density, $\rho r_c^3 = 4.0$. The total density is not affected by the chain length.

5.2.1   Density Profile and Bond Length Distribution

The number density of polymer beads is plotted from the center point of simulation box, along the z-direction for different shear rates (Figure 5.3). All the profiles nearly overlap with each other. At distances far away from the boundary, a constant density profile confirms that the fluid is spatially homogeneous. Small fluctuations happen at the vicinity of the boundary, indicating the layered structure of the fluid particles at that point. This is an edge effect due to packing of the particles at the boundary.
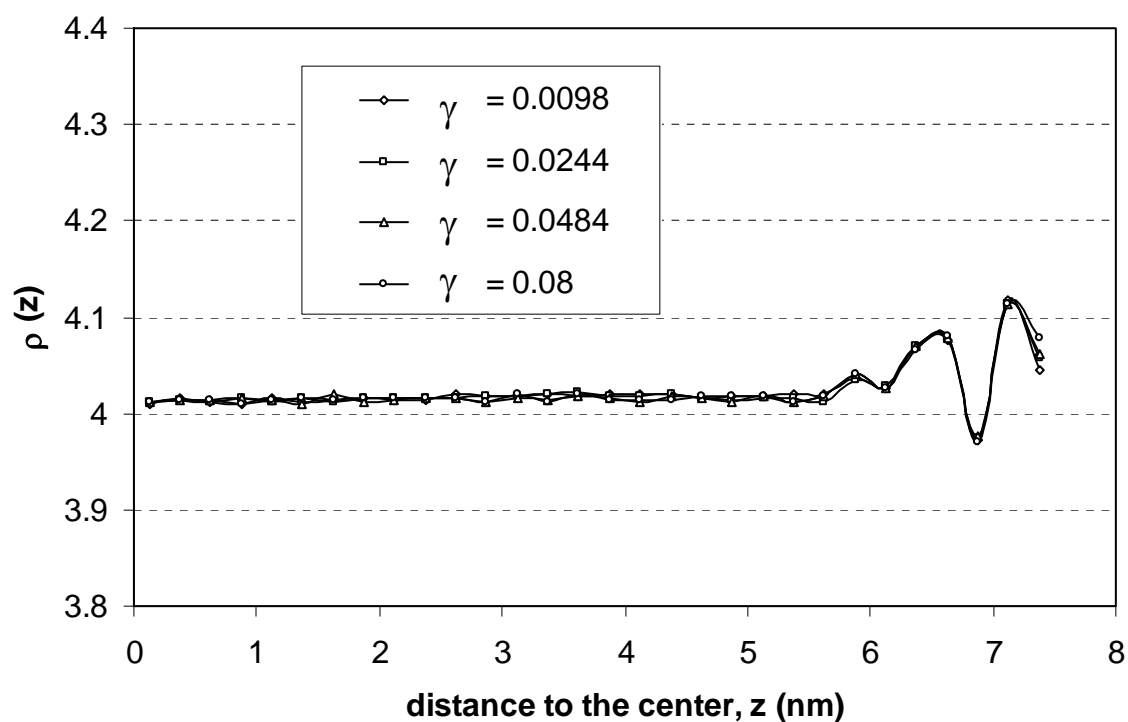
Figure 5.3 Number density profiles for polymer chain of L=8 at different shear rates (in units of 10^{14} s^{-1}).

For polymers in equilibrium, Equation 2.2 gives an approximately symmetric bond length distribution with a maximum at approximately 0.95rc. In Figure 5.4 the coarse-grained bond length distribution for polymer chains with no shearing is illustrated by the solid line. The same graph also depicts the bond length distributions of polymer chains under different shear rates. All the histograms are normalized. In the presence of a shear field, the intramolecular and intermolecular configurations change from the equilibrium state in order to minimize the free energy in the presence of the external field. After 2ns, we observe a bimodal distribution of bond length, with two maximum, one at 0.95nm and the other at 1.35nm, indicating that some chains are being stretched. This can be explained by the strong repulsive force from the walls to polymer chains. Regardless of the value of the velocity at which the walls are moving, we observe that the distribution of bond lengths is similar after 2ns. The final distribution shows a given percent of "elongated" bond lengths at 1.35nm and also a percent of "equilibrium" lengths at 0.95nm, i.e. some of the polymer bonds remain at their equilibrium length. There is no significant difference between different shear rates.
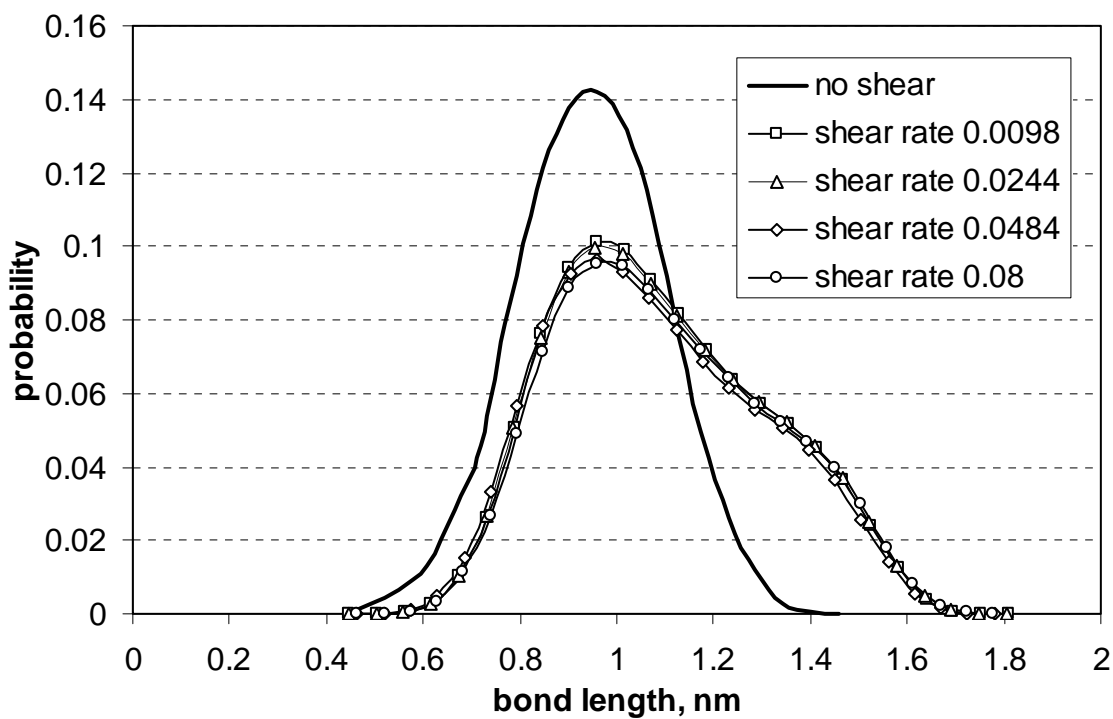
Figure 5.4 Polymer bond length distributions under zero and different shear rates (in units of 10^{14} s^{-1}).

5.2.2   Chain Dimension and Diffusivity

Several equilibrium properties are of interest as well, including the average chain dimension and the self-diffusion coefficient. They are important because they help us gauge the agreement between properties predicted by the potential model and corresponding properties measured by experiment.

In order to examine the variation of chain dimensions under shear, we calculate the mean squared radius of gyration. In polymer physics, the radius of gyration is used to describe the dimensions of a polymer chain. For a particular molecule at a given time it is defined as: $R_g^2 = \frac{1}{L} \sum_{k=1}^{L} (r_k - r_{mean})^2$, where r_{mean} is the mean position of the monomers. The radius of gyration is also proportional to the root mean square distance between the monomers: $R_g^2 = \frac{1}{2L^2} \sum_{i,j} (r_i - r_j)^2$. Here r_i and r_j are the location of two consecutive CG beads. L is the polymer chain length. And the end-to-end distance is defined as $R_{ee}^2 = \langle (r_1 - r_e)^2 \rangle$, where r_1 and r_e are the positions of the first and last beads.

Based on averages accumulated during the course of simulation, we measured for our system the values of R_g^2 and R_{ee}^2. Table 5.2 summarizes the results for polymer chain (L=8) at zero and different wall velocities. The ratio is close to Gaussian-chain behavior having the relation $R_{ee}^2 / R_g^2 = 6$. This behavior has been observed previously for a C100 melt [91] as well as melts of shorter alkanes [96-98]. Based on these results we conclude that the coarse-grained representation of the system preserves static properties. In a shear flow, polymer chains near the surface are forced to migrate in the shear direction, and are

stretched. The ratio increases with the increasing of wall velocity, because of the chain extension.

Table 5.2 Comparison of chain dimensions: radius of gyration (R_g^2) and end-to-end distance (R_{ee}^2) at zero and different shear rates (in units of 10^{14} s^{-1}).

	$\dot{\gamma} = 0.0$	$\dot{\gamma} = 0.0098$	$\dot{\gamma} = 0.0244$	$\dot{\gamma} = 0.0484$	$\dot{\gamma} = 0.08$
R_g^2 (Å^2)	10.9	11.0	11.0	11.2	11.4
R_{ee}^2 (Å^2)	65.7	67.9	68.1	69.8	72.6
Ratio	6.03	6.17	6.19	6.23	6.37

The end-to-end distance of polymer chains is an important structural property of polymer materials. Figure 5.5 gives the end-to-end distance as a function of shear rate for three different polymer chain lengths. They all increase with increasing shear rate, which illustrates that the polymer chains stretch to a certain extent under shear flow. The stretch ability also increases with increasing chain length.
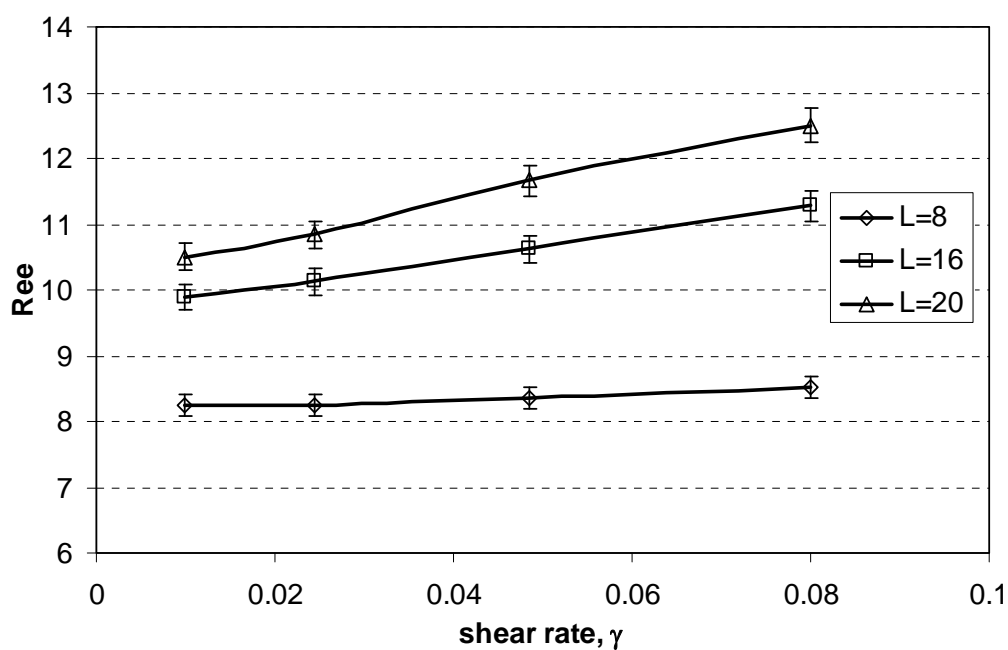
Figure 5.5 End-to-end distances as a function of shear rate for different polymer chain lengths.

Molecular simulation calculations of self-diffusion coefficients under equilibrium conditions are usually performed either in terms of mean squared displacements (MSD) and the Einstein relation or velocity autocorrelation functions and the Green–Kubo relation. When the former method is employed for chain systems, the self-diffusion coefficient is calculated in terms of the limiting slope of the mean squared displacement (MSD) of the chain centers of mass as a function of time based on the Einstein relation $MSD(t) = 6Dt$. Now we first define the MSD of the center-of-mass R^{cm} of a chain:

$MSD(t) = \left\langle \left[R^{cm}(t) - R^{cm}(0) \right]^2 \right\rangle$. Figure 5.6 gives the total and the three components of MSD of polymer chain center of mass. The diffusion in the direction perpendicular to the surface is small and liquid-like, as one would expect for a confined fluid between walls. The diffusion along the shearing direction is significantly greater for the polymer. A real chain however will be severely hindered by the interactions with surrounding chains, leading to subdiffusive behavior.
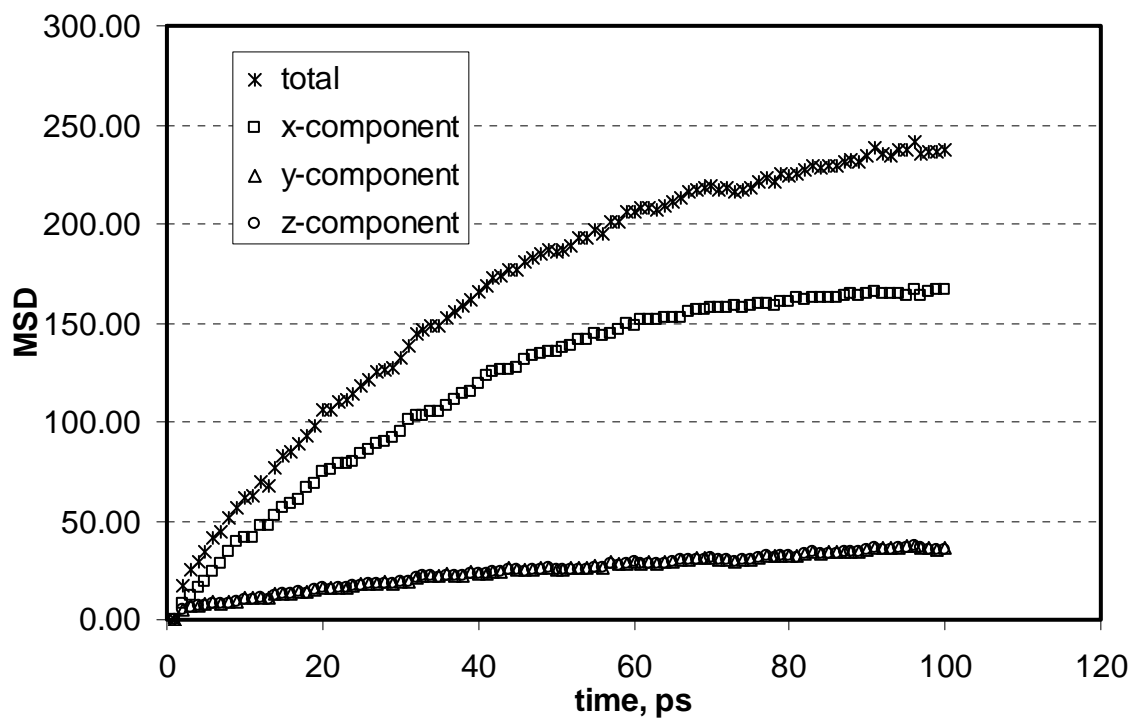
Figure 5.6 Components of the mean square displacement of polymer chain center of mass as a function of time for polymer chains of L = 8.

5.2.3 Shear Stress and Viscosity

In the literature several viscometric functions are commonly used to characterize the rheology of fluids, such as shear stress, viscosity and first normal stress. For a homogeneous equilibrium atomic system the stress tensor is calculated using the Irving-Kirkwood (IK) method: $\tau_{zx} = -\frac{1}{V}\left\langle \sum_{i}^{N_p} m_i v_{iz} v_{ix} + \sum_{i}^{N_p}\sum_{j>i}^{N_p} r_{ijz} F_{ijx} \right\rangle$, where V is the volume of the system, r_{ij} is the minimum image vector between atoms i and j, and F_{ij} is the force between the same two atoms, where m_i is the particle mass, Np the number of particle, $u_{i\alpha}$ and $u_{i\beta}$ the peculiar velocity components of particle i, for example, $u_{i\alpha} = v_{i\alpha} - \bar{v}(\vec{x})$, with $\bar{v}(\vec{x})$ being the stream velocity at position $\bar{x}$, and $\langle ... \rangle$ denotes the ensemble average. $F_{ij\beta}$ is the β–component of the force exerted on particle i by particle j. The first sum in the right-hand side of the above equation denotes the contribution to the stress from the momentum transfer of particles. The second sum represents the contribution from the interparticle forces. In the simulations, the expression given for the stress tensor is averaged over 1000 time steps.

In order to test the accuracy of the coding of the IK equation, we performed an additional calculation of the shear stress, which is directly defined by F/A. F is the summation of x component of the drag force, which is applied to the fluid particles during the simulations. A is the area where the shear is applied. Table 5.3 shows the comparison of the two different methods and it can be seen that there is excellent agreement between them. Thus, we confirmed that the values obtained from the Irving-Kirkwood equation do indeed correspond to the shear force.

Table 5.3 Shear stresses computed from Equations $\tau_{zx} = -\dfrac{1}{V}\left\langle \sum_{i}^{N_p} m_i v_{iz} v_{ix} + \sum_{i}^{N_p}\sum_{j>i}^{N_p} r_{ijz} F_{ijx} \right\rangle$

(IK method) and $\tau = F/A$ for polymer chains of L=8.

$\gamma \times 10^{-12}$, s^{-1}	0.98	2.44	4.84	8.0
IK, $\tau \times 10^{-12}$, Pa	1.53	2.14	2.70	3.25
F/A, $\tau \times 10^{-12}$, Pa	1.57	2.17	2.75	3.28

There are two different approaches to calculate the viscosity by molecular dynamics simulations: either by the time correlation function theory employing the Green-Kubo integral formulas or Einstein relations in equilibrium simulations, or by nonequilibrium molecular dynamics. The shear-rate dependent viscosity is determined from the constitutive relation: $\eta = \dfrac{\tau_{zx}}{\dot{\gamma}}$. The viscosity of the liquid is the ratio of the applied shear stress to the resulting strain rate (or equivalently, the ratio of the shear stress required to move the solution at a fixed strain rate to that strain rate). $\gamma = \dfrac{dv_x}{dz}$, where vx is velocity in the x direction. The relations between viscosity (η), shear stress (τ), and shear rate (γ) are $\tau = \eta \cdot \gamma$.

In Figure 5.7 shear viscosity is plotted versus shear rate for different polymer chain lengths. The shear viscosity exhibits expected shear thinning with increased strain rate over the entire range. The average power law exponents are calculated as −0.65 for shorter chains and −0.4 for longer chains. For polymeric liquids, power law exponents are generally reported in the range −0.4 to −0.9 [99]. The lower Newtonian regime was not reached because the examined shear rates were still not low enough. The error bar,

estimated from the scatter during the course of the simulation, is likely to be an underestimate of the true uncertainty in the simulation for such a relatively short run and at low strain rate.
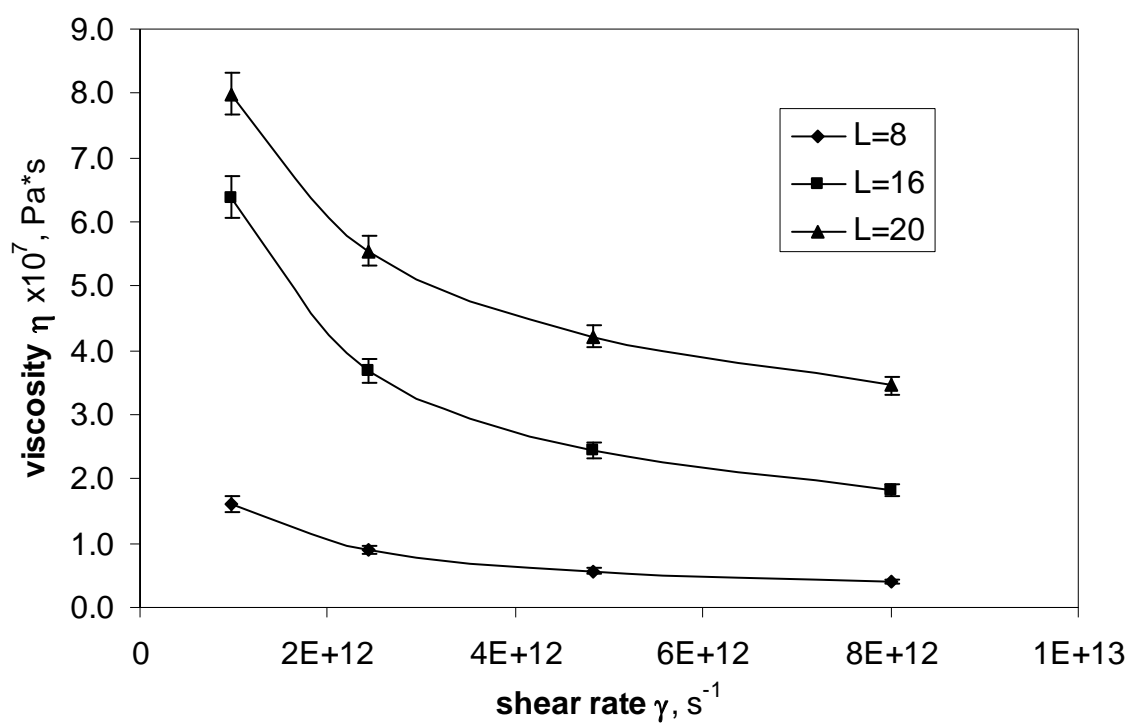
Figure 5.7 Shear viscosity vs. shear rate for different polymer chain lengths.

5.2.4   <u>First and Second Normal Stress Difference</u>

Far from equilibrium and in particular for polymeric liquids under PCF the diagonal components of the stress tensor become unequal, leading to normal stresses. In these situations the first and second normal stress coefficients are reintroduced here: $\Psi_1 = \dfrac{\tau_{xx}}{\dot{\gamma}^2}$ and $\Psi_2 = \dfrac{\tau_{yy}}{\dot{\gamma}^2}$. These functions measure the difference between stresses normal to the faces of a cubic volume of fluid. Data for the steady state first ($\Psi1$) and second ($\Psi2$) normal stress coefficients under planar Couette flow are presented in Figure 5.8. It had been suggested in the Weissenberg Hypothesis [100] that the second normal stress in fluids is zero, however it is now known that the $\Psi2$ is about 10% of the value of $\Psi1$. From the simulation data it is seen that both functions decrease in value as the strain rate is increased. In general these functions show an increase with molecular length, which is comparable with viscosity. However in comparison with the shear viscosity, the range of $\Psi1$ is about an order of magnitude greater, particularly for longer molecules.
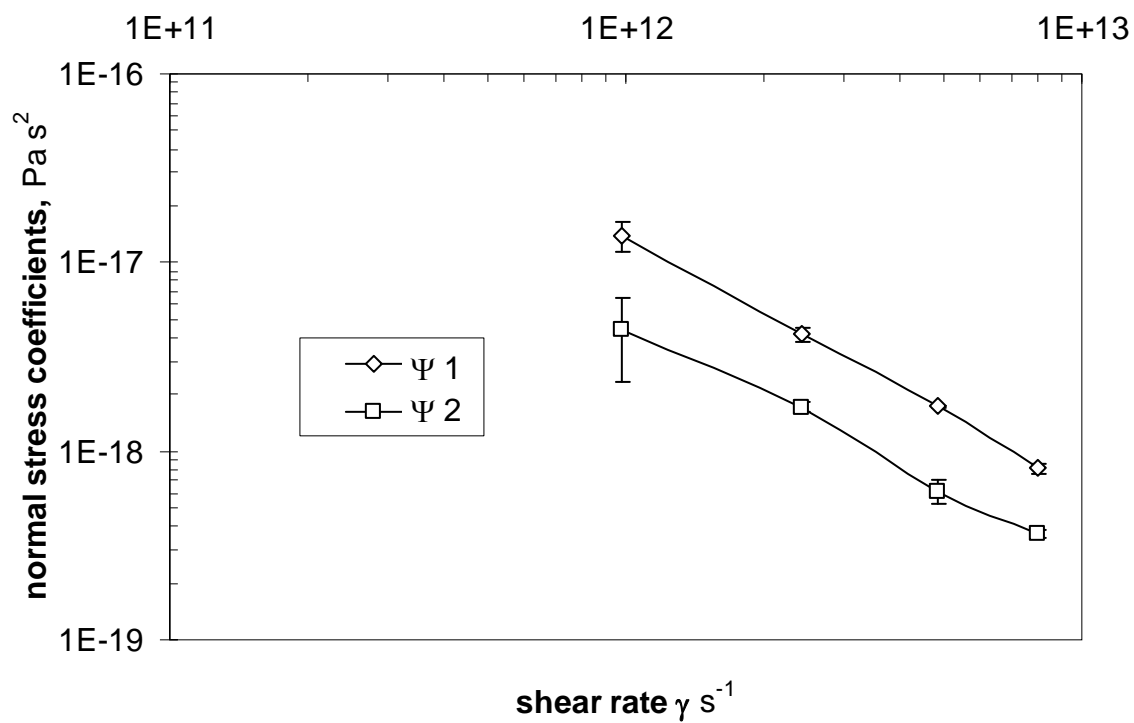
Figure 5.8 First and second normal stress coefficients vs. shear rate for polymer chains of

L=8.

There have been several publications where comparison has been made between molecular dynamics simulations, the Rouse model and the model of Doi and Edwards. Some of these have aimed to observe reptative diffusion; some have calculated the correlation functions for the Rouse modes while others have simply looked for the onset of the reptative regime in both rheological properties and the self-diffusion of molecules in the melt.

5.3   Rheological Properties of PNC

From processing points of view, it is very important to explore the rheological properties of polymer nanocomposites and also relate their rheological properties to the nature and microsctructure of the materials. The flow of low molecular weight polymer melts and solutions have been relatively well understood, but our understanding of the viscoelastic properties of polymer nanocomposites and influence of polymer-particle interactions on the viscoelastic properties of the matrix is quite immature. In spite of a large body of results coming mainly from experiments, the understanding of behavior of polymer composites under shear flow and the possibilities of a theoretical description are still limited, especially on the molecular level. Providing an insight into the flow induced phenomena on the molecular level such as coil deformation and chain orientation is of great importance. Therefore computer simulations can be very helpful.

A huge amount of studies have dealt with the improvement of the thermoelasticity of plastic films and the most studied approach is the modification of the plastic material by including fillers and specifically nanofillers [101]. The inclusion of nanoparticles in polymer matrices leads to undesired variations in other properties and in particular to a

strong increase in melt viscosity, which limits the maximum amount of inorganic nanofiller to less than 10 wt.% [102]. The improvement of the thermal and mechanical properties observed for nanocomposites with respect to unfilled matrices has been generally attributed to two distinct phenomena. Filler particles can influence the viscoelastic properties of the system by a variety of different mechanisms. On one hand, the particle induced effects on the dynamics of polymer segments modify the relaxation spectrum of the polymers. Second, particle aggregation effects lead to slow relaxations and substantial enhancements in elasticity. In this section, we include nanoparticles in polymer matrix and study the shear-induced properties.

5.3.1   Shear Viscosity and Einstein Equation

Figure 5.9 shows the relative viscosity ($\eta_r = \eta/\eta_0$) plotted vs. shear rate for different nanoparticle filling fractions. Over the range of shear rates studied, the shear viscosity is strongly dependent on the shear rate. These trends are quantified by fitting the power-law regions in the data with the following relationship: $\eta = A \cdot \gamma^B$. The values of the parameters A and B are listed in Table 5.4 and show that the magnitudes of the viscosity exponents |B| are greater in the more filler concentrated systems, indicating that increased loadings of the particles leads to an enhanced shear thinning of the composite. For the systems of polymer suspension, the addition of particles leads to an increase in the overall viscosity. This monotonic increase of viscosity with filler concentration is also commonly observed in experimental systems.
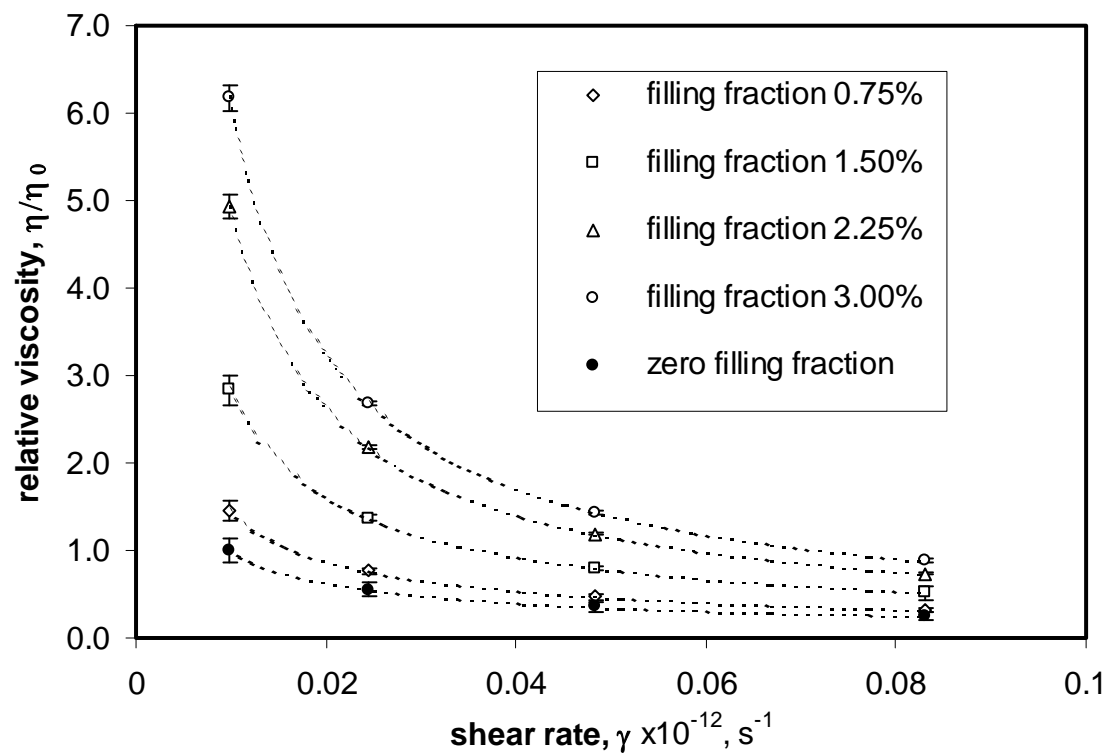
Figure 5.9 Shear rate dependent relative viscosity for different nanoparticle filling fractions, and no fillers. The dotted lines interpolate between the data points as a guide for the eye only.

Table 5.4 Description of shear viscosity curves: Parameters A and B obtained from the power-law fit to the data in Figure 5.9.

Nanoparticle filling fraction	0.75 %	1.5 %	2.25 %	3.0 %
A	0.0129	0.017	0.0188	0.0215
B	-0.71	-0.79	-0.89	-0.91

The results of our simulations are compared with an experimental analysis of a real polymer filled with spherical nanoparticles. The experimental system contains much longer polymers, as well as filler particles, which are as much as 5 times larger than those simulated. Despite these considerable differences of scale, this study aims to illustrate a general qualitative agreement between the forms of the shear viscosity versus strain rate curves observed via experiment and simulation.

Einstein predicted that the viscosity of a dilute suspension of rigid spheres has a linear relation with particle volume fraction ϕ, written as Equation $\frac{\eta}{\eta_0} = 1 + 2.5\phi$ where η and η_0 are the viscosities of the suspension and the suspending medium, respectively. The Einstein relation is justified only for a very dilute suspension system with negligible interparticle interaction and with an identical continuous medium. Given the interparticle interaction, the viscosity of the suspension increases significantly over that predicted by the Einstein equation.

As expected for systems so different, there is significant quantitative deviation of the simulation results from the experimental data, which is most clearly apparent in the zero shear viscosity results. The zero-shear viscosities of each of the systems are calculated by extrapolating the shear viscosity to $\dot{\gamma} = 0$, and scaled by the zero-shear viscosity of the polymer melt η_{p0}, for each system.

Figure 5.10 shows the zero shear viscosities η/η_0 plotted against nanoparticle filling fraction ϕ, for the simulated systems of various polymer chain lengths. As expected for simple fluid suspensions [103], it is observed that, for all the polymer matrices, the shear viscosity consistently increases with filler concentration. The

monotonic increase of viscosity with filler concentration is a commonly observed trend in experimental systems. In addition to Kao and Bhattacharya's PP-CaCO$_3$ studies [104], this behavior has been observed in a range of polymer-clay systems [105-108] and seems to be an important general feature of composites of molten polymers with micron-scale fillers. The trends in the steady-state shear viscosities of the simulated polymer-filler system agree with those seen in the experimental results; shear viscosities, zero-shear viscosities, and the rate of shear thinning are all seen to increase with filler content in both the experimental and simulated systems.
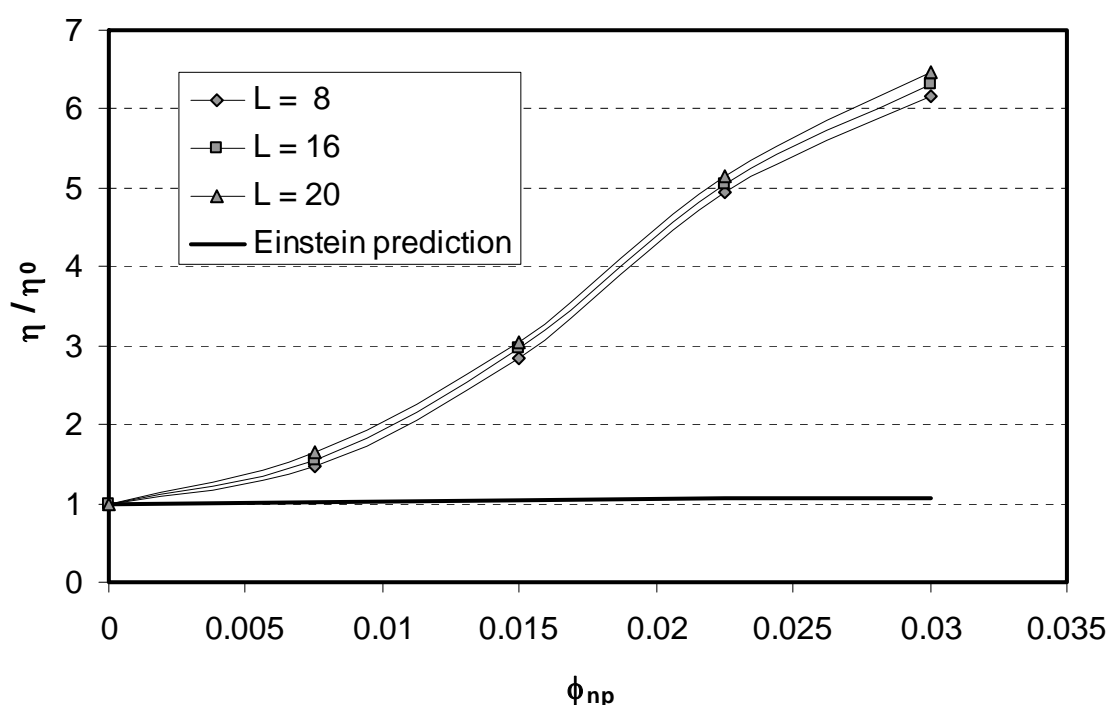
Figure 5.10 Zero-shear viscosity η/η_0 as a function of nanoparticle filling fraction for different polymer chain lengths.

Previous research on polymers filled with spherical microparticles [109] has shown that, rather than following predictions depending exclusively on filling fraction, the viscosity of the composite can be sensitive to the size of the filler particles themselves. Smaller-sized spherical filler particles present to the polymer a larger surface area for each filling fraction than larger particles. High aspect ratio fillers such as clay platelets show increased viscosities at lower concentrations [106-108] due to their higher surface area. Similarly, decreasing the size of spherical filler particles while keeping the filler volume fraction constant is also expected to increase the viscosity of the composite [109], in some cases resulting in a yield stress. It is reasonable to conclude that this occurs mainly due to the increased polymer adsorbtion on the filler particles due to the increased available surface area, and is thus associated with strong thermodynamic non-ideality of the composite system.

5.3.2 Nanoparticle Motion Under Shear

The dynamics and rheology of colloid suspensions have been well-understood in a continuum fluid-mechanical framework dating back to Stokes and Einstein [103]. These theories predict that the diffusivity of particles decreases with an increase in the viscosity of the fluid, and that the addition of particles increases the overall viscosity of the suspension. To address the equilibrium dynamical characteristics of the suspension, we compute the mean-squared displacements (MSD) of the nanoparticle center of mass $\langle r_C^2 \rangle$, corresponding to the simplest of the time dependent correlation functions for our system. We compute $\langle r_C^2 \rangle$ as $\langle r_C^2(t) \rangle = \langle [r_i(t) - r_i(0)]^2 \rangle$, where $\langle ... \rangle$ denotes the averages over different nanoparticles as well as different blocks of time interval t.

Displayed in Figure 5.11 (a) is our simulation results for the time dependent MSD $\langle r_C^2 \rangle$ of nanoparticles center of mass for different volume fractions ϕ in polymer matrix (chains of L = 8). From the slope of these lines, the self-diffusion coefficient $D = \langle r^2 \rangle / 6t$ is obtained (Figure 5.11 b) and is averaged over the number of nanoparticles in the system. Upon increase in the volume fraction, we observe the diffusion decrease. The diffusion constant D as a function of packing fraction of the particles have been widely studied since they provide a useful test of theoretical modeling and more specifically the role of long range, hydrodynamic interactions [110].
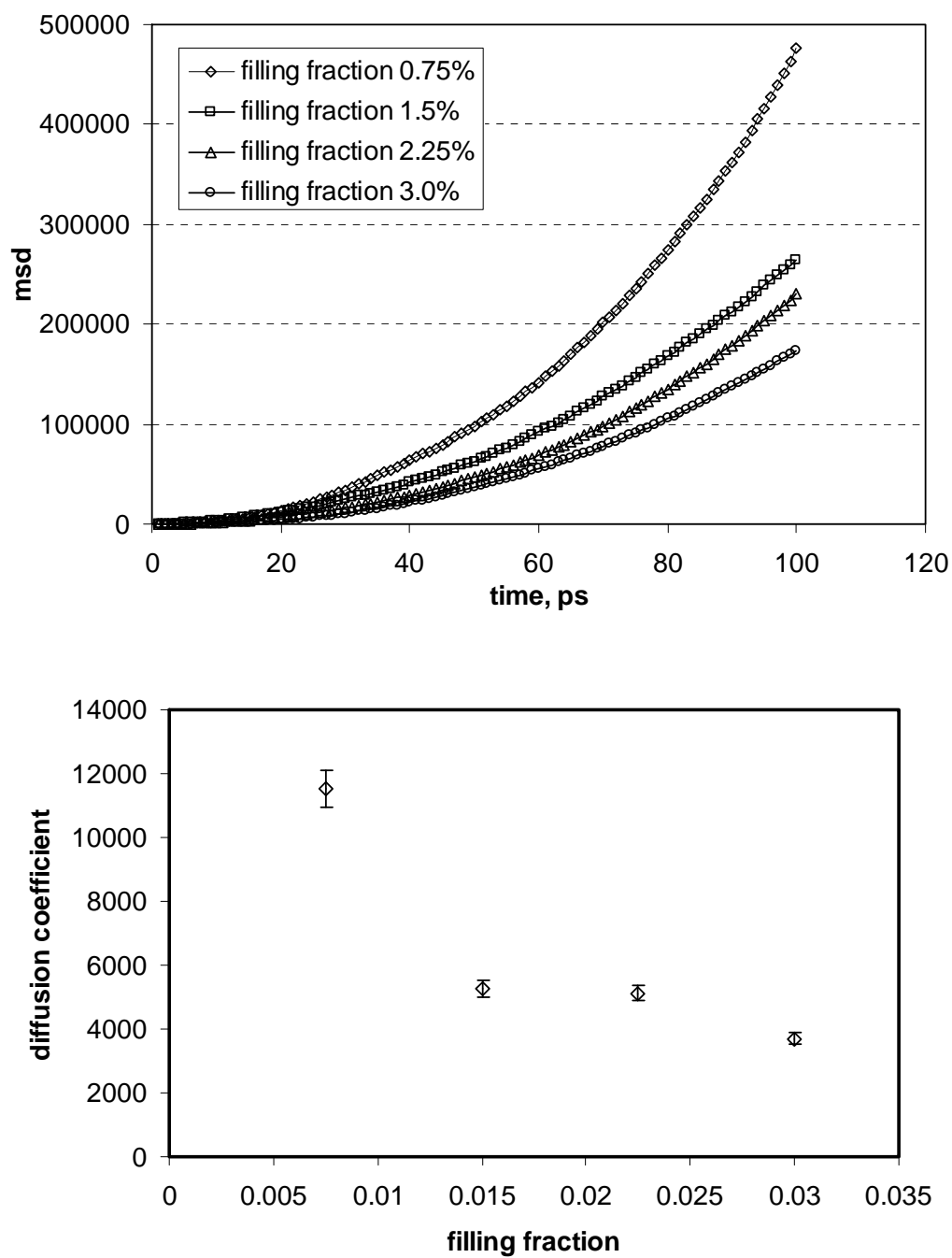
Figure 5.11 Mean square displacement (a) and diffusion coefficient (b) of nanoparticles

in polymer melt.

5.4   Summary

In this chapter, we study the rheological properties of silica nanoparticle in polyethylene melt. A few of the rheological properties are compared with theory and experimental studies for validating our coarse-grained model. The steady-state shear viscosities of a model polymer nanocomposite are studied and can be usefully compared with experimental results for real polymer composites. The difference in scale between the simulated systems and the composites examined experimentally precludes quantitative comparisons of the results, but several qualitative similarities in shear rheology are evident. It is shown that the shear viscosities of nanoparticle-filled systems exceed those of the pure polymer, with increased viscosities resulting from increasing the filler content in the composite. They also both exhibit a trend towards stronger shear-thinning behavior as the proportions of the filler are increased.

Chapter 6

CONCLUSIONS AND RECOMMENDATIONS

In this chapter, we first present a summary of conclusions from the research work detailed in this dissertation, followed by some recommendations for future work for understanding the phase behavior, structural characteristics and rheological properties of polymer-particle systems.

6.1   Summary of Research

This thesis reports molecular dynamics simulations of two different solid-fluid systems: i) silica nanoparticles embedded in a polyethylene melt ii) silica nanoaggregates in supercritical CO_2. Both of them contain silica nanoparticles, but are modeled at different levels, atomistic and coarse-graining. The coarse-graining process includes experimental data, thermodynamic theory, and atomistic simulations, and is described in the first part of this thesis. The application of this approach to the case of polyethylene chains in presence of silica nanoparticles leads to the prediction of the interaction parameters between solid silica particles and polyethylene melt.

Once the coarse-grained model is fully characterized, we studied the dispersion of silica nanoparticles in polyethylene matrix. The RDF and specific heat calculations indicate that for filling fractions smaller than 3 wt% the system is in a dispersed state and for filling fractions of c.a. 3 wt% and larger the nanoparticles show agglomeration. We show that thermodynamically stable dispersion of nanoparticles into a polymer melt is enhanced for systems where the polymer radius of gyration is greater than the radius of

the nanoparticle. Dispersed nanoparticles swell the polymer chains, and this results on the polymer radius of gyration increasing with nanoparticle filling fraction. The polymer-mediated forces are also more repulsive in the case of longer chains than in the case of shorter ones.

This thesis also reports on the rheology of both pure and nanoparticle-filled polymers. The steady-state shear viscosities and diffusion of our model polymer nanocomposite are calculated and compared with theory and experimental studies for validating our coarse-grained model. Our results show good agreement with experimental data. As the shear rate is increased, both systems exhibit a trend towards stronger shear-thinning behavior. In addition, the shear viscosities of nanoparticle-filled systems are greater than those of the pure polymer, which results from the increased filler content in the polymer.

We also perform molecular simulations for a second solid-fluid system: silica nanoparticle agglomerates in supercritical CO_2. The interaction parameters are determined by fitting the experimental adsorption isotherms. The calculated solvation force is mostly negative (attractive) and its dependence on the interparticle distance shows a minimum, which indicates maximum attraction at a pressure above the critical point. In a posterior study, we focus on the rupture of nanoagglomerate that is exposed to shear forces. Larger agglomerates of D~15nm were broken with $F \sim 1.07 \times 10^{-8}$N. Smaller agglomerates with D~7.5nm were broken with $F \sim 1.0 \times 10^{-7}$N. Our calculated value of CO_2 self diffusion coefficient appears to be one order of magnitude smaller than the experimental data.

6.2   Recommendations for Future Work

Based upon the experience and the knowledge gained, further research needs to be done in the following areas:

6.2.1   <u>Longer Polymer Chains and Branched Chains</u>

One of the main limitations of the systems with and without nanoparticles is the polymer chain length. Short chains make it difficult to work with the parameters that are closer to those investigated experimentally. Further work in this field should focus on simulating much longer chains. By extending the polymer/nanoparticle composite research to longer chains, we will be able to study the effect of varying the nanoparticle size relative to the polymer chain dimension e.g. the athermal end-to-end distance. This will allow us to determine the importance of relative sizes on determining the structural properties of the composites.

In this research, our focus was limited to the effect of homopolymers on the interactions, phase behavior and structural features of particulate suspensions. However, a substantial number of the practical situations comprise of nanoparticles in presence of copolymers or blends of different homopolymers. Such mixtures are being actively investigated for their potential to yield complex, highly ordered composites for next generation catalysts, selective membranes, and photonic band gap materials. The specific morphology and hence the applicability of these materials critically depends on the polymer architecture and on parameters such as the size and volume fraction of the particles, size asymmetry between different polymeric components/blocks and their relative affinities for the particle surfaces etc.

In addition, the introduction of branched chains, and the simulation of polydisperse melts will indicate to rheologists what is occurring at the molecular level. Techniques to allow mapping between simulated and real molecules need to be established, allowing the work to be fully utilized by industry.

6.2.2 Modified Surface and Shape of Nanoparticles

The surface of particles has an influence on the properties of the adsorbed mixture: its adhesion to freshly cleaved mica is stronger than to the hydrophobized mica, and the adsorption to the hydrophobized mica surface is in turn stronger than the adsorption to the hydrophobized silica [111, 112]. A possible explanation could be the role of the electrostatic attraction and the thickness of the hydrophobizing layer [113]. Future work should examine the effect of surface hydrophobicity on the dispersion of nanoparticle in polymer matrix.

Another relevant issue is that the spatial distribution of the particle center of mass will depend on, not only the volume fraction, but also the particle size distribution and particle shape (sphere, rod, plate). Hence for extended spheroids (rods and plates), excluded volume interactions between particles will lead to local orientation correlations, as well as possible fractal association leading to percolation behavior and interpenetrating polymer–nanoparticle rich regions [114, 115]. All of these factors will have substantial impact on phase transitions and related morphologies, including polymer crystallization, polymer blend phase separation, and block copolymer mesophase organization. It will be extremely beneficial to compare the nanoparticle shape to phase transition.

6.2.3   Surfactant Structure and Mixtures

Surfactant micellization phenomena are very sensitive to the specific chemical structure. From data assembled in [116], it can be seen that an increase in the length of alkane chains of nonionic surfactant is accompanied by a pronounced decrease in the CMC. In addition, it is known experimentally that the CMC of a surfactant generally increases as the degree of branching in the surfactant tail increases [117]. When developing a coarse-grained model for surfactant molecule with branches, we must consider that such structural details are not removed or obscured.

In addition, mixtures of two or more types of surfactants can be considered within the polymer matrix. This has not been done yet in the literature and deserves more attention. If two nonionic surfactants are mixed, they will form mixed micelles in the bulk, and also on the surface they will form mixed aggregates [118]. The composition of adsorbed layer probably depends on both species. By carefully choosing different surfactant architectures and bulk concentrations, it may be possible to make mixtures that can disperse nanoparticles in a more effective fashion.

References

1.	Sumita, M., et al., *Tensile yield stress of polypropylene composites filled with ultrafine particles.* Journal of Materials Science, 1983. **18**(6): p. 1758-1764.

2.	Hussain, M., et al., *Fracture behavior and fracture toughness of particulate filled epoxy composites.* Materials Letters, 1996. **27**(1-2): p. 21-25.

3.	Barnes, K.A., et al., *Suppression of dewetting in nanoparticle-filled polymer films.* Macromolecules, 2000. **33**(11): p. 4177-4185.

4.	Mackay, M.E., et al., *Influence of dendrimer additives on the dewetting of thin polystyrene films.* Langmuir, 2002. **18**(5): p. 1877-1882.

5.	Alexandre, M. and P. Dubois, *Polymer-layered silicate nanocomposites: preparation, properties and uses of a new class of materials.* Materials Science and Engineering, 2000. **28**: p. 1-63.

6.	Sumita, M., et al., *Dynamic Mechanical-Properties of Polypropylene Composites Filled with Ultrafine Particles.* Journal of Applied Polymer Science, 1984. **29**(5): p. 1523-1530.

7.	Dickey, M.D., et al., *High-aspect ratio polymeric pillar arrays formed via electrohydrodynamic patterning.* Journal of Materials Science, 2008. **43**(1): p. 117-122.

8.	Windlass, H., et al., *Colloidal processing of polymer ceramic nanocomposite integral capacitors.* Ieee Transactions on Electronics Packaging Manufacturing, 2003. **26**(2): p. 100-105.

9.	Riman, R.E., *Private communication.* 2005.

10.	Laitinen, N. and A.M. Juppo, *Measurement of pharmaceutical particles using a time-of-flight particle sizer.* European Journal of Pharmaceutics and Biopharmaceutics, 2003. **55**(1): p. 93-98.

11.	Uhland, S.A., M.J. Cima, and E.M. Sachs, *Additive-enhanced redispersion of ceramic agglomerates.* Journal of the American Ceramic Society, 2003. **86**(9): p. 1487-1492.

12.	Yang, J., et al., *Mixing of nano-particles by rapid expansion of high-pressure suspensions.* Advanced Powder Technology, 2003. **14**(4): p. 471-493.

13.	Stroud, W.J., J.E. Curry, and J.H. Cushman, *Capillary condensation and snap-off in nanoscale contacts.* Langmuir, 2001. **17**(3): p. 688-698.

14.	Jang, J., J. Jeon, and S. Hwang, *Monte Carlo study on the water bridge that produces the pull-off force in atomic force microscopy.* COLLOIDS AND SURFACES A-PHYSICOCHEMICAL AND ENGINEERING ASPECTS 2007. **300**(1-2): p. 60-64.

15.	Mark, J., *Physical Properties of Polymers.* 3rd ed. 2003: Cambridge University Press.

16.	Sperling, L.H., *Introduction to physical polymer science.* 4th ed. 2006: Wiley.

17.	Moore, J.D., et al., *A molecular dynamics study of a short-chain polyethylene melt. I. Steady-state shear.* Journal of Non-Newtonian Fluid Mechanics, 2000. **93**(1): p. 83-99.

18.	Baig, C., et al., *Rheological and structural studies of linear polyethylene melts under planar elongational flow using nonequilibrium molecular dynamics simulations.* Journal of Chemical Physics, 2006. **124**(8).

19.   Baig, C., et al., *Rheological and structural studies of liquid decane, hexadecane, and tetracosane under planar elongational flow using nonequilibrium molecular-dynamics simulations.* Journal of Chemical Physics, 2005. **122**(18).

20.   Daoulas, K.C., et al., *Self-consistent-field study of compressible semiflexible melts adsorbed on a solid substrate and comparison with atomistic simulations.* Macromolecules, 2005. **38**(16): p. 7134-7149.

21.   Depa, P.K. and J.K. Maranas, *Speed up of dynamic observables in coarse-grained molecular-dynamics simulations of unentangled polymers.* Journal of Chemical Physics, 2005. **123**(9).

22.   Depa, P.K. and J.K. Maranas, *Dynamic evolution in coarse-grained molecular dynamics simulations of polyethylene melts.* Journal of Chemical Physics, 2007. **126**(5).

23.   Vettorel, T. and H. Meyer, *Coarse graining of short polythylene chains for studying polymer crystallization.* Journal of Chemical Theory and Computation, 2006. **2**(3): p. 616-629.

24.   Xu, G.Q., H. Lin, and W.L. Mattice, *Configuration selection in the simulations of the crystallization of short polyethylene chains in a free-standing thin film.* Journal of Chemical Physics, 2003. **119**(13): p. 6736-6743.

25.   Guerrault, X., B. Rousseau, and J. Farago, *Dissipative particle dynamics simulations of polymer melts. I. Building potential of mean force for polyethylene and cis-polybutadiene.* Journal of Chemical Physics, 2004. **121**(13): p. 6538-6546.

26.   Allen, M.P. and D.J. Tildesley, *Computer Simulation of Liquids*. 1990, Oxford: Clarendon Press.

27.   Starr, F.W., T.B. Schroder, and S.C. Glotzer, *Molecular dynamics simulation of a polymer melt with a nanoscopic particle.* Macromolecules, 2002. **35**(11): p. 4481-4492.

28.   Thompson, R.B., et al., *Predicting the mesophases of copolymer-nanoparticle composites.* Science, 2001. **292**(5526): p. 2469-2472.

29.   Ginzburg, V.V., *Influence of nanoparticles on miscibility of polymer blends. A simple theory.* Macromolecules, 2005. **38**(6): p. 2362-2367.

30.   Marla, K.T. and J.C. Meredith, *Simulation of interaction forces between nanoparticles in the presence of Lennard-Jones polymers: Freely adsorbing homopolymer modifiers.* Langmuir, 2005. **21**(1): p. 487-497.

31.   Marla, K.T. and J.C. Meredith, *Simulation of interaction forces between nanoparticles: End-grafted polymer modifiers.* Journal of Chemical Theory and Computation, 2006. **2**(6): p. 1624-1631.

32.   Hooper, J.B. and K.S. Schweizer, *Contact aggregation, bridging, and steric stabilization in dense polymer-particle mixtures.* Macromolecules, 2005. **38**(21): p. 8858-8869.

33.   Shen, Y.Y., et al., *Molecular dynamics study of the influence of surfactant structure on surfactant-facilitated spreading of droplets on solid surfaces.* Langmuir, 2005. **21**(26): p. 12160-12170.

34.   Rosen, M.J., *Surfactants and Interfacial Phenomena.* 3rd ed. 2004: Wiley-Interscience.

35. Schick, M.J., *Nonionic surfactants : physical chemistry*. Surfactant science series. Vol. 23. 1983: New York : M. Dekker.

36. Suri, P., et al., *Effect of mixing on the rheology and particle characteristics of tungsten-based powder injection molding feedstock*. Materials Science and Engineering a-Structural Materials Properties Microstructure and Processing, 2003. **356**(1-2): p. 337-344.

37. Osman, M.A., J.E.P. Rupp, and U.W. Suter, *Effect of non-ionic surfactants on the exfoliation and properties of polyethylene-layered silicate nanocomposites*. Polymer, 2005. **46**(19): p. 8202-8209.

38. Israelachvili, J.N., *Intermolecular and Surface Forces*. 1991: Academic Press.

39. Wallqvist, A. and B.J. Berne, *Computer-Simulation of Hydrophobic Hydration Forces on Stacked Plates at Short-Range*. Journal of Physical Chemistry, 1995. **99**(9): p. 2893-2899.

40. Dijkstra, M. *Structure and solvation forces in confined films of alkanes*. 1998.

41. Dijkstra, M., R. van Roij, and R. Evans, *Phase diagram of highly asymmetric binary hard-sphere mixtures*. Physical Review E, 1999. **59**(5): p. 5744-5771.

42. Yethiraj, A. and C.K. Hall, *Monte-Carlo Simulation of Polymers Confined between Flat Plates*. Macromolecules, 1990. **23**(6): p. 1865-1872.

43. Shinto, H., M. Miyahara, and K. Higashitani, *Evaluation of interaction forces between macroparticles in simple fluids by molecular dynamics simulation*. Journal of Colloid and Interface Science, 1999. **209**(1): p. 79-85.

44. Shinto, H., et al., *Interaction forces between nanoparticles in diol-water mixtures: A molecular dynamics study with coarse-grained model*. Langmuir, 2002. **18**(10): p. 4171-4178.

45. Qin, Y. and K.A. Fichthorn, *Molecular-dynamics simulation of forces between nanoparticles in a Lennard-Jones liquid*. Journal of Chemical Physics, 2003. **119**(18): p. 9745-9754.

46. Qin, Y. and K.A. Fichthorn, *Solvation forces between colloidal nanoparticles: Directed alignment*. Physical Review E, 2006. **73**(2).

47. Snook, I.K. and W. van Megen, *Solvation forces in simple dense fluid. I.* Journal of Chemical Physics, 1980. **72**(5): p. 2907-2913.

48. Gao, J.P., W.D. Luedtke, and U. Landman, *Layering transitions and dynamics of confined liquid films*. Physical Review Letters, 1997. **79**(4): p. 705-708.

49. Wang, Y.T., K. Hill, and J.G. Harris, *Confined Thin-Films of a Linear and Branched Octane - a Comparison of the Structure and Solvation Forces Using Molecular-Dynamics Simulations*. Journal of Chemical Physics, 1994. **100**(4): p. 3276-3285.

50. Li, L.W., D. Bedrov, and G.D. Smith, *Water-induced interactions between carbon nanoparticles*. Journal of Physical Chemistry B, 2006. **110**(21): p. 10509-10513.

51. Schoen, M. *Capillary condensation between mesocopically rough surfaces*. 2002.

52. Jang, J.Y., M.A. Ratner, and G.C. Schatz, *Atomic-scale roughness effect on capillary force in atomic force microscopy*. Journal of Physical Chemistry B, 2006. **110**(2): p. 659-662.

53. Altunin, V.V., *IUPAC. International Thermodynamic Tables of the Fluid State*. Carbon Dioxide. Vol. 3. 1976, London: Pergamon Press.

54. Ravikovitch, P.I., et al., *Unified approach to pore size characterization of microporous carbonaceous materials from N2, Ar, and CO2 adsorption isotherms.* Langmuir, 2000. **16**(5): p. 2311-2320.

55. Wojcik, M., K.E. Gubbins, and J.G. Powles, *The thermodynamics of symmetric two centre Lennard-Jones liquids.* Molecular Physics, 1982. **45**(6): p. 1209 - 1225.

56. Harris, J.G. and K.H. Yung, *Carbon Dioxides Liquid-Vapor Coexistence Curve and Critical Properties as Predicted by a Simple Molecular-Model.* Journal of Physical Chemistry, 1995. **99**(31): p. 12021-12024.

57. Moller, D. and J. Fischer, *Determination of an Effective Intermolecular Potential for Carbon-Dioxide Using Vapor Liquid-Phase Equilibria from Npt Plus Test Particle Simulations.* Fluid Phase Equilibria, 1994. **100**: p. 35-61.

58. Vrabec, J., J. Stoll, and H. Hasse, *A set of molecular models for symmetric quadrupolar fluids.* Journal of Physical Chemistry B, 2001. **105**(48): p. 12126-12133.

59. Stoll, J., et al., *Comprehensive study of the vapour-liquid equilibria of the pure two-centre Lennard-Jones plus pointquadrupole fluid.* Fluid Phase Equilibria, 2001. **179**(1-2): p. 339-362.

60. Neimark, A.V. and A. Vishnyakov, *A simulation method for the calculation of chemical potentials in small, inhomogeneous, and dense systems.* Journal of Chemical Physics, 2005. **122**(23): p. 234108.

61. Vishnyakov, A. and A.V. Neimark, *Studies of liquid-vapor equilibria, criticality, and spinodal transitions in nanopores by the gauge cell Monte Carlo simulation method.* Journal of Physical Chemistry B, 2001. **105**(29): p. 7009-7020.

62. Span, R. and W. Wagner, *A new equation of state for carbon dioxide covering the fluid region from the triple-point temperature to 1100 K at pressures up to 800 MPa.* Journal of Physical and Chemical Reference Data, 1996. **25**(6): p. 1509-1596.

63. Rigby, M., et al., *The Forces Between Molecules*. 1986: Oxford University Press.

64. Vishnyakov, A., P.I. Ravikovitch, and A.V. Neimark, *Molecular level models for CO2 sorption in nanopores.* Langmuir, 1999. **15**(25): p. 8736-8742.

65. Johnson, J.K., J.A. Zollweg, and K.E. Gubbins, *The Lennard-Jones Equation of State Revisited.* Molecular Physics, 1993. **78**(3): p. 591-618.

66. Zhuravlev, L.T., *The surface chemistry of amorphous silica. Zhuravlev model.* Colloids and Surfaces a-Physicochemical and Engineering Aspects, 2000. **173**(1-3): p. 1-38.

67. Morishige, K., et al., *Capillary critical point of argon, nitrogen, oxygen, ethylene, and carbon dioxide in MCM-41.* Langmuir, 1997. **13**(13): p. 3494-3498.

68. Sonwane, C.G., S.K. Bhatia, and N. Calos, *Experimental and theoretical investigations of adsorption hysteresis and criticality in MCM-41: Studies with O2, Ar, and CO2.* Industrial & Engineering Chemistry Research, 1998. **37**(6): p. 2271-2283.

69. Bakaev, V.A., et al., *Adsorption of CO2 and Ar on glass surfaces. Computer simulation and experimental study.* Journal of Chemical Physics, 1999. **111**(21): p. 9813-9821.

70. Katoh, M., et al., *Adsorption of CO2 on FSM-type mesoporous silicas.* Physical Chemistry Chemical Physics, 2000. **2**(19): p. 4471-4475.

71. He, Y.F. and N.A. Seaton, *Experimental and computer simulation studies of the adsorption of ethane, carbon dioxide, and their binary mixtures in MCM-41.* Langmuir, 2003. **19**(24): p. 10132-10138.

72. He, Y.F. and N.A. Seaton, *Heats of adsorption and adsorption heterogeneity for methane, ethane, and carbon dioxide in MCM-41.* Langmuir, 2006. **22**(3): p. 1150-1155.

73. Zhuravlev, L.T. *Characterization of Amorphous Silica Surface.* 1993.

74. Ishikawa, T., et al., *Surface silanol groups of mesoporous silica FSM-16.* Journal of the Chemical Society-Faraday Transactions, 1996. **92**(11): p. 1985-1989.

75. Bakaev, V.A. and W.A. Steele, *On the computer simulation of a hydrophobic vitreous silica surface.* Journal of Chemical Physics, 1999. **111**(21): p. 9803-9812.

76. Bottani, E.J., V. Bakaev, and W. Steele, *A Simulation/Experimental Study of the Thermodynamic Properties of Carbon-Dioxide on Graphite.* Chemical Engineering Science, 1994. **49**(17): p. 2931-2939.

77. Bakaeva, T.I., V.A. Bakaev, and C.G. Pantano, *Adsorption of CO2 on glass fibers.* Langmuir, 2000. **16**(13): p. 5712-5718.

78. Beebe, R.A., et al., Russ. J. Phys. Chem. (Transl. of Zh. Fiz. Khim.), 1964. **38**: p. 372.

79. Norman, G.E. and V.S. Filinov, *Investigations of phase transitions by a Monte Carlo method.* High Temperature (USSR), 1969. **7**: p. 216-222.

80. Ravikovitch, P.I. and A.V. Neimark, *Experimental confirmation of different mechanisms of evaporation from ink-bottle type pores: equilibrium, pore blocking, and cavitation.* Langmuir, 2002. **18**(25): p. 9830-9837.

81. Vishnyakov, A. and A.V. Neimark, *Monte Carlo simulation test of pore blocking effects.* Langmuir, 2003. **19**(8): p. 3240-3247.

82. Lyubartsev, A.P. and A. Laaksonen, *M.DynaMix - a scalable portable parallel MD simulation package for arbitrary molecular mixtures.* Computer Physics Communications, 2000. **128**(3): p. 565-589.

83. Neimark, A.V. and A. Vishnyakov, *A simulation method for the calculation of chemical potentials in small, inhomogeneous, and dense systems.* Journal of Chemical Physics, 2005. **122**(23).

84. Chennamsetty, N., H. Bock, and K.E. Gubbins, *Coarse-grained potentials from Widom's particle insertion method.* Molecular Physics, 2005. **103**(21-23): p. 3185-3193.

85. Nam, C.H., et al., *Aerated vibrofluidization of silica nanoparticles.* AIChE Journal, 2004. **50**(8): p. 1776-1785.

86. O'hern, H.A.J. and J.J. Martin, *Diffusion in carbon dioxide at elevated pressures.* Industrial and Engineering Chemistry, 1955. **47**: p. 2081-2086.

87. Advani, S.G. and C.L. Tucker, *The Use of Tensors to Describe and Predict Fiber Orientation in Short Fiber Composites.* Journal of Rheology, 1987. **31**(8): p. 751-784.

88. Tiu, C., T. Moussa, and P.J. Carreau, *Steady and dynamic shear properties of non-aqueous drag-reducing polymer solutions.* Rheologica Acta, 1995. **34**(6): p. 586-600.

89. Vlassopoulos, D. and W.R. Schowalter, *Steady Viscometric Properties and Characterization of Dilute Drag-Reducing Polymer-Solutions.* Journal of Rheology, 1994. **38**(5): p. 1427-1446.

90. Micic, P. and S.N. Bhattacharya, *Elongational behavior of polyethylene melts - Effect of deformation.* Polymer Engineering and Science, 2000. **40**(7): p. 1571-1580.

91. Paul, W., G.D. Smith, and D.Y. Yoon, *Static and dynamic properties of a n-C100H202 melt from molecular dynamics simulations.* Macromolecules, 1997. **30**(25): p. 7772-7780.

92. Paul, W., et al., *Chain motion in an unentangled polyethylene melt: A critical test of the rouse model by molecular dynamics simulations and neutron spin echo spectroscopy.* Physical Review Letters, 1998. **80**(11): p. 2346-2349.

93. Harmandaris, V.A., V.G. Mavrantzas, and D.N. Theodorou, *Atomistic molecular dynamics simulation of stress relaxation upon cessation of steady-state uniaxial elongational flow.* Macromolecules, 2000. **33**(21): p. 8062-8076.

94. Harmandaris, V.A., et al., *Crossover from the rouse to the entangled polymer melt regime: Signals from long, detailed atomistic molecular dynamics simulations, supported by rheological experiments.* Macromolecules, 2003. **36**(4): p. 1376-1387.

95. Kremer, K. and G.S. Grest, *Dynamics of Entangled Linear Polymer Melts - a Molecular-Dynamics Simulation.* Journal of Chemical Physics, 1990. **92**(8): p. 5057-5086.

96. Mondello, M., et al., *Dynamics of n-alkanes: Comparison to Rouse model.* Journal of Chemical Physics, 1998. **109**(2): p. 798-805.

97. Paul, W., D.Y. Yoon, and G.D. Smith, *An Optimized United Atom Model for Simulations of Polymethylene Melts.* Journal of Chemical Physics, 1995. **103**(4): p. 1702-1709.

98. Mondello, M. and G.S. Grest, *Molecular-Dynamics of Linear and Branched Alkanes.* Journal of Chemical Physics, 1995. **103**(16): p. 7156-7165.

99. Bird, R.B., *Dynamics of polymeric liquids.* 2nd ed. Fluid mechanics. Vol. 1. 1987: Wiley.

100. Weissenberg, K., *A continuum theory of rheological phenomena.* Nature, 1947. **159**: p. 310-311.

101. Sorrentino, A., M. Tortora, and V. Vittoria, *Diffusion behavior in polymer-clay nanocomposites.* Journal of Polymer Science Part B-Polymer Physics, 2006. **44**(2): p. 265-274.

102. Arunvisut, S., S. Phummanee, and A. Somwangthanaroj, *Effect of clay on mechanical and gas barrier properties of blown film LDPE/Clay nanocomposites.* Journal of Applied Polymer Science, 2007. **106**(4): p. 2210-2217.

103. Batchelor, G.K., *An introduction to fluid dynamics.* First Cambridge Mathematical Library ed. 2000: Cambridge University Press.

104. Kao, N., A. Chandra, and S. Bhattacharya, *Melt strength of calcium carbonate filled polypropylene melts.* Polymer International, 2002. **51**(12): p. 1385-1389.

105. Krishnamoorti, R., R.A. Vaia, and E.P. Giannelis, *Structure and dynamics of polymer-layered silicate nanocomposites.* Chemistry of Materials, 1996. **8**(8): p. 1728-1734.

106. Choi, H.J., et al., *Preparation and rheological characteristics of solvent-cast poly(ethylene oxide)/montmorillonite nanocomposites.* Macromolecular Rapid Communications, 2001. **22**(5): p. 320-325.

107. Prasad, R., et al. *Morphology of EVA based nanocomposites under shear and extensional flow*. 2004: John Wiley & Sons Inc.

108. Solomon, M.J., et al., *Rheology of polypropylene/clay hybrid materials.* Macromolecules, 2001. **34**(6): p. 1864-1872.

109. Shenoy, A.V., *Rheology of Filled Polymer Systems*. 1st ed. 1999: Springer - Verlag.

110. Heyes, D.M. and H. Sigurgeirsson, *The Newtonian viscosity of concentrated stabilized dispersions: Comparisons with the hard sphere fluid.* Journal of Rheology, 2004. **48**(1): p. 223-248.

111. Long, J., Z.H. Xu, and J.H. Masliyah, *Adhesion off single polyelectrolyte molecules on silica, mica, and bitumen surfaces.* Langmuir, 2006. **22**(4): p. 1652-1659.

112. Zimin, D., V.S.J. Craig, and W. Kunz, *Adsorption and desorption of polymer/surfactant mixtures at solid-liquid interfaces: Substitution experiments.* Langmuir, 2004. **20**(19): p. 8114-8123.

113. Benes, M., et al., *Surface-dependent transitions during self-assembly of phospholipid membranes on mica, silica, and glass.* Langmuir, 2004. **20**(23): p. 10129-10137.

114. Balazs, A.C., T. Emrick, and T.P. Russell, *Nanoparticle polymer composites: Where two small worlds meet.* Science, 2006. **314**(5802): p. 1107-1110.

115. Balazs, A.C., et al., *Multi-scale model for binary mixtures containing nanoscopic particles.* Journal of Physical Chemistry B, 2000. **104**(15): p. 3411-3422.

116. Huibers, P.D.T., et al., *Prediction of critical micelle concentration using a quantitative structure-property relationship approach .1. Nonionic surfactants.* Langmuir, 1996. **12**(6): p. 1462-1470.

117. Sterpone, F., G. Briganti, and C. Pierleoni, *Sphere versus Cylinder: The Effect of Packing on the Structure of Nonionic C12E6 Micelles.* Langmuir, 2009. **25**(16): p. 8960-8967.

118. Brinck, J. and F. Tiberg, *Adsorption behavior of two binary nonionic surfactant systems at the silica-water interface.* Langmuir, 1996. **12**(21): p. 5042-5047.

CURRICULUM VITA

Yangyang Shen

EDUCATION

- June 2000   Beijing University of Chemical Technology
  B. S. in Polymer Science and Engineering

- May 2007   Rutgers, the State University of New Jersey
  M. S. in Chemical and Biochemical Engineering

- January 2010   Rutgers, the State University of New Jersey
  Ph.D. in Chemical and Biochemical Engineering

PUBLICATIONS

- **Y. Shen**, A. Couzis, J. Koplik, C. Maldarelli, and M. S. Tomassone, et al. A molecular dynamics study of the influence of surfactant structure on surfactant-facilitated spreading of droplets on solid surfaces, Langmuir 2005, 21 12160.

- Vishnyakov, **Y. Shen**, and M. S. Tomassone, Solvation forces between silica bodies in supercritical carbon dioxide, Langmuir 2008, 24, 13420.

- Vishnyakov, **Y. Shen**, and M. S. Tomassone, Interactions of silica nanoparticles in supercritical carbon dioxide, J. Chem. Phys. 2008, 129, 174704.

- **Y. Shen**, A. Vishnyakov, and M. S. Tomassone, Coarse-grained model and molecular dynamics studies on the dispersion of silica nanoparticles in a polyethylene melt, Proceeding of AIChE Annual Meeting, November 2008.